Durham E-Theses

Magnetic field control of ultracold atom-molecule collision

BEYENE, MUSIE

How to cite:

Use policy

Magnetic field control of ultracold atom-molecule collision

Musie Beyene

A Thesis presented for the degree of

Doctor of Philosophy

University of Durham
Department of Chemistry
England

June 2011

Magnetic field control of ultracold atom-molecule collision

Musie Beyene

Abstract

In this work we investigate the potential of controlling *cold* $(O(K)-mK)$ and *ultra-cold* (mK-μK) atom-molecule collisions by tuning scattering states across *Feshbach* resonances using magnetic fields. We are interested in particular in the prospect of suppressing the often undesirable inelastic collisions. The He-O_2 system provides the vehicle for our study. We calculate *bound* and *quasi-bound* states of several isotopic combinations, including their Zeeman structure, to reveal the underlaying pattern for easier characterization of *quasi-bound* states in terms of rigorous and approximately good quantum numbers. These calculations also help us locate the fields at which zero-energy resonances will occur. Scattering calculations are then performed for collisions of ^{3}He and ^{4}He with $^{16}O_2$ at fixed (1 μK) energy but varying magnetic field. The field is varied to sweep the scattering state across resonance. At *low* and *ultralow* energies we enter the Wigner threshold regime where the S-partial wave dominates the wavefunction. The cross sections, and the real and imaginary parts of the scattering length, vary dramatically across resonance. Their profiles are used to analyze the resonances. In a highlight of our results we show that dramatic suppression of inelastic cross sections occur for ^{4}He-$^{16}O_2$. The resonances are relatively wide (of order 100 Gauss), with suppression of inelastic scattering over a similarly wide range of fields and for temperatures ranging from 10 mK down to 1 μK. We conclude that under certain conditions it is possible to almost completely eliminate inelastic collisions. This is potentially very important for cooling techniques, such as evaporative and sympathetic cooling, that require efficient elastic cross sections. Suppression of inelastic collisions can not only increase thermalization efficiency but it can also result in longer trap-lifetimes by reducing transitions to untrapable states.

Acknowledgements

Contents

List of Figures

List of Tables

Chapter 1

Introduction

Research in cold and ultra-cold molecular physics and chemistry has seen phenomenal growth over the last decade and a half fueled by interest from atomic molecular and optical physics, chemical and even condensed matter physics. Initial inspiration was provided by developments in atomic physics. These developments have been land-marked by no less than two Nobel prizes, one for the demonstration of laser cooling [1] and another for the achievement and early fundamental studies of the properties of the collective quantum state of Bose-Einstein condensate (BEC from hereon) in dilute Rubidium [2] and Sodium [3] gases. Our fascination with quantum behavior reserves a special place for its macroscopic manifestation. The award of nobel prizes for the discovery of superfluidity, superconductivity and the laser underscores the place held by collective quantum behavior in modern physics.

Bose Einstein condensates have the important property that the interaction between the constituent particles, which determines important properties of the condensate such as the chemical potential and stability of the condensate [4, 5], can be tuned. Donley and colleagues [6] exploded a stable BEC by suddenly changing the interaction from repulsive to attractive, demonstrating in spectacular fashion the dependence of the condensate stability on the interaction. The ability to tune interactions using a magnetic [7,8] or optical [9–12] field, coupled with trapping in optical lattices [13], opened the possibility of studying quantum phase transitions [14, 15] and understanding the underlaying mechanisms believed to be responsible for su-

perconductivity and superfluidity. Low temperature atoms have also been used in high precision clocks [16–18], matter-wave solitons [19] and interferometry [20, 21], and in tests of violation of fundamental symmetry [22, 23] with consequences far beyond atomic physics.

Encouraged by the achievement of low temperature atoms, efforts are underway to achieve similar temperatures in molecules. Ultra-cold molecular ensembles will be more than a simple extension of ultra-cold atomic systems. Molecules have more degree of freedom which results in a much richer structure. This facilitates the significant enhancement of accuracies of measurements of comparable experiments using atoms and also introduces many new interesting experiments. For example, measurements of the electric dipole moment (EDM) of the electron is enhanced by the presence of closely spaced states that couple the different degrees of freedom [24], while parity violating experiments [25] performed on enantiomers can only be performed on molecules. The increased structure also results in a richer resonance structure. Resonances are important to atomic and molecular collisions and are central to the prospects of controlling collision outcome. Perhaps the most exciting prospects for ultra-cold molecules are due to the possibility of having an electric dipole moment. The dipole moment has allowed the development of a formidable toolkit for the manipulation of molecules which includes decelerators [26, 27], traps [28, 29], a storage ring [30], and even a synchrotron [31]. Some of these developments were inspired by accelerator physics.

In the low temperature limit, which we divide into cold (a few kelvin to 1 mK) and ultra-cold (below 1 mK) following Suominen [32], the long-range interaction plays a dominant role. The dipole-dipole interaction has an R^{-3} dependence on the separation R as compared to the R^{-6} of dispersion forces. Therefore, ultra-cold polar molecules interact more strongly compared to neutral atoms. The long-range nature coupled with the prospects of controlling the interaction of polar molecules in optical lattices [33, 34] raises the prospects of experimental accessability of interesting

many-body states [35–37]. The strongly anisotropic nature of the dipole-dipole interaction has encouraged investigations of steric effects on collision dynamics [38, 39]. Dipole moments also dramatically change the behavior of degenerate systems [40]. Low energy collision behavior of polar molecules is dependent on the dimensions [41]. Restricted to move in two dimensions, polar molecules can form a crystalline structure [34] which might potentially be used to suppress collisions [42]. In general, trapping geometry can be used to tune interactions [40, 43, 44].

There are a few direct consequences of the low energy of ultra-cold atoms and molecules that are responsible for the wide interest in them. The first and principle reason is the quantum nature of particles which begins at about the 1 mK mark. At ultra-cold temperatures the de Broglie wavelength of a particle becomes much longer than typical bond-lengths and at degeneracy exceeds the average separation between the particles in the gas. A few partial waves dominate particle encounters and the position of the nodes and resonances of the waves cannot be washed out, bringing the wave nature of the particles and thus quantum effects to the fore. The second reason is a practical one. For fields achievable in the laboratory the Zeeman and Stark effects typically result in internal energy change of the order of 1 K. This means that meaningful manipulation and control of molecules by external fields is possible only in the cold and ultra-cold regimes. Another important consideration is the inherent precision of measurements implied by these temperatures. Low temperature results in high accuracy and this coupled with excellent electromagnetic technology has resulted in significant efforts in precision measurements of a host of fundamental and not so fundamental quantities as we shall see below. Carr *et al.* [45] have reviewed the science, technology and applications of cold molecules in 2009.

1.1 Applications

1.1.1 Precision spectroscopy

Cold and ultra-cold molecules are ideal for precision measurements for several related reasons. A temperature of, say, 50 μK corresponds to an energy spread of approximately 1 MHz (3×10^{-5} cm^{-1}). This narrow distribution increases the accuracy and efficiency of spectroscopy. Lower speeds and trapping made possible by low temperatures reduce Doppler broadening resulting in higher resolution. Efficiency of optical transitions is increased by the reduced spread of energy giving better signal to noise ratio. Trapping also allows for longer interrogation time increasing the precision of measurements [46]. Collision times at cold and ultra-cold temperatures are orders of magnitude higher than at ambient temperatures, increasing the impact of the interactions which allows for investigation of finer details of the potential energy surface [47].

The potential of photoassociation of cold atoms as a high resolution probe of atomic and molecular structure was pointed out by Thorsheim and colleagues [48]. Ultra-cold atoms interact at long range where the densities of bound states are quite high and their spacing quite small. Photoassociation spectroscopy of ultra-cold atoms has allowed resolution of near dissociation bound states of several alkali-metal dimers [49–51]. The technique also yields important information of the long-range interaction of the atomic species. Photoassociation spectroscopic data is complementary to data of traditional spectroscopy. Stwalley and Wang [52], and more recently Jones *et al.* [53], have reviewed photoassociation of cold and ultra-cold atoms.

Cold and slowed molecules have also improved accuracy in the spectroscopy of more traditional molecules. For example, van Veldhoven *et al.* [46] fully resolved the hyperfine structure of $^{15}ND_3$, while van de Meerakker *et al.* [54] were able to measured the lifetime of the $v = 1$ vibrational level of OH radicals at 59.0 ± 2.0 milliseconds by trapping them. The measurement was in good agreement with the-

oretical calculations [55] which gave a lifetime of 58.3 milliseconds. Velocity tuning technology [26,56] has enabled scattering experiments that are highly sensitive to the details of the potential energy surface [47]. As we shall see below improved accuracy of traditional spectroscopy has benefits beyond atomic and molecular physics.

Time variation of fundamental constants

A fascinating class of precision measurements on cold molecules that have far reaching implications involves experiments to determine the time variation of fundamental constants of physics. Of these, the fine structure constant α [57], and the ratio $\mu = m_{\mathrm{e}}/m_{\mathrm{p}}$ [57–60] of electron to proton mass are accessible to spectroscopic measurements. The determination of μ involves measurements of hyperfine structure which depends on nuclear and electronic masses via their respective spins. Measurements of transitions that have different dependencies on a constant are compared over extended time. Molecules, with their increased degrees of freedom, offer more possibilities of finding closely spaced levels with very different lifetimes, increasing the sensitivity of measurements [57–59]. The best results thus far are from astronomical data. This is principally due to the possibility of measurements that correspond to events separated by astronomical time. In contrast, laboratory experiments can only compare measurements that are separated by months or years. Current limits on the variation of fundamental constants imposed by measurements on cold molecules are on the verge of limits obtained from astronomical data. Lower temperatures are likely to swing the pendulum in favor of laboratory experiments resulting in more stringent tests of the time variation of the constants. Recent experiments include measurements to probe time variation of α using Stark decelerated OH by Hudson and colleagues [61]. Kotochigova *et al.* [60] have proposed the use of Sr_2 molecules to probe the time variation of μ, while DeMille *et al.* [59] proposed the use of Cs_2 for the same purpose. Zelevinsky *et al.* [58] have discussed the use of ultra-cold molecules trapped in an optical lattice. The theoretical and observational status of the variation of the fundamental constants in 2003 has been reviewed by Uzan [62].

Violation of fundamental symmetries

The standard model requires physical laws to be invariant with respect to charge conjugation, space inversion and time reversal. The acronym for the combined symmetry is CPT (Charge, Parity and Time). However, it has been known for some time that the standard model is incomplete. For example, the weak nuclear force does not conserve parity [63] while the strong force is known to violate CP [64, 65]. The asymmetry between matter and antimatter in the universe might also be explained by CP violating interactions. In efforts to extend our understanding, scientists are probing phenomena that violate the predictions of the standard model. These efforts include experiments in search of the EDM of electrons, protons and neutrons which would be a consequence of violation of PT symmetry.

The EDMs, if present, are very small and will require very high electric fields for the resulting shift in energy to be measurable. Such high fields are found inside atoms and molecules but an external field is required to orient the dipole moments. Relativistic effects and higher polarizability improve measurement accuracy making heavy, ultra-cold, polar molecules ideal. Hudson *et al.* [24] have used cold YbF to obtain an upper limit of $-0.2 \pm 3.2 \times 10^{-26}$ e cm, where e is the electronic charge, for the electronic EDM. This is not as good as the best limits obtained by experiments using atoms but is expected to improve with higher molecular densities. Kozlov and DeMille [66] performed calculations which indicated enhanced sensitivity of measurements of the electronic EDM in PbO. Bickman *et al.* [67] and Vutha *et al.* [68] have described experiments using PbO and ThO, respectively.

Enantiomers or chiral molecules are a pair of molecules that are mirror images of each other but cannot be superimposed by simple rotations and translations alone. Enantiomers are very important in biological chemistry [69]. Differences in the properties of chiral molecules would be a consequence of parity violation and thus a result of the weak interaction. Theoretical calculations predict differences of the order of 1 Hz, while recent experiments have achieved accuracies of tens of Hz. The orders

of magnitude improvement in accuracy resulting from the low temperatures now achievable is likely to benefit our understanding of the mechanisms of parity violation. Quack and Stohner have reviewed computational and experimental progress on violation of parity in chiral molecules until 2005 [70].

1.1.2 Quantum chemistry

Wigner's threshold laws [71] state that reactive rate constants have a finite value in the zero-energy limit and early studies [72, 73] showed that this can indeed be significant, prompting further research in ultra-cold collisions and chemistry. In this limit the de Broglie wavelength of the molecules is much longer than typical bond-lengths. This means that the conventional picture of the reacting nuclei rolling along the surface of the electronic potential like classical billiard balls is no longer valid. Instead we must have a quantum mechanical picture of waves over the surface. This opens a whole new set of phenomena associated with waves. Mechanisms such as tunneling become important [72–75]. Long-range van der Waals forces, which are usually unimportant at higher energies, become very important [72, 76, 77] and greatly influence chemical [78] reactions at ultra-cold temperatures. Rotational and vibrational resonances of the van der Waals interaction become crucial [75, 77, 79, 80].

Theoretical studies of ultra-cold chemical reactions has mainly involved atom-dimer systems of distinguishable atoms or indistinguishable spin-polarized alkali-metal atoms. Reactions of indistinguishable systems are usually barrierless and the reactants and products are chemically identical. In an interesting paper, Cvitaš *et al.* [81] considered atom-diatom collisions of isotopically distinguishable Li at ultra-cold temperatures. They found that for collisions of ^{7}Li with ^{6}Li$_2$ and ^{7}Li^{6}Li the reactions are exothermic. For ^{7}Li–^{6}Li^{7}Li, reactive rates were found to be slightly higher than elastic rates. In contrast, only elastic outcomes are possible for ^{6}Li–^{7}Li$_2$/^{6}Li^{7}Li collisions. This has important implications for efforts to produce lithium dimers from mixed atomic isotopes and for sympathetic cooling and trap loss of Li atoms and dimers.

Of greater chemical interest are systems with products that are distinguishable from the reactants. Such reactions often have a barrier and in the ultra-cold regime proceed mainly through tunneling. Systems that have been studied include $F+H_2/HD/D_2$ [72, 73, 82–84], Li-HF [75], F+HCl/DCl [85] and $O+H_2$ [78, 86, 87]. In a study of $F+H_2$ Balakrishnan and Dalgarno [72] found that the product channel is dominated by the $HF(v = 2)$ state. An important investigation in understanding the impact of tunneling is to determine the effect of mass by comparing isotopically different systems. Balakrishnan *at al* [82] found a branching ratio of HF to FD of approximately 5.5 in reactions of $F+HD(v = 0, j = 0)$. Bodo *et al.* [73] investigated reactions of $F+D_2$ and found a difference of three orders of magnitude in reaction rates compared to $F+H_2$ which could not be accounted for by differences in tunneling alone. They artificially varied the mass of the H atom and were able to show that the difference was due to resonance enhancement. They also attributed a higher Wigner limit of reaction rate to resonance enhancement. Similar resonance enhancement was observed earlier by Takayanagi and Kurosaki [79] in $F+H_2/D_2/HD$ systems. Weck and Balakrishnan [88] performed calculations on H+HCl/DCl for dimer states $(v = 0 - 2, j = 0)$ and found resonances corresponding to the $v = 1$ in the entrance channels of both systems to increase reactivity significantly. The $v = 2$ state had a zero-temperature limiting rate coefficient about 8 orders of magnitude higher than the ground state. More recently Quéméner and Balakrishnan [85] studied the reaction rates of F+HCl/DCl. They found reactions of F+HCl to be much faster than those of F+HDl, indicating the importance of tunneling in ultra-cold chemistry. Reaction rates of F+HCl increased by four orders of magnitude when the HCl molecule was promoted from its vibrational ground state to $v = 2$. Rotational excitations had less pronounced effects.

1.1.3   Lattice models and parallels with solid state physics

Lattice models, such as Hubbard models [89], have been used in condensed matter physics to explain the superfluid, superconductive, and the Mott-insulator phases. Atoms in optical lattice traps provides a physical realization of these models [90], and the ability to tune their interaction opened the door to the prospects of study-

ing controlled transitions between these important phenomena. The equivalent of pairing electrons in the so called BEC-BCS crossover believed to be responsible for the superconductive phase was observed in fermionic atoms [91–94]. The Mott-insulator to superfluid transition in atomic systems has also been observed [14, 95]. Developments of work with fermionic atomic species in optical lattices with two-atom occupation [96] might lead to simulations that yield the phase diagram of the original Hubbard model, a problem that has not lent itself to analytical description.

With extension to molecules, polar molecules can be placed in optical lattice for the important added advantage of strong off-site interaction. This would allow for the exploration of strongly correlated systems [34, 97, 98]. Micheli *et al.* [33] have shown that it is possible to engineer arbitrary interactions between neighboring polar molecules in optical lattices using a combination of direct and alternating electric fields. Optical shielding has also been shown to be possible [33]. Interesting physics is expected for polar molecules in optical lattices [36, 40, 99–101].

1.1.4   Quantum computing

The manufacture of the solid-state transistor heralded the age of modern electronic computers. Continuous miniaturization has allowed for faster, less energy inten-sive, and cheaper computers that have revolutionized every aspect of life. However, chip manufacturing is fast approaching the *quantum limit*. This is the limit in size when quantum effects become important and current computer technology will be insufficient. Recent advances in our understanding of cold and ultra-cold atoms and molecules, and developments in technologies to control and manipulate them, have allowed us to take advantage of this challenge to shift the paradigm of the process of computing itself. Quantum computers are an architectural proposal to exploit the quantum effect of superposition to introduce a form of parallel processing with potential for a phenomenal increase in processing speed. Quantum algorithms for currently intractable problems, such as integer factorization, indicate that solution of such problems might become feasible. In addition, quantum computers will be

capable of truly random processes, opening the door to accurate modeling of many physical processes.

Polar molecules are central to a promising new platform for the physical realization of quantum computers [102]. The bits of information, normally referred to as qubits, can be stored in long-lived hyperfine or rotational states of the electronic ground state. The strong dipole-dipole interaction increases the efficiency of binary operations necessary for a complete set of basic operations. The main practical challenge is decoherence, which compromises the fidelity of information storage and processing. Decoherence has many sources, but, cooling reduces contributions due to translational oscillation in the trap and occupation of undesired internal states.

1.2 Achieving cold and ultra-cold molecules

The workhorse of experiments to cool atoms to ultra-low temperatures, the *laser*, does not work for the vast majority of molecules. De-excitation of molecules populates many levels and the closed cycle (of a few levels) essential for laser cooling to work is absent. This has led to alternative cooling methods that can be categorized in two, direct and indirect methods. We will discuss some of the main methods of both categories beginning with direct ones. These discussions are not meant to be a comprehensive update of developments but an overview of some of the basic ideas behind a sample of representative methods.

1.2.1 Direct methods

Direct methods start with 'hot' molecules and cool them to low temperatures. Some direct methods, such as Stark [26] and optical lattice deceleration [103], are really slowing techniques and do not lead to increased phase-space density. However, other direct methods such as buffer-gas-cooling [104] do increase phase-space density. Direct methods such as evaporative [3, 105] and sympathetic cooling also used in the cooling of atoms increase phase-space density too. Direct methods have the advantage of reducing the internal as well as the translational energy of molecules.

Bethlem and Meijer reviewed developments in the production by direct methods and application of cold molecules up to 2003 [106]. We will begin by a brief discussion of the Stark effect which is at the heart of the most successful slowing techniques for molecules.

The Stark effect in molecules

The change in internal energy W of a molecule with dipole moment $\boldsymbol{\mu}$ placed in an external electric field $\boldsymbol{E}$ can be expressed as

$$
\begin{aligned}
W &= -\mu E \cos(\theta) \\
&= -\mu_{\text{eff}} E
\end{aligned}
\tag{1.1}
$$

where μ and E are the magnitudes of $\boldsymbol{\mu}$ and $\boldsymbol{E}$, θ is the angle between them and $\mu_{\text{eff}} = \mu \cos(\theta)$. Quantization of space limits μ_{eff} to a discrete set of values depending on the rotational state of the molecule. If the field is inhomogeneous the molecule experiences a force F_x in the x direction given by

$$
\begin{aligned}
F_x &= -\partial_x W \\
&= \mu_{\text{eff}} \partial_x W,
\end{aligned}
\tag{1.2}
$$

where ∂_x indicates the partial derivative with respect to x. States with a positive μ_{eff} feel a force in the direction of increasing field strength and are referred to as *high field seeking* (*h.f.s.*) states. Negative μ_{eff} states are attracted to low field regions and are thus *low field seeking* (*l.f.s.*). These forces are exploited in the design of equipment such as the Stark decelerator [26, 27]. The dependence of the force on μ_{eff} has been the basis for state selection in some experiments.

Stark deceleration

The use of fields to deflect [107] and focus [108, 109] atoms and molecules has a long history. However, the first successful use of fields to impart permanent change in longitudinal motion of molecules was reported by Bethlem *et al.* [26] in what they called a Stark decelerator. Theoretical accounts of the Stark decelerator have been made by Bethlem *et al.* [110] and Gubbels *et al.* [111] but we will give a simplified
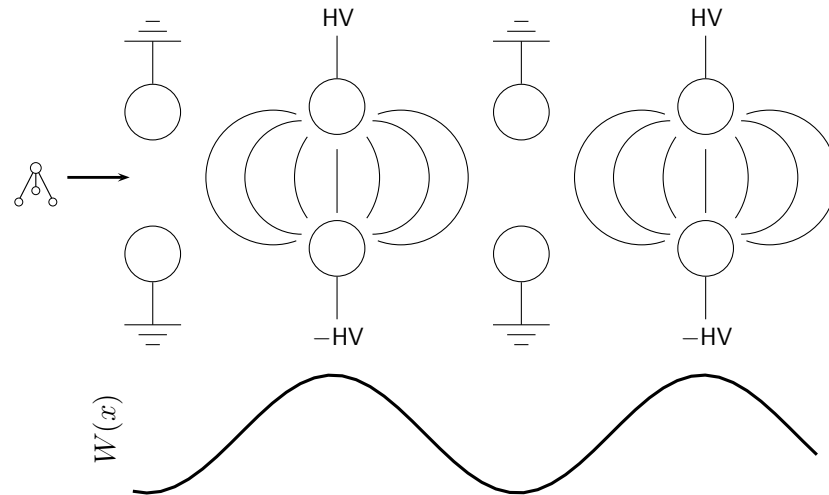
Figure 1.1: A schema depicting two stages of the Stark decelerator [26] and the profile of the interaction energy, $W(x)$, along the direction of travel chosen to be the x-axis.

account. The basic idea behind the decelerator is the use of a series of stages with a synchronized switching of fields. Each stage consists of two cylindrical rods with rounded edges. A high voltage is applied across the pair. Figure 1.1 is a schematic diagram showing two stages in sequence. We note that between two high voltage pairs is a set of neutral terminals. Figure 1.1 also shows a profile of the interaction energy $W(x)$ along the length of the decelerator, taken to coincide with the x-axis. On entering the field region, a low field seeking molecule will experience a potential hill, decelerating as it climbs. If nothing is done, and assuming that the molecule has enough energy, it will overcome the hill, accelerating and regaining all of its initial kinetic energy at the bottom. However, if the field is switched off before the molecule exits the stage, it will leave with less energy than when it entered. The amount of energy lost depends on the exact position of the molecule as the field is switched off. There are an array of stages and the process is repeated at each stage. The switching times of the stages must be synchronized taking into account the decreasing velocity of the molecules. The concept of a *synchronous* molecule defined as having just the right velocity to be in a similar position (same phase) on entering each stage is helpful. This molecule travels a distance exactly equal to the separation of the stages in one period. Molecules in the vicinity of the *synchronous* molecule

in phase-space are in stable orbits around it as they travel through the stages. We can imagine the molecules traveling together in a decelerating potential well, so that the motion is phase-space coherent. Those too far from the *synchronous* molecule have unstable phase-space trajectories and are lost during deceleration. Phase-space coherence is an important property of the Stark decelerator which allows for the deceleration of a slice of a thermal distribution as apposed to a single molecule.

Stark deceleration was first performed on metastable CO [26]. The velocity was decreased from 225 m/s to 98 m/s in 63 stages corresponding to a reduction of approximately 19% in energy. In 2009 Tokunaga *et al.* [112] reduced the velocity of LiH molecules to 53 m/s in 100 stages removing 98% of the kinetic energy in the process. Some of the molecules decelerated so far include ND_3 [28], OH [54,113,114], metastable NH [115], H_2CO [116] and SO_2 [117].

Stark deceleration will, in principle, work for any polar molecule as long as it is in a *l.f.s.* states. This is not because longitudinal deceleration is not possible for molecules in *h.f.s.* states, but, because of the transverse electric field pattern of the decelerator. The field magnitude along the perpendicular axis connecting the two electrodes of a stage has a minimum at the halfway point and increases closer to the electrodes. Molecules in *h.f.s.* states traveling along the decelerator would be defocused along this direction, eventually crushing into the electrodes. What makes the limitation to *l.f.s* states so restricting is the fact that the ground state of all molecules are *h.f.s.* states. In addition mixing of levels in heavy polar molecules of experimental interest, such as YbF [24,118] and PbO [66,119], results in virtually all low lying levels to become *h.f.s* at relatively low fields.

Alternating gradient deceleration

The alternate gradient (AG) Stark decelerator [27] is a development designed to decelerate molecules in both *h.f.s.* and *l.f.s.* states [120]. The AG Stark decelerator relies on an important physical phenomenon that the net effect of alternate focusing

and defocusing in a plane perpendicular to the direction of motion results in net focusing. Thus, alternating the field configuration so that the molecules are alternately focused and defocused in each of the perpendicular directions produces net dynamic focusing on the perpendicular plane. Bethlem *et al.* [27] achieved this by alternating the field configuration between stages. Each stage in the AG decelerator has four electrodes, producing a quadrupole field. The electrodes are at the vertices, away from the defocusing axis, which avoids loss of any molecules from collisions. The deceleration works as in the Stark decelerator except that the switching times have to be adjusted. The AG decelerator can be used to slow molecules in both *h.f.s.* and *l.f.s.* states.

In a proof-of-principle experiment Bethlem *el al* [27] demonstrated both acceleration and deceleration of metastable CO in a *h.f.s.* state. Subsequently AG deceleration has also been applied to OH radicals [121] and CaF [122]. Tarbutt *et al.* [118] have decelerated YbF while Wohlfart and colleagues have decelerated the much heavier benzonitrile [123]. The Stark and AG decelerators typically achieved temperatures of tens of mK, which are orders of magnitude higher than is required for condensation. This means that Stark deceleration can only serve as a first stage cooling method for experiments aimed at achieving condensation.

Buffer Gas Cooling

At temperatures of 1 K and below most gases have a very low vapor pressure, and cooling by containment in a cold container is impractical as the molecules would simply stick to the walls and condense. Helium is an exception. It has a relatively high vapor pressure down to subkelvin temperatures. Buffer-gas cooling (BGC) [104] employs He gas as a buffer between the walls of a cryogenic cell and the molecules of a gas to be cooled. For effective cooling the He must thermalize the gas to be cooled before its molecules touch the walls of the cell. This requires a minimum density of the He gas depending on the mean free path. Cooling efficiency can be increased by higher densities, however, this increases the vapor pressure, imposing a lower limit on the temperature. The cooled gas must be trapped for further cooling. For this

the cryogenic cell spatially coincides with a field used for the trap. As the molecules of the gas are thermalized, they fall into the trap and the buffer-gas is pumped out. Helium is essentially unaffected by the magnetic field due to its closed shell structure. The trap also stops diffusion of thermalized molecules onto the cell walls during the cooling process. The trap depth sets an upper limit on the temperature of the trapped molecules.

Buffer-gas cooling was initially used to cool atoms [124,125]. Pumping technology limited these early experiments to atoms with large magnetic dipole moments (6 μ_{B}). These atoms interacted more strongly to produce deeper traps and longer trapped lifetimes, stayed trapped just about long enough to allow for the evacuation of the buffer-gas. Improvements in pumping techniques eventually resulted in the BGC of atoms with smaller magnetic moments [126]. The first molecule to be cooled by BGC to mK temperatures was CaH [127]. Other molecules such as NH [128, 129] were subsequently cooled by this technique. In an interesting recent development BGC was used as the first stage of a process that achieved condensation of metastable ^{4}He [130].

Buffer-gas cooling has several advantages. It is a dissipative process which accepts the whole thermal distribution which results in a comparatively high number of cold molecules. Up to 10^{12} NH molecules have been cooled [129]. The technique is not dependent on the internal structure of the gas to be cooled and is therefore of quite general application. This could allow simultaneous cooling of different species as long as they can be trapped magnetically. However, BGC only achieves temperatures of the order of mK.

Optical lattice deceleration

Identical counter-propagating laser beams can be used to create a potential lattice for trapping atoms and molecules [131]. The lattice can be made to travel at constant speed if we change the frequency of one beam. Let us imagine suddenly switching-

on a traveling lattice to capture a bunch of molecules from a pulsed supersonic beam in one of the potential wells. The number of captured molecules will depend on the laser spatial and intensity profile, the relative molecule to lattice velocity, and the beam temperature. In the frame of reference of the lattice, the molecules will eventually decelerate, and, if the well is deep enough, be reflected back in the opposite direction. If however, we switch the laser off just as the molecules are at the turning point, we could bring them to a standstill in the lattice frame. The use of a lattice to reflect molecules in this way was suggested by Ryytty and Kaivola [103]. In practice the molecules in an ensemble will of course enter the trap at different points in phase and will not be at their turning points simultaneously. The reduction in beam velocity depends on the relative beam to lattice velocity. Ideally, we would have a lattice stationary in the lab frame. Also it would be preferable to have deep wells to capture many and hotter molecules. However, for a fixed potential depth, a higher relative speed reduces the fraction of molecules that can be captured. In a theoretical study, Dong *et al.* [132] found that the optimal lattice velocity for a maximum fraction of nearly stationary molecules to be half the molecular beam velocity. Optical deceleration slows and bunches molecules in velocity space at the expense of spatial distribution as required by conservation of phase-space density. Like the Stark decelerator, optical lattice deceleration is phase-space coherent.

Optical lattice deceleration relies on induced, as opposed to a permanent, dipole moment. Since all molecules (and atoms) are polarizable to some degree, optical lattice methods are in principle quite general. The constant lattice velocity method generally produces deep minima (100 K) for short durations (nanoseconds) using a pulsed laser beam to impart the required impulse. In a second variable method the lattice is decelerated by chirping one of the lasers. Decelerating lattices have shallower (1 K) minima but last longer (minutes). The deeper wells demand laser light at least two orders in magnitude more intense. The decelerating lattice has the disadvantage that it will also decelerate the molecules of the carrier gas employed in the production of the beam. The constant velocity lattice has the advantage that it can separate the molecules as long as there is a significant difference in the

mass-to-polarizability ratios of the two species [132].

Fulton et al. [133] have slowed a beam of NO at temperatures of 1.8 K from 400 m/s to 270 m/s, corresponding to a 50% reduction in kinetic energy, using a constant velocity optical lattice. They found that allowing for a half rotation in phase space retained the original velocity distribution.

Sympathetic cooling

At times it is not possible to apply a cooling technique directly because of quantum statistics or complicated internal structure of the molecules. Sympathetic cooling, developed initially to cool ions, and which promises very low temperatures, can be used in some such cases. The gas to be cooled is simultaneously trapped with a second species which is usually cooled by laser. Cooling proceeds by thermalization. Although less effective for neutral species, because they interact less strongly than ions, sympathetic cooling by rubidium atoms was used to achieve the condensation of ^{41}K [134]. Theoretical studies have considered the prospects of sympathetic cooling of OH [135, 136] by Rb and found them to be poor. More recent considerations of cooling NH_3 and ND_3 [137,138] by Rb and NH [139–141] by alkali-metal and alkaline-earth atoms indicate rather mixed results. Sympathetic cooling of ammonia by Rb is likely only for the ground state [137] of the molecule while cooling NH by Mg has good prospects [141].

1.2.2   Indirect methods

Indirect methods begin with laser-cooled atoms and associate them to form molecules. Association can be achieved optically [48, 49], magnetically [142, 143], or by three-body recombination. Indirect methods have the advantage of producing molecules with translational temperatures similar to the parent atoms. Until recently these molecules were highly vibrationally excited. Recently, heteronuclear molecules have been produced in their vibrational ground state by coherent photoassociation [144]. Here we will discuss homonuclear and heteronuclear photoassociation, magnetic as-

sociation by Feshbach resonance tuning, and enhanced association by three-body recombination.

Photoassociation

If two atoms collide in the presence of a photon they can be promoted to a bound state of an excited electronic potential energy curve (hereafter PEC). The photon has to be of the right frequency corresponding to the energy difference between the scattering and bound states. Photoassociation (PA) of atoms by laser light in the cold regime was suggested by Thorsheim *et al.* [48]. Fioretti *et al.* [49] recorded the first PA of Cs_2, and a little over half a decade later homonuclear diatomic molecules had been produced from most of the alkali-metal atoms [51, 145, 146]. The long-range nature of low-energy scattering states means that overlap with deeply bound vibration states, which have a short classical turning point, is virtually zero. The Franck-Condon factors invariably dictate PA to highly excited vibrational states, which quickly dissociate back to a scattering state, or, drop down to a vibrational state of the electronic ground state. The latter outcome is less likely for the same reason that PA is more likely to produce a molecule in a highly excited vibrational state. Even when relaxation (de-excitation) results in a bound state, it is invariably vibrationally highly excited. These states are undesirable in trapped molecules because collisional relaxation, even near dissociation, releases enough kinetic energy to eject the colliding pair out of the trap. Stabilization to the ground state is therefore important. The relaxation process need not be spontaneous, and coherent transfer to deeper vibrational levels can be achieved by stimulation [147]. In the latest schemes, chirped lasers are used to create a tailored wavepacket on the excited curve increase PA yields greatly [148–150].

Homonuclear molecules

Trapped alkali-atoms are usually in *spin-stretched* electronic states, which means that the scattering state is a triplet state. The leading term in the long-range potential of the electronic ground-state of both homonuclear and heteronuclear alkali metal dimers has an R^{-6} dependence. In contrast, excited electronic states

of homonuclear dimers have an R^{-3} dependence. This leads to a denser bound-state structure at high vibrational levels, which can be advantageous in relaxation, however, the difference in the long-range behavior of ground and excited electronic states leads to poor Frank-Condon factors. Also the hyperfine interaction only weakly couples *gerade* and *ungerade* symmetry states. This makes it challenging to transfer *ungerade* scattering states of the $^3\Sigma_u$ PEC to *gerade* bound-states of the $X^1\Sigma_g$ ground state PEC. Nonetheless, transitions were observed by Samelis *et al.* in 2000 [151]. Nikolov *et al.* [152] reported the formation of K_2 in their absolute ground states ($X^1\Sigma(v=0)$) by a two-step method. They photoassociated a scattering state to a highly excited $5^1\Pi_u$ or $6^1\Pi_u$ state via an intermediate $v=89$ level of a $1^1\Pi_g$ curve. The second step is an efficient bound-to-bound transition. The higher excited state has an inner turning point above the absolute ground state, giving favorable Franck-Condon factors. More recently, Viteau *et al.* [153] reported ground-state Cs_2 by PA. Their method was essentially a redistribution of the vibrational occupation by optical pumping. They excited molecules using a shaped, broadband, laser pulse tuned to transitions between several vibrational levels of ground and electronically excited states. Frequencies that could excite the $v=0$ ground state were removed so that it became a 'dark-state'. The molecules are then allowed to decay spontaneously, occupying all levels including $v=0$. Population transfer to the $v=0$ levels of the ground state can then be effected by a sufficient number of absorbtion-emission cycles. Viteau *et al.* [153] reported a transfer of over 50% of molecules from $v=1-10$ levels to the ground state $v=0$. In a different approach, Koch *et al.* [154] have proposed tailoring a laser pulse by using control theory to optimize transfer of weakly bound electronic ground state molecules to the absolute ground ($v=0$) state. A bound initial state is required to ensure that the optimization process can guarantee the existence of an optimum solution. There must, of course, be a route of transitions connecting the initial and final states. Koch *et al.* [154] simulated optimal control transfer of long-range Na_2 molecules to $v=0$ for a simplified two channel model and reported 99 percent efficiency.

Heteronuclear molecules

For heteronuclear alkali metal dimers the excited and ground electronic states both have an R^{-6} long-range dependence. Theoretical calculations by Wang and Stwalley [155] showed this similarity to lead to much better Franck-Condon factors which improved with increasing mass. They also noted that the turning point of the least-bound state of the excited electronic state was much further out (at ≈ 100 Å) for KRb than other heteronuclear dimers, pointing to better PA prospects for KRb. In 2004, Stwalley [156] noted a very fortuitous mixing of the $b^3\Pi$ and $2^1\Sigma$ states, the two lowest curves of the first excited electronic state. This mixing, which is present in all heteronuclear alkali metal dimers, and is stronger for heavier systems, allows for efficient transitions to and from the ground *singlet* and *triplet* states. Stwalley [156] reported the existence of a mixed character bound-state with four turning points resulting from two avoided crossings of the curves above the ground $v = 0$. Such a state makes for an ideal intermediate level in efforts to achieve ground state $v = 0$ molecules. Kotochigova *et al.* [157] studied transition dipole moments between the two ground-state potentials and the mixed excited state of KRb. They found the excited state to have *triplet* character in the short-range and *singlet* character in the long-range. At an avoided crossing and turning point ($R \approx 10a_o$) there was strong mixing. They affirmed the feasibility of a single step two-photon scheme to achieve ground state KRb in $v = 0$. Another factor improving the PA efficiency of heteronuclear dimers is the lifting of parity restrictions.

In 2005, Sage *et al.* [158] reported ground state $v = 0$ RbCs molecules achieved by a two-steps process in a relatively low density sample. In 2008, Ospelkaus *et al.* [144] reported the first observation of absolute ground-state KRb. They employed a two-lasers to coherently transfer loosely bound Fermionic Feshbach molecules to the $v = 0$ of the ground electronic state. The molecules were at temperatures below 400 nK, which is three times higher than is required for degeneracy. In 2008, Deiglmayr *et al.* [159] reported LiCs in the ground state $v = 0$ produced using a single PA step followed by spontaneous emission. The excited state belonged to the $B^1\Pi$ potential

energy curve, the highest of the first excited electronic asymptote. The essential science, applications, and developments in PA of alkali-metal atoms until 2006 has been reviewed by Jones *et al.* [53].

Feshbach Resonance Association

Each spin configuration of a colliding pair of alkali atoms defines a channel. In a first order picture, each of these channels supports its own bound states. It is therefore sensible to talk about the channel that supports a given bound state. In the complete system the *hyperfine* interaction couples the different channels, mixing the character of the bound states. Only states belonging to the lowest threshold remain truly bound, the others retain their bound-like character (localization) but are *quasi-bound* or *resonance* states with an associated dissociation lifetime. In the vicinity of a *resonance* state, scattering cross sections exhibit pronounced sensitivity with change in energy. Resonance states are *Feshbach* (*shape*) if they are supported by a different (the same) channel as the scattering state. This means that Feshbach resonances generally have different magnetic moments to the scattering state. The difference can be exploited to tune scattering properties of ultra-cold [142, 160] and degenerate [161] systems. Importantly, atoms of a condensate can be associated to produce a *molecular* BEC, as pointed out by Timmermans and colleagues [143].

There are several approaches to associating atoms. The most common one involves sweeping the resonance across the scattering state, resulting in the transfer of colliding atoms to a bound state. With a linear time-dependent magnetic field, the avoided-crossing of the scattering and resonance states is described well by a Landau-Zener curve crossing model [162]. The probability of transition to a bound state, P_t, can be expressed as

$$P_t = 1 - \frac{1}{\exp(\delta)}, \tag{1.3}$$

where δ is inversely proportional to the rate of change of the magnetic field. In the zero δ, or *adiabatic*, limit, P_t approaches unity. Although in practice the probability for any pair is very small, each atom can pair with any other in the ensemble,

depending of course in the phase-space density. The number of pairs is proportional to the number of atoms, resulting in an appreciable chance of binding. The first diatomic molecules from degenerate Fermionic species were created by this method [163]. The Pauli exclusion principle forbids s-wave collisions of identical Fermionic species in the same internal state. Therefore, *ultracold* Fermionic dimer association requires mixed species or mixed internal states. In this first experiment, Regal *et al.* [163] prepared the ^{40}K atoms in the same total internal angular momentum state, $f = 9/2$, but in different projection quantum numbers, $m_f = -9/2$ and $-5/2$. They detected the molecules indirectly by an atom count and directly by resonant coupling of the molecular state to the $|f = 9/2, m_f = -7/2\rangle$ atomic state. By applying a magnetic field gradient, they were able to selectively probe atoms from the dissociation of the dimers. Subsequently, other Bosonic [164–166] and Fermionic [163, 167, 168] atoms were associated by tuning across Feshbach resonances.

Another association mechanism is three-body recombination. When two atoms collide they can bind permanently if a third body is present to carry away the excess energy released by binding. Such three-body recombination requires high densities. However, near a Feshbach resonance, three-body recombination is enhanced [169]. Such enhancement was exploited to associate ^{6}Li atoms from a Fermi-degenerate gas to create a molecular BEC of ^{6}Li$_2$ by Jochim and colleagues [170]. Cubizolles *et al.* [168] reported association efficiencies of 85%, by three-body recombination, of Fermi degenerate ^{6}Li atoms. The resulting Bosonic molecules were in the *ultracold* regime but not degenerate. They also demonstrated the reversibility of the association process by recovering all the atoms. Three-body recombination can be viewed chemically as an equilibrium between exothermic 3-atom collisions, which result in dimer formation, and competing endothermic atom-molecule collisions, that dissociate the dimers.

In a novel approach, Donley *et al.* [171] applied two rapid pulses of magnetic field with a constant near-resonant field, B_{dc}, between the pulses. The first pulse *non-*

adiabatically mixed the scattering and molecular states. They observed dramatic oscillations in the number of atoms in the BEC between the pulses. The oscillation frequency depends on the dimer binding energy [172]. They measured the frequency for different binding energies by changing B_{dc} and found excellent agreement with theoretical prediction. Thompson *et al.* [173] associated ^{85}Rb atoms by applying a small sinusoidal oscillation to a constant field tuned close to a Feshbach resonance. Photons from the oscillating field stimulate the scattering state into emitting a very low frequency photon corresponding to the energy of the bound state. The authors observed Rabi-like oscillations between the atomic and molecular states. The oscillations were damped over the lifetime of the molecules. This approach has the advantage of avoiding resonant fields with characteristic heating and inelastic collisions. The physics and developments relating to Feshbach resonances in ultra-cold and degenerate atoms up to 2006 has been reviewed by Köhler *et al.* [174].

1.3 Ultra-cold collisions

The kinetic model is a central pillar of our understanding of gases because for a wide range of temperatures the details of the interaction of pairs of atoms or molecules are not important. Collisions can be treated classically as between *hard balls*. In quantum gases, where atoms and molecules are waves and can extend over regions that exceed their average separation, understanding the details of binary interactions is crucial to understanding the properties of the gas. Collisions can lead to chemical reaction or nonreactive elastic or inelastic scattering. We have seen that chemical reactions at ultra-low temperature have novel mechanisms and offer fascinating prospects of coherent control. Inelastic collisions have a strong bearing on the prospects of trapping, and by extension, cooling of molecules to ultra-cold temperatures. There are several mechanisms responsible for trap loss. Collisions can cause a reorientation of the electric or magnetic dipole moment, resulting in transitions to untrappable states. As the ground state is always *h.f.s* but static fields can only trap *l.f.s* states, transitions to at least one untrappable state will always be energetically favorable. A second mechanism is the transfer of internal energy

to relative motion of the colliding partners. Even relaxation between highly excited vibrational states will release sufficient energy to kick both partners out of the trap. Trap loss can also result from chemical reactions.

Molecules can rotate, vibrate, and have fine and hyperfine structure which depends on the orientation of the electronic and nuclear spins. There are a few general principles that form a useful guide to our understanding of inelastic collisions. Rotational relaxation of molecules depends on the anisotropy of the interaction energy and the rotational constant of the molecule. Higher anisotropy and lower rotational constants increase rotational quenching. Vibrational quenching increases with increased sensitivity of the interaction to the vibrational coordinates. For ground state $^2\Sigma$, reorientation of magnetic dipole moment (or *spin flipping*), during collisions with structureless atoms is due to coupling of spin states to rotational levels via the spin-rotation interaction, and the coupling in turn of different rotational states by the potential anisotropy [175]. Molecules of $^3\Sigma$ ground state experience deeper traps for the same magnetic field configuration. However, the spin-spin interaction mixes the rotational states so that the ground state is no longer a pure $N = 0$ state (where N is the rotational quantum number), and the interaction anisotropy plays a more direct role in *spin flipping*. Therefore, Zeeman relaxation is faster for $^3\Sigma$ molecules, with the efficiency proportional to the square of the ratio of spin-spin to rotational constant [176–178]. Stronger spin-spin, spin-rotation, higher potential anisotropy, and lower rotational constants all increase Zeeman relaxation.

Potential anisotropy couples different Stark levels directly. Thus, electric dipole reorientation is generally much more efficient than the magnetic counterpart for polar molecules. Zeeman relaxation will also be generally faster in polar molecules than in non-polar molecules. The stronger interactions of electric dipole moments result in deeper wells which support more resonances. Increased degrees of freedom such as spin, rotational or vibrational motions increase the number of channels, increasing the number of Feshbach resonances. As a general rule, strongly interacting

and heavier systems have a denser set of levels increasing both shape and Feshbach resonances, with detrimental effect on trap stability.

Although cold and ultra-cold collisions are fully quantum mechanical, making them counterintuitive, they have several advantages. Collisions in the low-energy limit are dominated by a single partial wave (S-wave), significantly simplifying the analysis. The long-range nature of the wavefunction means that away from resonances, the long-range character of the potential plays a dominant role. Useful insight can be gained by dividing the radial separation of the colliding partners into long and short ranges. Our detailed understanding of the internal structure of atoms and molecules, and knowledge of the long-range interactions, furnishes our capacity to understand, in great detail, cold and ultra-cold collisions. On the other hand, the richness of even the simplest atoms and molecules poses great challenges. For example, the number of channels and the interplay between them quickly results in intricate complexity that not only becomes impossible to reproduce completely by computation, but might render results difficult to interpret.

Apart from causing trap loss collisions are central to thermalization. The efficiency of important cooling techniques such as buffer-gas cooling [104], evaporative cooling [3, 105], and sympathetic cooling [179] depend on collision properties. In particular elastic collisions are required to dominate in order to ensure the cooling process is faster than trap loss due to inelastic collisions. The indirect methods of optical and Feshbach association of atoms are also outcome of collisions, albeit in fields. In order to master these processes and understand and manipulate gaseous matter at these low temperatures, it necessary to understand collisions under appropriate conditions. The challenge is essentially to determine the dependence of collision outcome on the internal states of the colliding partners, their interaction, and on applied static and time varying fields. We will sample efforts to understand dependence on some of these factors.

1.3.1   Inelastic atom-diatom collisions

The bulk of current experimental and theoretical work, including our own research, is on atom-diatom collisions, reflecting the young stage of the field. Early calculations [180–184] of cold and ultra-cold collisions were motivated by astrochemistry, and involved the most abundant elements in the universe, H and He. In a study of vibrational relaxation of H_2 by collisions with H, Balakrishnan *et al.* [181] found an increase of seven orders in magnitude of the rate constant resulting from vibrational excitation of H_2 from its ground state to $v = 12$. In collisions of H_2 with ^{3}He and ^{4}He [183], the same authors found that rate coefficients increased by three orders of magnitude as the initial vibrational levels v is increased from 1 to 10. They also noted that the relaxation rates exhibited a minimum at a collision energy of approximately 10 K, corresponding to the interaction well depth, before attaining a limiting value in accordance to Wigner's threshold laws [71] below 10^{-3} K. Forrey *et al.* [185] considered vibrational relaxation of trapped molecules via direct collisional quenching and vibrational pre-dissociation. They found direct collisional quenching to dominate at low atom densities. At higher densities transient van der Waals states of the complex become important. Significantly, they found that for any given vibrational state of the molecule, the least-bound state of the collision complex controls the vibrational relaxation.

Demonstration of BGC motivated research into low vibrational collisions of polar [175, 177, 186–196] and non-polar [197–200] diatomic molecules with He. Balakrishnan *et al.* [186] considered vibrational quenching of $CO(v = 1\ j = 0, 1)$ in collisions with ^{4}He and found shape resonances to influence the quenching rates significantly at energies less than the well depth. At low energies, they found near dissociation Feshbach resonances, supported by the $j = 1$ levels of both $v = 0$ and 1, to dramatically affected both the elastic and rotational quenching rates from the $j = 1$ levels. In contrast, for collisions of ^{3}He-$CO(v = 0, 1\ j = 0, 1)$, Zhu and colleagues [187] found the corresponding Feshbach resonances to be absent, and the quenching rates to be much smaller. Experimental results at ultra-low tempera-

ture are very limited, but, at energies corresponding to $T > 35$ K Balakrishnan *et al.* [186] and Zhu *et al.* [187] found their calculations to be in good agreement with experimental observations [201]. Bodo *et al.* [202] extended the work of Balakrishnan *et at.* [186] by considering relaxations of the second excited vibrational state of CO in collisions with ^{4}He. They found relaxation rates corresponding to $v = 2 \rightarrow 1$ to dominate the $v = 2 \rightarrow 0$ rates in the cold regime, and to be two orders of magnitude greater in ultra-cold regime. These results applied to different initial rotational levels. Bodo and Gianturco [191] did a comparative study of vibrational cooling of the polar molecules LiH, CO, and HF in initial states ($v = 1, 2$ $j = 0$) by collision with He. They found that of the three molecules LiH would be the best candidate for BGC. Stoecklin *el al.* [194] considered ro-vibrational quenching of HF($v = 1$) in collisions with ^{3}He at ultra-low energies. They found pure rotational quenching to be much more efficient than pure vibrational quenching. This is due to the high anisotropy and relatively weak dependence of the He-HF interaction on the separation of the hydrogen and fluorine atoms in HF. Balakrishnan *et al.* [196] found similar results in collisions of CaH with He. Balakrishnan *et al.* [196] also found that the spin-rotation interaction, although small, significantly influences the rotational quenching at temperatures below 10 K. Volpi and Bohn [200] found $^{17}O_2$ to be reasonably robust against Zeeman relaxation, even at higher vibrational levels, but warned that trapping magnetic fields would lift the degeneracies and reduce the robustness. Motivated by the prospects of sympathetic cooling, Lara *et al.* [135, 136] studied collisions of cold and ultra-cold Rb with NH and found high propensities for NH to change internal state. Żuchowski and Hutson performed cold and ultra-cold collision calculations of Rb-NH_3/ND_3, focusing on molecules initially in the upper level of the inversion doublet for ($j = 1, k = 1$), which is *l.f.s* [137]. They found inelastic rates to the lower level of the inversion doublet to preclude sympathetic cooling of ammonia in the upper state. However, they reported good cooling prospects for *h.f.s* states, even when Rb is in a magnetically trappable *l.f.s* state.

Quasi-resonance is the enhanced efficiency in the transfer of rovibrational en-

ergy between specific rovibrational states. It is an important phenomenon in rovibrational relaxation. Stewart *et al.* [203] and Magill *et al.* [204] observed quasi-resonance at thermal temperature in experimental investigations of atom-diatom collisions in 1988. They reported significantly enhanced transitions between levels related by $\Delta J = n\Delta v$, where $n = 2$ or $n = 4$, and ΔJ and Δv are the changes in the J and v quantum numbers, respectively. Forrey and colleagues [205] showed quasi-resonances to occur at cold and ultra-cold temperatures with more pronounced effect as temperature is reduced. Similar observations were made by Balakrishnan *et al.* [198] in rovibrational quenching of O_2 by collisions with ^{3}He. The increased impact of quasi-resonance at lower temperatures is due to the increased collision time. In particular, the collision time becomes progressively longer than the rotational period as the collision energy is reduced. Tilford *et al.* [199] found rapid pure rotational relaxation of all levels of O_2 in a He buffer-gas at cold and ultra-cold temperatures. Florian *at al* [192] compared quenching of the polar molecule CO to O_2 by collisions with He and found quasi-resonance to be more important in CO. They also reported relative stability of some rotationally excited levels in regions were quasi-resonance was forbidden, raising prospects of stable polar "super rotors" previously investigated by Forrey [206]. These so called "super rotors" are predicted to exhibit interesting quantum phenomena [207–209]. In a study of ultra-cold collisions of OH with He, González-Sánchez *et al.* [195] found rotational relaxation to be much more efficient than elastic collisions.

The achievement of photo and magnetoassociation provided another impetus to research in collisional quenching. Early experiments involved homonuclear alkali metal gas samples and produced translationally ultra-cold but vibrationally highly excited diatomic molecules. However, calculations involving highly vibrationally excited states are very expensive because they required the inclusion of a large number of open channels. In addition, even calculations of nonreactive collisions potentially required inclusion of closed, single, and double, continuum states to which highly excited states would be coupled [210]. For this reason, many early calculations were limited to low vibrational levels. These generally showed vibrational quenching to

be much faster than elastic scattering [211–215], consistent with experimental observations [216–219]. Experimental results on Cs-Cs$_2$ [220], for the high $v = 32 - 47$ and low $v = 4 - 6$ levels, showed the quenching rates to be largely independent of vibrational and rotational excitation. More recently, calculations of vibrational quenching of homonuclear Li atom-diatom systems by Quéméner *et al.* [210] showed vibrational quenching to be particularly efficient for both high and low vibration levels when the scattering length is negative and small. The quenching rates showed strong but irregular dependence on the vibrational levels. They also reported the need to include many continuum states to obtain convergence for the highly excited vibrational states.

Interestingly, highly vibrationally excited molecules produce from Fermionic atoms were found to be remarkably stable to collisional trap loss [167–169, 221]. Petrov and colleagues [222] explained this phenomenon in terms of Pauli blocking, also observed in a gas of atomic ^{40}K by DeMarco and colleagues [223]. Essentially, the atoms making up the highly excited molecule preserved their individual identity sufficiently as to be subjected to the Pauli principle, which forbids S-wave collisions with the atoms of the surrounding gas. Cvitaš *et al.* [213], in a comparison study of Bosonic and Fermionic atom-diatom Li systems, showed that there was no systematic suppression of quenching for lower vibrational levels in either. A few months latter Quéméner *et al.* [215] found similar results for the $v = 1$ levels of Fermionic and Bosonic K-K$_2$ collisions.

1.3.2 Sensitivity of collision dynamics to the potential energy surface

The interaction energy is the most significant determinant of collision outcome, and, numerous studies have explored the sensitivity of collision dynamics to the details of the potential energy surface (PES). In a comparative study of two potential energy surfaces of He-H$_2$, Lee *et al.* [224] found significant differences in the inelastic scattering. For the quenching of the first excited state of H$_2$, the difference was up to 3

orders of magnitude. The differences was less drastic for elastic and pure rotation quenching. Cybulski et al. [193] found that minute variations in the analytic potential of He-NH, resulting from different fitting procedures, gave rise to a difference of up to 50% in Zeeman relaxation rates. In a study of collisions between spin-polarized Na-Na$_2$, Soldán et al. [211] found an order of magnitude difference in $v = 1 \rightarrow 0$ transitions between pairwise additive and nonadditive surfaces. Quéméner et al. [212] studied sensitivity to three-body interactions at short distance of the same system and found similar sensitivity of the $v = 1$ levels. They found that changes of 1% in the three-body interaction can result in up to 75% difference in cross sections. They also reported pronounced sensitivity of the rotational distribution to the three-body interaction, even for quenching of the $v = 2$ and 3 levels. In a more recent study, Cvitaš et al. [214] studied the sensitivity of ultra-cold collision dynamics of Li-Li$_2$ to the three-body interaction. Three-body nonadditive forces between spin-polarized alkali metal atoms can change well depths by up to a factor of 4, and equilibrium inter-atomic distances by more that an Ångström [225].

In a systematic survey of interactions of NH$_3$ with alkali-metal, alkaline-earth, and Xe atoms, Żuchowski and Hutson [138] found the interactions to have deep minima and strong anisotropies, leading them to conclude that sympathetic cooling is likely to work only when both atom and molecule are in their ground state. However, in ultra-cold collision calculations of Rb-NH$_3$ and Rb-ND$_3$ [137] the same authors found that sympathetic cooling of molecules in *h.f.s* states by magnetically trapped atoms might actually be possible. In a similar study, Soldán et al. [139,140] investigated the interaction of alkali-metal and alkaline-earth atoms with NH. They found interactions with alkali-metals to be highly anisotropic and ion-pair states to be accessible even at low temperatures, introducing the possibility of chemical reaction. The interaction with alkaline-earths was predictably less anisotropic. However, for Sr-NH and Ca-NH the anisotropy was still much higher than the rotational constant of NH. For Be-NH and Mg-NH they found the anisotropy to be comparable or less than the rotational constant of NH. In addition the ion-pair states crossed the dispersion-bound states behind the repulsive wall of the dispersion surface, making

the crossings energetically inaccessible at low energies. They concluded that Mg and Be are promising candidates for sympathetic cooling of NH. Collision calculations supported this conclusion for Mg-NH [141].

1.3.3   Collisions in fields

The study of collisions in fields is a necessity. As we have seen, trapping in electric, magnetic or electromagnetic fields is a prerequisite for achieving and maintaining ultra-cold temperatures. Thus practically all collisions take place in the presence of fields. The suitability of molecules for magnetic or electrostatic trapping and cooling is determined by collision properties in fields. Atom-diatom collision calculations involving the He atom and O_2 [226] and NH [177, 193] in magnetic fields and CaH [227], CaD [228, 229], OH [230, 231], and YbF [232] in combined electric and magnetic fields have looked mainly at the efficiency of Zeeman relaxation compared to elastic collisions. Volpi and Bohn *et al.* [226] considered ^{3}He-$^{17}O_2$ and found that spin relaxation could be suppressed by setting the Zeeman splitting of entrance and exit channels at less than the centrifugal barriers. Krems *et al.* [177] found elastic collisions to be five orders of magnitude higher than Zeeman relaxation for temperatures between 0.5 and 1.0 K, indicating NH as a good candidate for cooling by ^{3}He buffer gas. Their cold collision rates were consistent with recent measurements [129]. In a combined experimental and theoretic study, Campbell *et al.* [178] studied collisions of ^{3}He and ^{3}He with four stable isotopomers of NH. Their results for ^{4}He supported the inverse proportional dependence of Zeeman relaxation rates on rotational constant of NH as predicted [176, 177]. Relaxation rates involving ^{3}He were significantly higher and did not follow predicted dependence. They put this down to a shape resonances. Cybulski *et al.* [193] found the elastic cross sections to be insensitive to the magnetic field from 0 up to about 3 Teslas, while the Zeeman relaxation increased rapidly in the ultra-low regime. As part of a systematic study of the prospects of sympathetic cooling NH by laser-cooled alkaline-earth and alkali-metal atoms, Wallis and Hutson [141] performed scattering calculations of ultra-cold Mg with NH in a magnetically trappable state. They found NH to be stable against Zeeman relaxation for temperatures ranging from the ultra-cold up

to 10 mK, pointing to promising prospects for sympathetic cooling of NH by Mg.

The use of combined electric and magnetic fields allows greater control of collisions. Calculations of collisions of He with CaH [227], CaD [227, 228] and OH [231] showed it was possible to effectively suppress spin-changing collisions by a combination of electric and magnetic fields. Tscherbul and Krems [227] showed this suppression to extended up to cold temperatures. They found that the electric field can shift the start of the Wigner regime to lower energies by coupling states of different parity. Abrahamsson *et al.* [228] crossed a *h.f.s* Zeeman state of the first excited rotational level of CaD with a *l.f.s* level of the ground state using a magnetic field and induced an avoided-crossing by applying an electric field coupling the states. They were able to observe enhanced Zeeman transitions as they tuned the magnetic field near the crossing. Therefore, combining fields was used not only to induce but also to enhance an otherwise forbidden transition. The relative orientation between the electric and magnetic fields is an additional control parameter which can break symmetry, mixing states, and inducing transitions [227, 228]. It can also be used to change the position of an avoided crossing [227,228]. Tscherbul and Krems [227] and Abrahamsson *et al.* [228] have suggested that combined fields could be used to induce non-adiabatic spin transitions and spin-forbidden chemical reactions. Tscherbul *et al.* [231] found spin relaxation to be effectively suppressed by moderate fields of 10 kV/cm at collision energies below 10 mK for ^{3}He-OH collisions. Pavlovic *et al.* [230] found that fields of less than 15 kV/cm were sufficient to enhance Stark relaxation of OH in specific internal states by three orders of magnitude. They observed rich resonance structure tunable by electric field strength. The sensitivity to electric field strength reduced with increased rotational excitation. Elastic scattering dominated over relaxation processes for ^{4}He-OH collisions and varied monotonically with reducing energy. The cross sections changed smoothly across threshold, in disagreement with an experimental observation [233] made earlier. Alyabyshev and Krems [234] considered the effects of a microwave laser on Zeeman relaxation of CaH by collisions with He in the presence of a magnetic field. They demonstrated that the frequency and intensity of the laser field could be used to effectively tune collision

cross sections.

1.3.4 Molecule-molecule collisions

As denser samples of molecules are realized [235–238] it is important to understand molecule-molecule collisions. Calculations [239–243] showed that the collision outcome between polar molecules could be influenced by electric fields. Stark relaxation was found to be efficient, indicating poor prospects of evaporative cooling in electrostatic traps. The stronger interaction between polar molecules also results in a denser resonance structure [119], posing a challenge to trapped lifetimes. Avdeenkov and Bohn [239–241] showed that the dipole-dipole interaction can be tuned using electric fields to produce long-range minima and barriers, which could suppress inelastic collisions [244]. Avdeenkov *et al.* [244] showed that high electric fields could be used to suppress inelastic collisions driven by the dipole-dipole interaction in $^1\Sigma$ molecules. Scattering properties of OH molecules showed remarkable independence to the short-range details of the interaction at ultra-low energies. The authors attributed this behavior to avoided crossings in the long-range adiabatic potential energy curves [239]. Avdeenkov [245] considered stability of polar molecules in microwave traps and concluded that evaporative cooling in such traps has good prospects. Ticknor [246] demonstrated a universal regime at the high-field limit where collisions are characterized by the mass, induced dipole, and the energy of the colliding partners.

In collision calculations of OH in a magnetic field, Ticknor and Bohn [247] reported two orders of magnitude suppression of inelastic collisions in *l.f.s* states by fields of several thousand Gauss. For collisions of NH in their rotational ground state in a magnetic field, Kajita [248] reported the inelastic cross sections to be two orders of magnitude less that elastic cross sections, indicating good prospects for evaporative cooling of NH. Tscherbul *et al.* [249] found efficient Zeeman relaxation in O_2-O_2 at cold temperatures for magnetic fields exceeding 10 Gauss. In the

ultra-cold regime, the spin-relaxation cross sections are dominated by Feshbach resonances, with densities of up to 100 resonances per Tesla. They found the density of resonances to reduce by up to a factor of 10 for the ground compared to excited spin states.

Following the achievement of dense samples of ground state $^{40}K^{87}Rb$, Ni *et al.* [237] demonstrated the strong effect that modest electrostatic fields can have on dipolar molecule-molecule collisions. These molecules are fermions and react by tunneling through the P-wave barrier. Nonetheless, Ni *et al.* [237] were able to induce chemical reactions, leading to pronounced loss rates. Reactions showed a strong power dependence on the dipole moment, consistent with theoretical predictions [250]. Collisions of $^{40}K^{87}Rb$ molecules prepared in different internal states, and with ^{87}Rb or ^{40}K atoms, showed a 10 to 100 times increase in reaction rates [238]. Ospelkaus *et al.* [251] demonstrated control of the hyperfine interaction by preparing molecules in a single hyperfine state. They used a two-photon scheme that should allow any bialkali polar molecule to be prepared in an arbitrary superposition of hyperfine states. The transitions depended on the electric nuclear quadrupole moment and coupling to rotationally excited states as predicted by Aldegunde *et al.* [252].

1.4   Feshbach resonances and control

The latest trend in the field of cold and ultra-cold physical chemistry is towards control. The magnetic and optical association of atoms is already an example of such control. Exquisite navigation across a maze of avoided crossing states has been demonstrated. Lasers have been used in coherent control of chemical reactions at higher temperatures [253], and the potential for extension to low and ultra-low temperatures is promising. Pulsed chirped lasers have allowed excitation of tailored photoassociated states [148–150]. Two-photon photoassociation, in the so called "pump-dump" scheme, was the first attempt designed to overcome the inefficiencies of spontaneous stabilization. Association of atoms, by coherent Raman scattering [254] that couples ultra-cold scattering states directly to deeply-bound states,

effectively side-stepping intermediated excited state, has played an critical role in realizing dense samples of near degenerate polar molecules [235–238]. Shaped laser pulses have been used to excite tailored wavepackets, and genetic algorithms [255] and control theory [154] have been employed to overcome the complexity of optimizing laser parameters to the characteristics of individual systems. Control of polar molecules up to the hyperfine level has recently been demonstrated [251]. As the production of dense ground state molecules becomes routine, the trend towards control will gain even greater momentum.

Understanding binary collisions and interactions with static fields has been, and will continue to be, central to developments. As we have seen, collision properties determine the feasibility of experiments to cool and manipulate atoms and molecules. These properties show dramatic variation across resonances, and, shape and Feshbach resonances play a critical role in both reactive [73, 75, 78–80, 84] and nonreactive [186, 187, 196, 198, 256] scattering. The density of resonances increases as the colliding partners become heavier, their interaction gets stronger, and the number of channels is increased. Resonances are thus an even more critical feature of physically interesting atomic and molecular systems including the recently achieved ground-state dipolar molecular gases. Dramatic variation of the cross sections, coupled with the possibility of tuning and even inducing resonances using fields [257, 258], point to Feshbach resonances as a promising mechanism of control.

In this thesis we aim to contribute to the understanding of the potential of control of collisions by magnetic Feshbach resonance tuning. We will be interested, in particular, in identifying conditions that result in the strong suppression of the often undesirable inelastic collisions. We propose to do this by locating and characterizing the resonances of the He-O_2 system. This characterization will involve the determination of quantum properties of quasi-bound states, the location of zero-energy resonances, and the analysis of data from low-energy scattering calculations in the presence of a magnetic field. The calculation of bound states is important in

illuminating the underlying pattern that determines the character of quasi-bound responsible for the resonances. Both bound and quasi-bound states are characterized by approximate and rigorously good quantum numbers. In the next two chapters we will discuss the theoretical framework of multichannel bound and scattering states, including methods of numerical calculation. Discussion of the theory will introduce the language and context for understanding the results and important theoretical concepts, including some relating specifically to low-energy scattering. This will be followed by chapter 4, which begins with a discussion of the properties of molecular oxygen as a prerequisite to understanding the pattern of bound states of the He-O_2 complex. The chapter ends with a presentation of the Zeeman structure of bound states of several isotopic combinations of the complex. Only bound states of the same parity as the S-wave dominated low-energy scattering wavefunction are presented. Chapter 5 begins with discussion of low-energy scattering calculations that reinforce earlier theoretical discussion. Calculations of quasi-bound states are presented and the positions in magnetic field of S-wave Feshbach resonances are located. This chapter ends with a discussion of a rather positive finding regrading the prospects of suppressing inelastic collisions by Feshbach resonance tuning.

Chapter 2

Theory of bound states

2.1 Single-channel bound states

2.1.1 Two structureless particles

The wavefunction $\psi(\mathbf{r})$ of two structureless particles interacting according to a time-independent potential $V(r)$, after removing the motion of the center-of-mass motion, satisfies the Schrödinger equation

$$[- \bigtriangledown^2 - k^2 + U(r)]\psi(\mathbf{r}) = 0, \qquad (2.1)$$

with

$$k^2 = \frac{2\mu E}{\hbar^2} \quad \text{and} \quad U(r) = \frac{2\mu V(r)}{\hbar^2}$$

where μ is the reduced mass of the particles and E the energy. This equation is identical to that of a single particle of mass μ in a spherically symmetric potential. It is more illuminating to write equation 2.1 in spherical polar coordinates, which gives

$$\left[-\frac{1}{r^2}\frac{\partial}{\partial r}\left(r^2 \frac{\partial}{\partial r} \right) + \frac{\hat{\mathbf{l}}^2}{r^2} - k^2 + U(r) \right] \psi(\mathbf{r}) = 0. \qquad (2.2)$$

As well as the radial degree of freedom the particles can also orbit about each other. This results in what we will refer to as the end-over-end angular momentum for which $\hat{\mathbf{l}}$ is the operator. We can separate the solutions $\psi(\mathbf{r})$ into angular and radial and write

$$\psi(\mathbf{r}) = r^{-1} \sum_{l=0}^{\infty} \sum_{m=-l}^{l} \chi_l(r) Y_l^m(\hat{\mathbf{r}}). \tag{2.3}$$

The functions $\chi_l(r)$ represents the radial dependence while the angular functions $Y_l^m(\hat{\mathbf{r}})$ are the well known spherical harmonics. They are eigenfunctions of $\hat{\mathbf{l}}^2$ with eigenvalues $l(l+1)$ with $l = 0, 1, 2, 3....$ etc. Substituting equation 2.3 into 2.2 and using orthogonality of the spherical harmonics polynomials gives

$$\left[-\frac{d^2}{dr^2} - k^2 + U(r) + \frac{l(l+1)}{r^2} \right] \chi_l(r) = 0. \tag{2.4}$$

These are a separable set of equations, one for each l. This separability is due to the spherical symmetry of the interaction and means that l, which for structureless particles is also the total angular momentum, is a good quantum number. We can rewrite 2.4 as

$$\left[-\frac{\hbar^2}{2\mu} \frac{d^2}{dr^2} + V_{l,\text{eff}}(r) \right] \chi_l(r) = E\chi_l(r), \tag{2.5}$$

which are a set of single dimensional Schrödinger equations with *effective potential*

$$V_{l,\text{eff}}(r) = V(r) + \frac{\hbar^2 l(l+1)}{2\mu r^2}. \tag{2.6}$$

The effect of the angular degree of freedom is to modify the interaction potential according to the end-over-end angular momentum l. This modification is referred to as the *centrifugal* term in light of its origins. Its notable features are the r^{-2} and inverse mass dependence and the sign. It is repulsive for all r and is smaller for heavier systems. Figure 2.1 depicts an interaction potential of Rb-Cs in a fixed electronic state without the centrifugal term. The features are typical of a pair of interacting atoms. In the extreme short range the interaction potential and the centrifugal terms are both repulsive. For $r = 0$, which corresponds to the particles being at the same point in space, the interaction (and the centrifugal term) is infinitely repulsive. In the short range $V(r)$ dominates over the centrifugal term and the potential is attractive. In the long-range the situation is reversed and the effective potential becomes positive. In an intermediate range where the two terms are comparable there will be a local maximum, the *centrifugal barrier*, at the point where the centrifugal term takes over. The exact position and height of the barrier depends on the reduced mass and details of the interaction potential $V(r)$
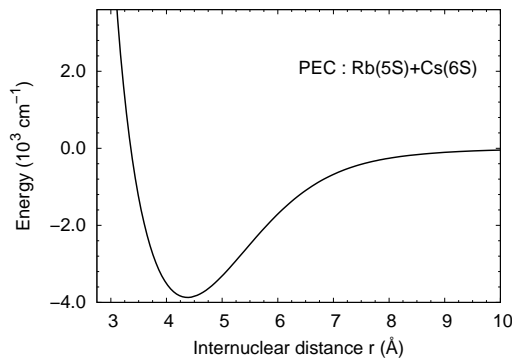
Figure 2.1: The potential energy curve of the electronic ground state, $l = 0$, of RbCs. Produced with permission from data provided by Ghosal [259].

but it gets progressively higher with increasing l. As we shall see in the effects of the *centrifugal barrier* are very important, especially in low energy collisions.

2.1.2 Behavior of the wavefunction in classically *allowed*, and classically *forbidden* regions

Let us now consider the behavior of the radial component of the wavefunction in different regions of the radial domain. Such a consideration will allow us to recall important facts that underpin an understanding of some of the challenges of numerical solution and secondly, but equally importantly, the properties of low-energy radial wavefunctions that will aid an understanding of unique and important phenomena in low energy scattering. Let us begin by considering the behavior in the *classically forbidden* region (so called because a classical particle would not be found there) where $V_{l,\text{eff}}(r) > E$. From equation 2.5 we note that here

$$\text{Sign}[\chi_l''(r)] = \text{Sign}[\chi_l(r)], \tag{2.7}$$

so that $\chi_l(r)$ is convex with respect to the r-axis. We have used $''$ to denote the second derivative with respect to r. Mathematically there are two linearly independent solutions, an exponentially increasing and an exponentially decreasing function of r. For the vast majority of energies the wavefunction is dominated by the increasing component in the limit $r \to \infty$. Starting from either side of the axis $\chi_l(r)$ might approach the axis, constantly turning away, and might miss turning back to grow

unbound. If it crosses the axis it will grow in the opposite direction. Figure 2.2 shows several scenarios for different starting points that might result as the wavefunction approaches the axis.
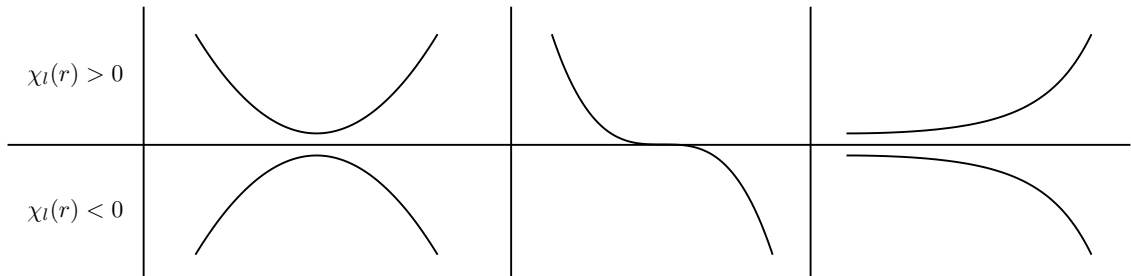
Figure 2.2: Behavior of $\chi_l(r)$ in a *classically forbidden* region for different initial conditions.

In the *classically allowed* region where $V(r) < E$,

$$\text{Sign}[\chi_l''(r)] = -\text{Sign}[\chi_l(r)]. \tag{2.8}$$

The wavefunction is concave with respect to the r-axis and turns towards it. The two independent solutions oscillate about the axis. Beginning from above or below the axis $\chi_l(r)$ will approach it, possibly crossing only to turn back and cross the axis any number of times depending on the energy and the potential. The wavefunction oscillates about the axis.

Bound states are localized states which is usually expressed by the requirement that

$$\lim_{r \to \pm\infty} \chi_l(r) = 0. \tag{2.9}$$

A potential that supports bound states must have at least one classically allowed region sandwiched between two classically forbidden regions. Each forbidden region must either have an infinite range or have a boundary of infinite potential. For two physical particles the condition at minus infinity is imposed instead at $r = 0$ where the potential is infinite. The behavior of the wavefunction coupled with the

bound state conditions means that a bound state must have an energy less that the interaction energy at the *dissociation* limit $r \to \infty$.
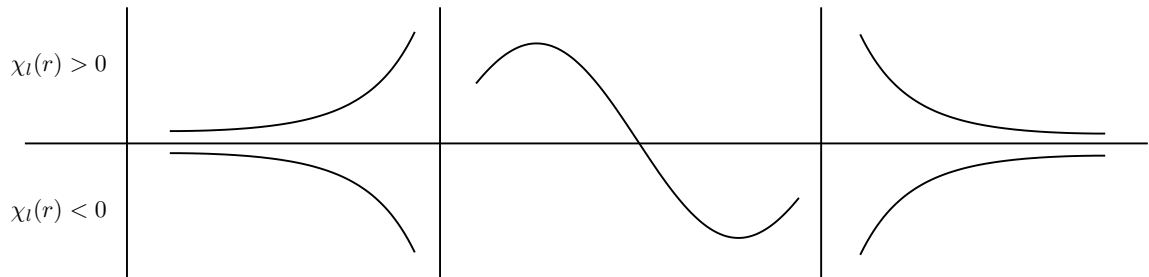
Figure 2.3: The left and right-most panels show bound-state behavior in the *inner* and *outer classically forbidden* regions respectively. The central panel depicts behavior in the *classically allowed* region.

It is possible to build a picture of a bound state from arguments presented so far by combining the behavior in the different regions. Figure 2.3 summarizes the appropriate behavior in the three regions, while figure 2.4 shows the first three levels of Rb-Cs. The potential energy curve is also shown at a scale that corresponds to the eigenvalues of the states in the same figure. As we can see from the figures, the wavefunctions oscillate in the classically allowed region and decay with penetration into the classically forbidden regions on either side. Also the nodes of the wavefunctions begin from zero and increase in steps of one. The square of the wavefunction can be interpreted as a probability distribution of the system. Figure 2.5 depicts the square of four excited states of Rb-Cs belonging to figure 2.1. There are several notable features of individual plots and trends with increasing energy. The probability is pronounced at the two ends nearer the classically forbidden regions. This behavior is consistent with that of a classical particle trapped in a potential which would spend most of its time closer to the turning points where the kinetic energy is lowest. As the energy of the excited state increases the oscillations are more rapid with the probability pushed further away from the central region towards the boundaries. The probability is particularly enhanced around the *outer* turning point. This is due to the shape of the potential and in particular the fact that it
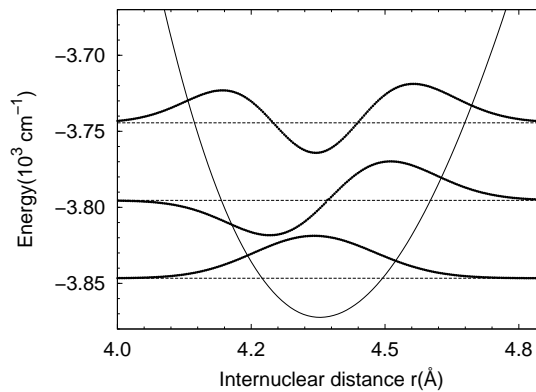
Figure 2.4: The first three states and a zoom-in of the interaction curve. The number of nodes start from zero and go up to two, as expected. RbCs. Produced with permission from data provided by Ghosal [259].

is *less* steep at the *outer* turning point. Typically analytic functions of the interaction between neutral particles obtained by fitting to data have an exponential form nearer the *inner* turning point with an r^{-6} variation in the long-range. Because the potential becomes flatter with increasing r near dissociation functions have very small amplitude in the short-range and are almost entirely long-range in character.

2.1.3   Numerical propagation: some considerations

In all but the simplest cases it is not possible to solve the Schrödinger equation analytically and numerical methods are required. These can be categorized into shooting [260–263] and matrix [264–266] types. Matrix methods use a complete, usually orthonormal, basis set in which to expand the solutions. Of course a practical implementation must truncate the basis set. The eigenvalues are then obtained by diagonalizing the resulting matrix representation of the hamiltonian. An advantage of this method is that all the eigenvalues are obtained at once. However, representing the behavior of the radial wavefunction at the classically forbidden and allowed regions using the same set of basis functions can be challenging and usually results in the need for a large set. Matrix diagonalization time has a cubic dependence on size and this can result in slow convergence. Shooting methods propagate an initial value problem for some trial energy E_{trial} across a range $[r_{\min}, r_{\max}]$ converging on
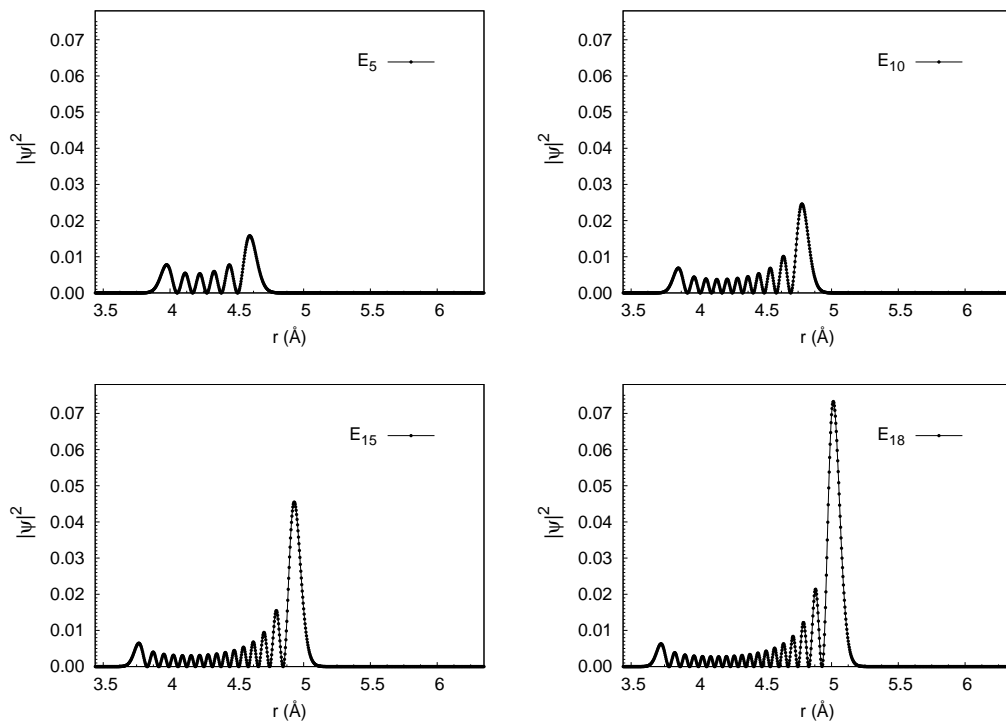
Figure 2.5: The square of the amplitude of the fifth, tenth, fifteenth, and eighteenth excited states of Rb-Cs belonging to the interaction potential shown in figure 2.1. RbCs. Produced with permission from data provided by Ghosal [259].

one eigenvalue at a time. Propagation time is inversely proportional to the number of points. Shooting methods are highly efficient and accurate. The radial part of our system is solved by a shooting method which justifies a restriction of the rest of the discussion in this subsection to integration or shooting methods.

A widely used single-channel propagation algorithm based on the Numerov integration method [267] is that of Cooley [263]. This algorithm propagates a quantity

$$X(r) = \chi_l(r) - h^2 \frac{d^2}{dr^2} \chi_l(r) \tag{2.10}$$

to achieve an error of order $h^6/240$ where h is the integration step size. The initial conditions are expressed by

$$\chi_l(r_{\min}) = 0$$
$$\chi_l'(r_{\min}) = \epsilon,$$

where the initial derivative ϵ is some arbitrarily small non-zero value. In theory, for a two particle potential, $r_{\min}$ should be set to zero and $r_{\max}$ to infinity. In practice they are both set deep enough inside their respective classically forbidden regions as to render the solutions insensitive to their exact values. The propagated solutions will satisfy the *bound-state* boundary conditions at $r_{\max}$ only if E_{trial} coincides with an eigenvalue. As the solution in a classically forbidden region is generally composed of exponentially growing and decaying functions of r any deviation from an eigenvalue will lead, eventually, to domination of the wavefunction by the diverging component. In practice even when the trial energy is very close to an eigenvalue numerical errors eventually lead to divergent behavior.

A common practice to mitigate divergence is to propagate a trial solution outward from $r_{\min}$ and another inward from $r_{\max}$ with appropriate boundary conditions for the same trial energy. The two solutions are then compared for continuity at a point $R_{\text{mid}} \in [R_{\min}, R_{\max}]$ set in the classical region. Due to the linearity of the Schrödinger equation any pair of solutions can be made to agree by scaling. However, continuity of their derivatives required by conservation of momentum affords us a second matching condition. The two matching conditions for a solution can then be summarized by

$$^{\text{l}}\chi'_l / ^{\text{l}}\chi_l |_{r_{\text{mid}}} = {}^{\text{r}}\chi'_l / ^{\text{r}}\chi_l |_{r_{\text{mid}}} \tag{2.11}$$

where superscripts l and r denote propagation from the *left* and *right* directions respectively. In this way we can ensure a single smooth and continuous *bound-state* solution. Numerically there is tolerance for a difference between the two sides of equation 2.11 corresponding to a level of accuracy of the calculated eigenvalue.

When the matching condition is met we have our solution and there is nothing to do. However an initial guess will not, except by coincidence, result in a solution and a procedure to converge to an eigenvalue must be provided. Such a procedure

is a correction formula for E_{trial} based on the difference

$$d(E_{\text{trial}}) = {}^{\text{l}}\chi_l'/{}^{\text{l}}\chi_l|_{r_{\text{mid}}} - {}^{\text{r}}\chi_l'/{}^{\text{r}}\chi_l|_{r_{\text{mid}}}. \tag{2.12}$$

Cooley [263] gave a correction formula that has quadratic convergence in the energy. That such formulae exist is due to the behavior of $d(E_{\text{trial}})$. In particular for small differences $E_{\text{trial}} - E_n$ from an eigenvalue E_n, $d(E_{\text{trial}})$ must be a monotonically increasing or reducing function, crossing the axis $d(E_{\text{trial}}) = 0$ when $E_{\text{trial}} = E_n$. Once in this range a standard root finding algorithm such as the secant [268] method can be used safely to converge to E_n. Properties of one dimensional potentials with minima as described above include the following [269],

1. the spectra of bound states is discrete,

2. bound states are non-degenerate,

3. bound states have a unique number of nodes which increases with the energy.

The last of these properties allows for a systematic sweep through the eigenvalues. The ground state eigenfunction has no nodes, the first exited state has one node, the second has two etc. Normalization, which is a requirement for a physical system, does not affect the position or number of nodes and thus a node count can and is usually used as a first step in a convergence process. When searching for an eigenvalue E_n corresponding to the nth excited state if the node count of the trial solution is greater than n we reduce E_{trial}. If it is lower we increase E_{trial}.

Finally it is worth mentioning that difficulty in propagating the wavefunction in the classically forbidden region stimulated the development of more stable integration algorithms. These algorithms exploit the fact that the instability in the classically forbidden regions is invariably characterized by an explosion in both the wavefunction and its derivative. If one propagates a quantity that is simply related to the ratio of these two quantities it is possible to contain the propagation. Although not generally used in the solution of single-channel problems, one class of method based on propagation of the log-derivative [260] are common in solutions to multi-channel problems.

2.2 Multi-channel bound states

2.2.1 Coupled equations

When dealing with particles that have internal structure but remain chemically relatively distinct, such as van der Waals complexes, it is conceptually and computational helpful to separate *internal* degrees of freedom from those that arise from relative motion. We therefore expand the wavefunction as

$$\Phi(\Omega, \mathbf{R}) = R^{-1} \sum_{\alpha} \chi^{\alpha}(R)\psi_{\alpha}(\Omega) \tag{2.13}$$

where R is the relative separation of the particles and Ω represents all internal degrees of freedom and the end-over-end angular momentum. The use of a capital letter for the separation of the particles is for the purpose of distinguishing the multi-channel from the single-channel case. The $\psi_{\alpha}(\Omega)$ are a complete set for the Hilbert space spanned by the asymptotic Hamiltonian H_{asymp} which for a pair of particles 1 and 2 is

$$H_{\text{asymp}} = H_1 + H_2 \tag{2.14}$$

where H_i is the monomer Hamiltonian of i. If the functions are eigenfunctions of H_{asymp} then they correspond to unique combination of monomer states and are referred to as channels. Channels can be constructed simply as products of the monomer eigenfunctions and will thus generally include rotational, vibrational, spin and possibly electronic wavefunctions of the individual particles. The $\chi^{\alpha}(R)$ are radial *channel functions*. The factor R^{-1} is included for convenience of form in the final expressions. The Hamiltonian of the complex excluding the center-of-mass motion, can be written as

$$H = -\frac{\hbar^2}{2\mu} R^{-1} \frac{d^2}{dR^2} R + V(\mathbf{R}, \Omega) + H_{\text{asymp.}} \tag{2.15}$$

The term $V(\mathbf{R}, \Omega)$ includes centrifugal contributions as well as the interaction potential energy and depends on the internal states and the vector $\mathbf{R}$. Dependence on the orientation of $\mathbf{R}$ expresses the interaction anisotropy. Substituting 2.13 into the

Schrödinger equation

$$H\Phi(\Omega, \mathbf{R}) = E\Phi(\Omega, \mathbf{R}) \tag{2.16}$$

with H given by 2.15 and projecting onto a channel $\psi_\beta(\Omega)$, assuming an orthonormal set ψ_α, yields

$$\frac{d^2\chi^\alpha(R)}{dR^2} = \sum_\beta [W_{\alpha,\beta}(R) - E\delta_{\alpha,\beta}]\chi^\beta(R) \tag{2.17}$$

where

$$W_{\alpha\beta}(R) = \frac{2\mu}{\hbar^2} \int \psi_\beta(\Omega)^* \left[V(R,\Omega) + H_{\mathrm{asymp}}\right] \psi_\alpha(\Omega)d\Omega. \tag{2.18}$$

Equation 2.17 can be expressed in matrix form simply as

$$\chi(R)'' = \mathrm{W}(R)\chi(R). \tag{2.19}$$

For an N channel problem $\mathrm{W}(R)$ is an N by N dimensional matrix and $\chi(R)$ are N by 1 column vectors.

2.2.2 Early numerical methods

Numerical solution of coupled equations is computationally intensive. Early attempts to solve the coupled equations had to make drastic approximations which were aimed mainly at decoupling the equations. The most drastic of these, the *distorted wave* approximation [270], simply ignored the off-diagonal terms of $W(R)$. From equation 2.18 we can see that the diagonal components $W(R)_{\alpha\alpha}$ act to distort the *channel functions* which explains the name of the approximation technique. In scattering, these diagonal terms contribute to elastic scattering. Adiabatic methods [270, 271] attempt to include some of the coupling by diagonalizing $W(R)$ at each point R to obtain *adiabats*. These *adiabats* act as effective potential energy curves for the radial motion described by a set of decoupled equations. The most important approximation for van der Waals molecules is *helicity decoupling* [272,273] which neglects terms off-diagonal in the total angular momentum projection onto the intermolecular axis. This effectively block diagonalizes the coupled equations resulting in bound states which can be labeled by the intermolecular axis projection quantum number. In all approximate methods the neglected contributions could be

included by perturbation methods. In the modern era of desktop computers, how-
ever, we can afford to use *close-coupling* methods which solve the coupled equations
exactly with the exception in practice of basis set truncation.

As in the single-channel case methods for the solution of the coupled equations
2.19 can be broadly classified as matrix [274–276] or grid [264] methods. Matrix
methods expand all degrees of freedom in a basis set while grid methods, as the
name suggests, propagates all variables across a grid. The *coupled channel* [277–279]
method is a particularly efficient hybrid which integrates the radial component by
quadrature and handles internal dimensions using a basis set. This avoids simul-
taneous representation problems of the wavefunction in the classically allowed and
forbidden regions discussed for the one dimensional case. It also reduces the dimen-
sion of the matrix which must be diagonalized significantly reducing solution time.
The remainder of this chapter, which is devoted to the *coupled channel* method, will
look first at two important implications of the presence of more than one channel
on locating eigenvalues; the specification of correct initial conditions and the sys-
tematic determination of bound states. We will follow this by a description of the
multi-channel log-derivative [280] method which we have employed in our study.

2.2.3   Coupled channel method

Converging on an eigenvalue

In the single-channel case the numerical solution for eigenvalues was reduced to a
search in a single parameter, the energy. This was possible because the linearity
of the Schrödinger allowed us, by renormalization, to eliminate the search for the
correct initial derivative. In an N dimensional multi-channel case, the bound-state
boundary conditions specify the solutions at initial points and thus propagation of
a trial solution requires the specification of $N + 1$ parameters, N for the initial
derivatives of the radial *channel* functions $\chi^\alpha(R)$ that make up our vector solution
$\chi(R)$ and a trial energy. Renormalization can reduce the number of parameters
by one which would still leave us with N parameters to specify. Early numerical

methods [281–283] devised elaborate techniques to converge on the correct initial derivatives and energy. Gordon [277] was the first to suggest a method that avoids the need for the correct derivatives. The method takes advantage of the linearity of the Schrödinger equation which means that a linear combination of solutions that have the same energy is itself a solution at the same energy.

For a trial energy E_{trial} Gordon propagates a set of solutions with zero initial values and an arbitrary but linearly independent set of initial derivatives. With precisely N such solutions we span the space of all solutions that satisfy the desired initial conditions for a bound state. Therefore, as long as linear independence is maintained, any solution $\psi(R)$ that is zero at the initial point and has an energy E_{trial}, including an eigenfunction if it exists, can be expressed as a linear combination of the propagated solutions. We write this as

$$^{\text{l}}\Psi(R)C^{\text{l}} = \psi(R), \tag{2.20}$$

where $^{\text{l}}\Psi(R)$ is an $N \times N$ matrix whose columns are the propagated solutions and C^{l} is a set of coefficients. Equation 2.20 holds for arbitrary R and the coefficients are independent of R. The superscript l indicates outward propagation from the left boundary point R_{min}. Propagating inward from R_{max} at the other end of our range at the same trial energy in a similar manner gives a second equation

$$^{\text{r}}\Psi(R)C^{\text{r}} = \psi(R) \tag{2.21}$$

for solutions $\psi(R)$ that meet the bound-state boundary condition at the trial energy. If an eigenfunction $\phi(R)$ exists at the trial energy it must belong to the common space spanned by the columns of $^{\text{l}}\Psi(R)$ and $^{\text{r}}\Psi(R)$. This means there exists a pair of column coefficients C^{l} and C^{r} such that

$$^{\text{l}}\Psi(R)C^{\text{l}} = \phi(R) = \psi(R)C^{\text{r}} \tag{2.22}$$

so that

$$^{\text{l}}\Psi(R_{\text{mid}})C^{\text{l}} = {}^{\text{r}}\Psi(R_{\text{mid}})C^{\text{r}} \tag{2.23}$$

for any matching point R_{mid}. Continuity imposes the second condition

$$^{\mathrm{l}}\Psi'(R)C^{\mathrm{l}} = {}^{\mathrm{r}}\Psi'(R)C^{\mathrm{r}} \tag{2.24}$$

where $'$ indicates a derivative with respect to R. Gordon combines the two conditions 2.23 and 2.24 into a single set of $2N$ linear homogeneous equations

$$\begin{pmatrix} ^{\mathrm{l}}\Psi(R_{\mathrm{mid}}) & {}^{\mathrm{r}}\Psi(R_{\mathrm{mid}}) \\ ^{\mathrm{l}}\Psi'(R_{\mathrm{mid}}) & {}^{\mathrm{r}}\Psi'(R_{\mathrm{mid}}) \end{pmatrix} \begin{pmatrix} C^{\mathrm{l}} \\ C^{\mathrm{r}} \end{pmatrix} = \underline{\mathbf{0}}. \tag{2.25}$$

For a nontrivial set of coefficients, which we postulate, equation 2.25 implies that the determinant

$$\begin{vmatrix} ^{\mathrm{l}}\Psi'(R_{\mathrm{mid}}) & {}^{\mathrm{r}}\Psi'(R_{\mathrm{mid}}) \\ ^{\mathrm{l}}\Psi(R_{\mathrm{mid}}) & {}^{\mathrm{r}}\Psi(R_{\mathrm{mid}}) \end{vmatrix} = 0. \tag{2.26}$$

This condition is not only a necessary but also a sufficient one for E_{trial} to coincide with an eigenvalue and then holds for any choice of matching point R_{mid}. As the determinant of a matrix is a scalar quantity we can use a standard one dimensional root finding algorithm to search for eigenvalues. This reduces the number of search parameters to one, the energy.

At energies away from eigenvalues the determinant in equation 2.26 is a function of R_{mid} and a judicious choice can crucially affect the search for eigenvalues. Johnson [260, 278] and Manolopoulos [284] have discussed strategies for choosing R_{mid}. Note that the coefficients C^{l} and C^{r} do not appear in equation 2.26 and therefore it is not necessary to calculate the eigenfunctions in order to determining the eigenvalues. If required the coefficients can be calculated but only after locating the eigenvalues.

A generalized node count

Armed with a strategy for locating eigenvalues that depends on a reasonable assumption of continuity of the determinant in the neighborhood of an eigenvalue, we are left with a need for a strategy to determine that neighborhood. In the single-channel case the node count provided such a strategy. The simple characterization

of the wavefunction as positive or negative, which allows the detection of nodes, does not apply to a vector wavefunction and the changes caused by changing the propagation parameters is not transparent. This means that a simple extension of the single-channel node count is not possible. Gordon's solution [277], based on the observation that the number of zeros of the determinant $|\Psi(R)|$ along the whole integration range is equal to the number of eigenvalues below the corresponding energy E_{trial}, is described below.

Let us consider an imaginary problem similar to our real problem but with an infinite potential wall placed at the boundary R_{o}. When $R_{\text{o}} = R_{\text{max}}$ the eigenvalues of the real system coincide with those of the imaginary problem. We must of course choose R_{min} and R_{max} to qualify this assumption. Let us now consider what happens to eigenvalues below some trial energy E_{trial} as we move R_{o} towards R_{min}. The eigenvalues of our imaginary problem are monotonically reducing functions of the separation $R_{\text{o}} - R_{\text{min}}$. In the limit of zero separation even the *ground state* eigenvalue tends to infinity. So as we reduce R_{o} the eigenvalues increase smoothly (adiabatically), each coinciding with E_{trial} at some value of R_{o}. For each such R_{o} there must be an eigenfunction $\phi_n(R)$ and therefore a set of nontrivial coefficients C such that

$$\Psi(R)C = \phi_n(R) \tag{2.27}$$

for $R \in [R_{\text{min}}, R_{\text{o}}]$. As a bound state eigenfunction to our imaginary problem $\phi_n(R)$ satisfies

$$\phi_n(R_{\text{o}}) = \underline{\mathbf{0}} \tag{2.28}$$

and by implication of equation 2.27

$$|\Psi(R_{\text{o}})| = 0. \tag{2.29}$$

This happens exactly once for each eigenvalue that was initially below E_{trial}.

We have established that $|\Psi(R)|$, at E_{trial}, has a zero for each eigenvalue of the

physical problem below E_{trial}. What remains to be shown is that each zero of the $|\Psi(R)|$ corresponds to an eigenvalue of the real problem. First we note that each such zero would imply the existence of a nontrivial set of coefficients C for which

$$\Psi(R_{\text{o}})C = \underline{0} \tag{2.30}$$

at E_{trial}. The product $\Psi(R)C$ defines a function which by virtue of 2.30 is an eigenfunction of the imaginary problem. If we now increase the separation of the walls from R_{o} the eigenvalue will monotonically decrease. At $R_{\text{o}} = R_{\text{max}}$ the eigenvalue must coincide with one of the eigenvalues of our real problem. Thus a zero of the determinant of $\Psi(R)$ propagated at the energy E_{trial} corresponds to an eigenvalue of our real problem below E_{trial}. This completes the arguments of a one-to-one correspondence between the zeros of $|\Psi(R)|$ and the number of eigenvalues of our real problem below the trial energy E_{trial}. For a more formal discussion of this subject see Calvert and Davidson [285].

The chief development in Gordon's method is the elimination of the need to converge on the correct set of initial derivatives. This is achieved at the price of propagating an $N \times N$ matrix of trial solutions in place of an iterative process involving a single $N \times 1$ trial solution. The computational effort of Gordon's methods scales as the cube of the number of channels. Despite this, it has proven advantageous.

The problem presented by propagating through a classically forbidden region in the single-channel case is worse in multi-channel problems. The range of R for which at least one of the channels is forbidden is greater. For converged results it is always necessary to include some closed channels which exacerbates the problem. The unbound growth of the closed channels means they quickly dominate the trial solutions leading to a loss of linear independence. In principle, propagating independent solutions from the two boundary points should mitigate the problem as in the single-channel case but in practice this is not the case and the problem is quite

serious. Gordon applied regular stabilizing transformations during propagation designed to recover linearity. A more satisfactory solution proposed by Johnson [280] involves the propagating the multi-channel log-derivative.

2.2.4   Log derivative and log derivative propagator

The log-derivative $Y(R)$ of the matrix $\Psi(R)$ is defined as

$$Y(R) = \Psi'(R)\Psi^{-1}(R). \tag{2.31}$$

$\Psi^{-1}(R)$ is the inverse of $\Psi(R)$. Propagating the log-derivative is quite stable even in the presence of closed channels. This makes it the method of choice for many multi-channel calculations. The essential reason for this stability can be understood by considering a single-channel example. Let us assume a one dimensional square well potential. The Schrödinger equation can be written as

$$\frac{d^2\psi(R)}{dR^2} = k^2\psi(R). \tag{2.32}$$

The log-derivative $y(R)$ for the one dimensional case is

$$y(R) = \frac{1}{\psi(R)}\frac{d\psi(R)}{dR}. \tag{2.33}$$

Differentiating equation 2.33 and using 2.32 to replace the second derivative gives

$$y(R)' + y^2(R) - k^2 = 0. \tag{2.34}$$

This is a Ricatti equation and for constant k^2 has solutions

$$y(R) = \begin{cases} |k|\coth(|k|R), & \text{if } k^2 \geq 0 \\[2mm] |k|\cot(|k|R), & \text{if } k^2 \leq 0 \end{cases} \tag{2.35}$$

Apart from states very close to dissociation, for which $|k| \approx 0$, the log-derivative in the classically forbidden region remains finite (as $\lim_{R\to\infty} |k|\cot(|k|R) = |k|$). In the multi-channel case the relative sizes of closed and open channel elements of the trial solutions remain finite resulting in the preservation of linearity of the trial set.

The solutions 2.34 have poles in the classically forbidden regions. These poles correspond to the roots of the wavefunction $\psi(R)$. This problem persists in the multi-channel case where $\Psi^{-1}(R)$ and hence $Y(R)$ becomes undefined when $|\Psi(R)| = 0$. As we have seen this condition not only occurs but is the basis of our generalized node count. It is not possible to propagate across singularities using standard numerical integration techniques and invariant imbedding methods are used instead.

Johnson [280] was the first to give a propagation formula for the multi-channel log-derivative based on invariant imbedding but it was Mrugala and Secrest [286] who first published a derivation. They formulated propagation equations for coupled channels with a first derivative term which arises naturally in curve-crossing or reactive scattering problems. The equations of non-reactive multi-channel scattering is a special case obtained by setting the coefficient of the first derivative term to zero. Following Manolopoulos [284], who has given a formulation that closely follows Mrugala and Secrest, we will outline the method for the non-reactive case.

We begin by defining the log-derivative propagator as a map

$$y(a,b) : \{\Psi(a), \Psi(b)\} \longrightarrow \{\Psi'(a), \Psi'(b)\} \tag{2.36}$$

by

$$
\begin{pmatrix} \Psi'(a) \\ \Psi'(b) \end{pmatrix} = \begin{pmatrix} y_1(a,b) & y_2(a,b) \\ y_3(a,b) & y_4(a,b) \end{pmatrix} \begin{pmatrix} -\Psi(a) \\ \Psi(b) \end{pmatrix} \tag{2.37}
$$

where

$$
y(a,b) = \begin{pmatrix} y_1(a,b) & y_2(a,b) \\ y_3(a,b) & y_4(a,b) \end{pmatrix} \tag{2.38}
$$

and $a, b \in [R_{\min}, R_{\max}]$. The log-derivative relates the values of a function at two points to its derivatives at the same points. For an $N \times N$ trial matrix $\Psi(R)$ the individual $y_i(a,b)$ are each $N \times N$ matrices making $y(a,b)$ $2N \times 2N$. The log-derivative is closely related to the $R-$matrix of Light and Walker [287], another common propagator used in atomic and molecular bound and scattering state calculations.

Propagation across an interval $[a, b]$, where $a < b$, involves construction of a propagator $y(a, b)$ from a series of consecutive propagators of smaller intervals. Let us begin by dividing the interval $[a, b]$ in two by introducing a point $c = (b - a)/2$. We seek to determine $y(a, b)$ in terms of the half sector propagators $y(a, c)$ and $y(c, b)$. Expanding the defining equation 2.37 for the half sectors $[a, c]$ and $[c, b]$ a little algebraic manipulation and comparison with the propagator equations of $y(a, b)$ gives

$$
\begin{aligned}
y_1(a, b) &= y_1(a, c) - y_2(a, c)Z(a, b, c)y_3(a, c) \\[4pt]
y_2(a, b) &= y_2(a, c)Z(a, b, c)y_2(c, b) \\[4pt]
y_3(a, b) &= y_3(c, b)Z(a, b, c)y_3(a, c) \\[4pt]
y_4(a, b) &= y_4(c, b) - y_3(c, b)Z(a, b, c)y_2(c, b)
\end{aligned}
\tag{2.39}
$$

Where

$$
Z(a, b, c) = [y_4(a, c) + y_1(c, b)]^{-1}.
\tag{2.40}
$$

We now proceed to make an important connection between the log-derivative *propagator* and the log-derivative *matrix*. We start with the equation

$$
\begin{pmatrix} \Psi'(0) \\ \Psi'(R) \end{pmatrix} = \begin{pmatrix} y_1(0, R) & y_2(0, R) \\ y_3(0, R) & y_4(0, R) \end{pmatrix} \begin{pmatrix} -\Psi(0) \\ \Psi(R) \end{pmatrix}
\tag{2.41}
$$

for the log-derivative propagator across an interval $[0, R]$, and impose the boundary condition $\Psi(0) = \underline{0}$ appropriate for bound states. This gives

$$
\Psi'(0) = y_2(0, R)\Psi(R) \quad \text{and} \quad \Psi'(R) = y_4(0, R)\Psi(R).
\tag{2.42}
$$

Rearranging the second equation and comparing with equation 2.31 yields

$$
Y(R) = y_4(0, R).
\tag{2.43}
$$

Combining this with the last of equation 2.39 gives

$$
Y(b) = y_4(c, b) - y_3(c, b)[Y(c) + y_1(c, b)]^{-1}.
\tag{2.44}
$$

This is the recursion relation used to propagate the log-derivative matrix across a sector $[a, b]$. It expresses $Y(b)$ in terms of $Y(c)$ and the half sector propagators.

The propagation procedure can be summarized by

1. Partition the range of integration

2. Construct numerical approximations to $y(a, b)$ across each sector using equations 2.39

3. Propagate the log-derivative matrix across the range using equation 2.44

The substantial missing ingredient for propagation is the sectoral numerical approximation to $y(a, b)$. We begin by expressing equation 2.19 in terms of the matrix $\Psi(R)$ of trial solutions

$$\Psi''(R) = W(R)\Psi(R). \tag{2.45}$$

This can be recast as

$$\Psi''(R) - W^0(R)\Psi(R) = W^1(R)\Psi(R) \tag{2.46}$$

by expanding $W(R)$ us a sum of a diagonal component $W^0(R)$ and a term $W^1(R)$ that contains all off-diagonal contributions. We refer to $W^0(R)$ as the reference potential and to $W^1(R)$ as the residual. The residual components might include diagonal components. The idea is to represent the reference potential analytically so that the diagonal, and thus decoupled, homogeneous counterpart to equation 2.46

$$\Psi''(R) - W^0(R)\Psi(R) = \underline{0} \tag{2.47}$$

has two linearly independent solutions satisfying an appropriate set of boundary conditions denoted by $\Phi_\pm(R)$. The particular solutions $\Psi_\pm(R)$ to equation 2.46 with the same boundary conditions are then given by

$$\Psi_\pm(R) = \Phi_\pm(R) + \int G(R, R')W^1(R')\Psi_\pm(R)dR'. \tag{2.48}$$

Where the Green's function $G(R, R')$ is given by

$$G(R, R') = \Phi_-(R<)\Omega^{-1}\Phi_+(R>). \tag{2.49}$$

The $R <$ and $R >$ indicate the lesser and greater, respectively, of R and R'. The Wronskian Ω is

$$\Omega = \Phi_-(R').$$ (2.50)

It is well known that the Wronskian of two linearly independent functions is independent of the variable associated with the functions and so we are free to evaluate it at any point. We now impose the condition

$$\begin{pmatrix} \Phi_+(a) & \Phi_-(a) \\ \Phi_+(b) & \Phi_-(b) \end{pmatrix} = \begin{pmatrix} -I & 0 \\ 0 & I \end{pmatrix}$$ (2.51)

at the boundaries of the sector $[a, b]$. These conditions are also satisfied by $\Phi_\pm(R)$ which allows us to evaluate Ω as

$$\Omega = \Phi'_-(a) = \Phi'_+(b).$$ (2.52)

The conditions 2.51 together with the defining equation 2.37 give

$$\begin{pmatrix} y_1(a, b) & y_2(a, b) \\ y_3(a, b) & y_4(a, b) \end{pmatrix} = \begin{pmatrix} \Psi'_+(a) & \Psi'_-(a) \\ \Psi'_+(b) & \Psi'_-(b) \end{pmatrix}.$$ (2.53)

Evaluating $G(R, R')$ using 2.52, substituting into 2.48 and differentiating gives

$$y_1(a, b) = y_1^0(a, b) + \int_a^b \Phi_+(R')W^1(R')\Psi_+(R')dR'$$

$$y_2(a, b) = y_2^0(a, b) + \int_a^b \Phi_+(R')W^1(R')\Psi_-(R')dR'$$

$$y_3(a, b) = y_3^0(a, b) + \int_a^b \Phi_-(R')W^1(R')\Psi_+(R')dR'$$

$$y_4(a, b) = y_4^0(a, b) + \int_a^b \Phi_-(R')W^1(R')\Psi_-(R')dR'$$ (2.54)

where

$$\begin{pmatrix} y_1^0(a, b) & y_2^0(a, b) \\ y_3^0(a, b) & y_4^0(a, b) \end{pmatrix} = \begin{pmatrix} \Phi'_+(a) & \Phi'_-(a) \\ \Phi'_+(b) & \Phi'_-(b) \end{pmatrix}.$$ (2.55)

The functions $\Phi_\pm(R)$ are assumed to be known and thus a numerical approximation to the $y_i(a,b)$ can be obtained by representing the integral by quadrature. At first sight the appearance of the undetermined solutions $\Psi_\pm(R)$ under the integral signs in 2.54 appears to present a problem. In practice, this has the effect of restricting us to a quadrature that evaluates the integrand at the boundaries where $\Psi_\pm(R)$ are prescribed by the boundary conditions. The trapezium rule is an obvious choice. It fits a straight line between the boundary points in effect approximating the integrand to a linear function. We can do better with Simpson's rule which approximates the integrand to a quadratic equation. Simpson's rule requires evaluation of the integrand at the midpoint. There in no problem in evaluating the residual potential at any point but the solutions are not known at the midpoint. However, we use the equations of the half-sector propagators 2.39 to remove the need for this evaluation. Modification to the ordinary Simpson's rule is required to account for a discontinuity in the first derivative of $G(R, R')$.

The final numerical approximations to the half-sector propagators are [284]

$$y_1(a, c) = y_1^0(a, c) + \frac{h}{3} W^1(a)$$

$$y_2(a, c) = y_2^0(a, c)$$

$$y_3(a, c) = y_3^0(a, c)$$

$$y_4(a, c) = y_4^0(a, c) + \frac{2h}{3} \tilde{W}(c)^1 \tag{2.56}$$

for the first half and

$$y_1(c, b) = y_1^0(c, b) + \frac{2h}{3} \tilde{W}(c)^1$$

$$y_2(c, b) = y_2^0(c, b)$$

$$y_3(c, b) = y_3^0(c, b)$$

$$y_4(c, b) = y_4^0(c, b) + \frac{h}{3} W(b)^1 \tag{2.57}$$

for the second half-sector. The quantity h is the step size and

$$\tilde{W}(c)^1 = \frac{6}{h^2}\left[I - \frac{h^2}{6}W^1(c)\right]^{-1} - \frac{6}{h^2}I. \tag{2.58}$$

We are finally left with the choice of reference potential and the representation (basis set) in balancing the accuracy and computational cost. Johnson's algorithm [280] corresponds to choosing a diagonal reference potential whose components are the collision energy. This corresponds to trigonometric and hyperbolic solutions (for the open and closed channels, respectively) for the homogeneous solutions. The whole potential must then be treated by quadrature. In principle, any level of accuracy could be obtained in this way as long as we set the step size h to be small enough. However, treating part of the potential analytically gives better convergence with h. Manolopoulos' first improvement, referred to as the *diabatic* modified log-derivative propagator [288], involved the use of a piecewise constant reference potential

$$W^0(R)_{ij} = W(c)\delta_{ij}, \tag{2.59}$$

for $R \in [a, b]$. The half-sector propagators are then diagonal and given by

$$y_1^0(a,c) = y_4^0(a,c) = y_1^0(c,b) = y_4^0(c,b) = \begin{cases} |k_j|\coth(|k_j|h) & k_j^2 \geq 0 \\ |k_j|\cot(|k_j|h) & k_j^2 \leq 0 \end{cases} \tag{2.60}$$

and

$$y_2^0(a,c) = y_3^0(a,c) = y_2^0(c,b) = y_3^0(c,b) = \begin{cases} |k_j|\operatorname{csch}(|k_j|h) & k_j^2 \geq 0 \\ |k_j|\csc(|k_j|h) & k_j^2 \leq 0 \end{cases} \tag{2.61}$$

where $k_j^2 = W(c)_{jj} - E$.

The choice of reference potential made by Manolopoulos means that $W^1(c)$ is independent of energy. Thus, once calculated, these matrices can be saved for use at subsequent energies. This leads to a reduction of matrix inversion operation from 3 to 2 for each subsequent propagation across a sector. These two advantages result

in a significant reduction in computational effort for a given accuracy. With finite computing resources this translates to an improvement in achievable accuracies.

The benefits of analytic treatment of a diagonal reference potential might be inadequate for systems that are strongly off-diagonal in the chosen representation. We are of course free to choose any representation. For strongly off-diagonal systems Manolopoulos' *quasi-adiabatic modified* propagator [284] transforms the potential matrix to a representation that leaves the residual potential identically zero at the midpoint c. This eliminates the need to evaluate $\tilde{W}(c)^1$ which also becomes zero but we must find the diagonalizing basis at c. However, because a change in energy changes only the diagonal component of $W(R)$ the transformation matrices need only be calculated once and stored for use at subsequent energies. Transformation between the basis set corresponding to each sector involves two matrix multiplications and must be performed at each energy. In effect the *quasi-adiabatic* modified propagator is computationally more demanding and its use must be balanced with the advantages it offers over the *diabatic* modified propagator.

As in Gordon's method, the log-derivative methods propagate a set of N linearly independent solutions from each end of the propagation range. Because the log-derivative obeys the Ricatti equation, a first order equation, it only requires a single boundary condition. This is conveniently imposed at the origin and translates to

$$Y(0) = \infty I. \tag{2.62}$$

In practice this is replaced by a matrix with very large diagonal elements, say

$$Y(0) = 10^{30} I. \tag{2.63}$$

There is also no need to propagate the derivative of the log-derivative for the same reasons that reduce the number of boundary conditions. We therefore propagate a single $N \times N$ matrix. The matching condition of the *left* and *right* propagated log-derivatives

$$[\ ^{\text{l}}Y(R_{\text{mid}}) - {}^{\text{r}}Y(R_{\text{mid}})\ ]\Psi(R_{\text{mid}}) = \underline{0} \tag{2.64}$$

is particularly simple. Johnson [278] determined the eigenvalues by finding the roots of the determinant $|\ ^{\text{l}}Y(R_{\text{mid}}) - {}^{\text{r}}Y(R_{\text{mid}})\ |$.

We can write an eigenvalue equation

$$Y_{\text{match}}\Psi(R_{\text{mid}}) = \lambda\Psi(R_{\text{mid}}) \tag{2.65}$$

where $Y_{\text{match}} = {}^{\text{l}}Y(R_{\text{mid}}) - {}^{\text{l}}Y(R_{\text{mid}})$ and λ represents the eigenvalues. The matching condition 2.64 corresponds to a zero eigenvalue equation. The λ are functions of the trial energy E_{trial} with roots corresponding to eigenvalue E_n.

Hutson [279] studied the behavior of the determinant and eigenvalues of Y_{match} for total angular momentum $J = 1$ of the ground vibrational states of Ar-HF. The calculations were done for R_{mid} values 3.2 Å, 3.3 Å and 3.4 Å. The results showed that the roots of the determinant $|Y_{\text{match}}|$ coincide with those of the eigenvalues λ. These are the energies E_n of the physical problem. The E_n are unchanged by the value of R_{mid}, nonetheless, at other values E_{trial} both the determinant and λ can be affected strongly. Crucially the determinant function is not monotonic and can be adversely affected by the choice of R_{mid}. For some choices it is possible for the determinant function to approach the axis, touch it at an eigenvalue E_n and turn back without crossing the axis. This presents a problem for standard root finding numerical algorithms. Luckily, the λ are monotonic functions of energy and methods for locating E_n based on searching for the roots of these functions have proven to be much more robust.

Chapter 3

Scattering theory

3.1 Single-channel scattering

3.1.1 Introduction

We begin our discussion of scattering by considering the collision of two structureless particles. As was the case for bound states, this simplification offers sufficient context for the introduction of important scattering concepts that survive the complexity of coupled channels. In particular we can introduce the powerful method of *partial waves*. We have seen in the bound states chapter that the Schrödinger equation of two interacting structureless particles is essentially equivalent to the interaction of a single particle with a central potential. We can therefore equivalently imagine the scattering of a pair of such particles as a perturbation of the path of a single particle by a potential $V(r)$. The steady state solution ψ can be considered to be a sum

$$\psi = \psi_{\text{in}} + \psi_{\text{sc}} \tag{3.1}$$

of an incoming, ψ_{in}, and scattered, ψ_{sc}, component. The incoming wave travels in a definite direction defining a preferred axis. This reduces the symmetry from spherical to cylindrical which means the solution ψ can be expanded as

$$\psi(\mathbf{r}) = r^{-1} \sum_{l=0}^{\infty} \chi_l(r) P_l(\cos\theta) \tag{3.2}$$

where θ is the angle between the incoming and scattering directions without loss of generality. The functions $P_l(\cos\theta)$ are Legendre polynomials.

Experimentally all measurements are made at distances so large compared to the range of interaction that it is sufficient for the theoretic treatment to consider the effects of scattering only in the asymptotic region. In this region ψ_{in} can be represented by a plane-wave while ψ_{sc} travels in all directions with and probability density governed by the inverse square law (i.e. $|\psi_{\text{sc}}|^2 \propto r^{-2}$). The scattered wave will also generally depend on θ. Noting that the magnitude of the incoming and outgoing wave vectors is the same and the angle between them, θ, we can summarize the requirements mathematically by

$$\psi_{\text{in}} = \exp(ikr\cos\theta) \qquad \text{and} \qquad \psi_{\text{sc}} = \frac{f(\theta)}{r}\exp(ikr). \tag{3.3}$$

In the asymptotic region we therefore have

$$\psi(r,\theta) \sim \exp(ikr\cos\theta) + \frac{f(\theta)}{r}\exp(ikr). \tag{3.4}$$

Where we have written $\psi(\mathbf{r})$ as $\psi(r,\theta)$ making the variables explicit. The functions $f(\theta)$ is the *scattering amplitude* and represents the angular dependence of the scattered wave. The scattering amplitude, as we will see, contains all the physically relevant information. The scattering problem is essentially solved when the wavefunction is determined in the asymptotic region allowing the extraction of the scattering amplitude $f(\theta)$ by comparison with equation 3.4.

3.1.2 Cross sections and the scattering amplitude

The quantity that is measured experimentally is the cross section. The *differential* cross section is defined as the ratio of scattered to incoming flux. The scattered flux travels radially outward and measures the number of particles per unit time per unit solid angle. The flux $\mathbf{j}$ associated with a wavefunction ψ is given by

$$\mathbf{j} = \frac{\hbar}{\mu}\text{Im}[\psi^* \bigtriangledown \psi] \tag{3.5}$$

where μ is the reduced mass. Using equations 3.3 we get

$$\mathbf{j}_{\text{in}} = \frac{\hbar}{\mu}k\hat{\mathbf{r}} \qquad \text{and} \qquad \mathbf{j}_{\text{sc}} = \frac{\hbar}{\mu}\frac{|f(\theta)|^2}{r^2}k\hat{\mathbf{r}} \tag{3.6}$$

for the incident and scattered flux respectively. Thus the *differential* cross section $(d\sigma/d\Omega)$ related to the incoming and outgoing flux by

$$\frac{d\sigma}{d\Omega} = r^2 \frac{|\mathbf{j}_{\text{sc}}|}{|\mathbf{j}_{\text{in}}|}, \tag{3.7}$$

where *Omega* is the solid angle, is given by

$$\frac{d\sigma}{d\Omega} = |f(\theta)|^2. \tag{3.8}$$

The total *integral* cross section σ_{tot} obtained by integration over all directions is given by

$$\sigma_{\text{tot}} = \int |f(\theta)|^2 d\Omega. \tag{3.9}$$

3.1.3 Partial wave analysis

We have seen that solving the scattering problem amounts to a determination of the wavefunction of our system in the asymptotic region. Let us begin by recalling the Schrödinger equation for two unstructured particles 2.4

$$\left[-\frac{d^2}{dr^2} - k^2 + U(r) + \frac{l(l+1)}{r^2} \right] \chi_l(r) = 0. \tag{3.10}$$

In the absence of a potential equation 3.10 reduces to

$$\left[-\frac{d^2}{dr^2} - k^2 + \frac{l(l+1)}{r^2} \right] \chi_l^0(r) = 0. \tag{3.11}$$

Where the superscript 0 in the solutions is added to emphasis the absence of the potential. Two independent solutions are $kr j_l(kr)$ and $kr n_l(kr)$. The functions $j_l(kr)$ and $n_l(kr)$ are the well known spherical Bessel and spherical Neumann functions respectively. The most general solution is then expressible as a linear combination of these independent solutions. However, on physical grounds, we require the solution to be regular everywhere. Imposing this requirement at the origin eliminates the spherical Neumann solutions leaving us with the solutions

$$\chi_l^0(r) = A_l^0(k) kr j_l(kr). \tag{3.12}$$

In general we must allow the factor A_0 to depend on the scattering energy or equivalently on k. If we now assume that our potential falls off faster than r^{-2} we note

that in an intermediate region where the contribution of the potential can be ignored but the centrifugal term is still significant equation 3.10 reduces in form to 3.11 with solutions $\chi_l(kr)$ approximated by

$$\chi_l(r) = kr[A_l(k)j_l(kr) + B_l(k)n_l(kr)]. \tag{3.13}$$

Regularity at the origin still applies but we cannot impose it on equation 3.13 which is applied some distance away from the origin. We are now in a position to consider the effect of introducing the potential on the asymptotic form of the wavefunction. As $kr \to \infty$

$$j_l(kr) \longrightarrow \frac{1}{kr} \sin(kr - \pi l/2) \tag{3.14}$$

and

$$n_l(kr) \longrightarrow -\frac{1}{kr} \cos(kr - \pi l/2). \tag{3.15}$$

This implies that in the asymptotic region we have

$$\chi_l^0(r) \approx A_l^0(k) \sin(kr - \pi l/2) \tag{3.16}$$

and

$$\chi_l(kr) \approx [A_l(k) \sin(kr - \pi l/2) - B_l(k) \cos(kr - \pi l/2)] \tag{3.17}$$

which can be written as

$$\chi_l(kr) \approx C_l(k) \sin(kr - \pi l/2 + \delta_l(k)) \tag{3.18}$$

where $C_l(k) = [A_l(k)^2 + B_l(k)^2]^{1/2}$ and

$$\delta_l(k) = -\arctan(B_l(k)/A_l(k)) \tag{3.19}$$

is a phase shift. With the understanding that the phase-shift is a function of k we omit the explicit expression in most expressions. The presence of the potential therefore allows us to retain the term $n_l(kr)$ which in the asymptotically region results in a shift in phase of the wavefunction. We can write 3.17 as

$$\chi_l(kr) \approx \sin(kr - \pi l/2) - K_l(k) \cos(kr - \pi l/2)], \tag{3.20}$$

where

$$K_l(k) = \tan(\delta_l) \tag{3.21}$$

defines the diagonal elements of the K-matrix. The non-diagonal elements are zero. Similarly, we can express equation 3.18 as

$$\chi_l(kr) \sim e^{-i(kr-\pi l/2)} - S_l(k)e^{i(kr-\pi l/2)} \tag{3.22}$$

where

$$S_l(k) = e^{2i\delta_l(k)} \tag{3.23}$$

defines the S matrix. The S and K matrices are related by

$$S_l(k) = \frac{1 + iK_l(k)}{1 - iK_l(k)}. \tag{3.24}$$

The sign of a phase shift

The effect of the potential on the sign of the phase-shift is best illustrated by comparing two potentials $U(r)$ and $\bar{U}(r)$. The relevant equations for the two potentials are

$$\left[-\frac{d^2}{dr^2} + k^2 + U(r) + \frac{l(l+1)}{r^2}\right]\chi_l(r) = 0 \tag{3.25}$$

and

$$\left[-\frac{d^2}{dr^2} + k^2 + \bar{U}(r) + \frac{l(l+1)}{r^2}\right]\bar{\chi}_l(r) = 0. \tag{3.26}$$

Multiplying 3.25 by $\bar{\chi}_l(r)$ and 3.26 by $\chi_l(r)$ and integrating the difference gives

$$[\bar{\chi}_l(r)\chi'_l(r) - \bar{\chi}'_l(r)\chi_l(r)]|_0^\infty = \int_0^\infty \bar{\chi}_l(r)\chi_l(r)[\bar{U}(r) - U(r)]\,dr \tag{3.27}$$

where the dash denotes derivative with respect to r. Recalling that $\bar{\chi}_l(0) = \chi_l(0) = 0$ and selecting the asymptotic form

$$\chi_l(r) \approx \sin(kr - \pi l/2) + \tan(\delta_l)\cos(kr - \pi l/2) \tag{3.28}$$

for $\chi_l(r)$ and similarly for $\bar{\chi}_l(r)$ gives, after a little algebraic manipulation,

$$k[\tan(\bar{\delta}_l) - \tan(\delta_l)] = \int_0^\infty \bar{\chi}_l(r)\chi_l(r)[\bar{U}(r) - U(r)]\,dr. \tag{3.29}$$

If we now consider the two potentials to be infinitesimally close so that

$$\bar{U}(r) - U(r) = \varepsilon, \tag{3.30}$$

a small positive number, and consequently

$$\bar{\chi}_l(r) \approx \chi_l(r). \tag{3.31}$$

Then the integrand on the right hand side of equation 3.29 becomes $\chi_l(r)^2 \varepsilon$, and is positive everywhere. Thus we have

$$\tan(\bar{\delta}_l) > \tan(\delta_l) \iff \bar{\delta}_l > \delta_l. \tag{3.32}$$

Thus an overall more repulsive potential $\bar{U}(r)$ results in a greater phase-shift $\bar{\delta}_l(k)$. If we adopt a convention that a zero phase-shift corresponds to a zero potential then,

$$\delta_l > 0 \iff \text{overall repulsive potential} \tag{3.33}$$

and

$$\delta_l < 0 \iff \text{overall attractive potential.} \tag{3.34}$$

Cross sections

We now return to the question of determining the cross sections. The idea is to first determine the scattering amplitude and then using equation 3.9 to calculate the cross section. The first step is to expand the first term in equation 3.4 representing the incoming flux in Legendre polynomials. We note that

$$\exp(ikr\cos\theta) = \sum_{l=0}^{\infty}(2l+1)i^l j_l(kr)P_l(\cos\theta). \tag{3.35}$$

Expressing the asymptotic form of $j_l(kr)$ given by equation 3.14 in terms of complex exponentials and substituting into 3.35 we can express 3.4 as a sum of *radially* incoming and outgoing parts

$$
\begin{aligned}
\psi(r,\theta) \quad \sim \quad & \left[-\frac{1}{2ik}\sum_{l=0}^{\infty}(2l+1)i^l\exp(il\pi/2)P_l(\cos\theta)\right]\frac{\exp(-ikr)}{r} \\
+ \quad & \left[\frac{1}{2ik}\sum_{l=0}^{\infty}(2l+1)P_l(\cos\theta)i^l\exp(-il\pi/2)+f(\theta)\right]\frac{\exp(ikr)}{r}.
\end{aligned}
\tag{3.36}
$$

Next we rewrite equation 3.18 as

$$\chi_l(kr) \longrightarrow \frac{C_l(k)[\exp(i(kr - \pi l/2 + \delta_l)) - \exp(-i(kr - \pi l/2 + \delta_l))]}{2ikr} \tag{3.37}$$

and substitute this into 3.2 to obtain

$$\psi(r,\theta) \longrightarrow \sum_{l=0}^{\infty} \frac{C_l(k)[\exp(i(kr - \pi l/2 + \delta_l)) - \exp(-i(kr - \pi l/2 + \delta_l))]}{2ikr} P_l(\cos\theta)$$

$$\tag{3.38}$$

for the asymptotic form of the partial wave expansion. We now compare coefficients of the linearly independent functions $\exp(ikr)$ and $\exp(-ikr)$ of equations 3.38 and 3.36. Comparison of the coefficients of $\exp(-ikr)$ gives

$$\sum_{l=0}^{\infty}[(2l+1)i^l - C_l(k)\exp(-i\delta_l)]P_l(\cos\theta)\exp(il\pi/2) \;=\; 0$$

which upon setting the individual l terms to zero gives

$$C_l(k) = (2l+1)i^l \exp(i\delta_l). \tag{3.39}$$

Similarly comparison of $\exp(ikr)$ yields

$$
\begin{aligned}
f(\theta) &= \frac{i}{2k}\sum_{l=0}^{\infty}(2l+1)i^l P_l(\cos\theta)\exp(-il\pi/2)[\exp(2i\delta_l) - 1] \\
&= \frac{i}{2k}\sum_{l=0}^{\infty}(2l+1)i^l P_l(\cos\theta)\exp(-il\pi/2)[S_l(k)) - 1]
\end{aligned}
$$

for the scattering amplitude. Substituting this expression into equation 3.9, using 3.39 and noting the orthogonality of the $P_l(\cos\theta)$ we have

$$\sigma_{tot} = \frac{4\pi}{k^2}\sum_{l=0}^{\infty}(2l+1)|1 - S_l(k)|^2. \tag{3.40}$$

We note that the total cross section can be written as a sum of contributions σ_l from each of the partial waves where

$$\sigma_l = \frac{4\pi}{k^2}(2l+1)|1 - S_l(k)|^2. \tag{3.41}$$

Note also that the total cross section is dependent only on the phase-shifts. Thus, essentially the phase-shifts contain all the measurable information. In order to evaluate the cross sections we must first obtain phase-shifts. Conceptually, we divide the total radial coordinate range in two, the interior region in which the potential is effective and equation 3.10 applies, and the exterior region in which the potential is negligible where equation 3.11 applies. We have seen that the external region has analytic solutions and using equation 3.13 and 3.19, the general form of the total radial component of the wavefunction $R_l(r, k) = \chi_l(kr)/r$ can be written

$$R_l(r) = D_l(k)[j_l(kr) - \tan(\delta_l)n_l(kr)]. \tag{3.42}$$

In the interior region, the solution is solved numerically and the phase-shift is then obtained by imposing continuity of the solution and its derivative at the boundary of these two regions. Equivalently, we can require that the log-derivative be continuous. If we denote the log-derivative of the interior region by $\gamma_l(k)$ and let $r = b$ at the boundary then

$$\gamma_l(k) = \frac{j_l'(kb) - \tan(\delta_l)n_l'(kb)}{j_l(kb) - \tan(\delta_l)n_l(kb)}. \tag{3.43}$$

The prime denotes a derivative with respect to kr. We can rearrange this to get

$$\tan(\delta_l) = \frac{\gamma_l(kb)j_l(kb) - kj_l'(kb)}{\gamma_l(k)n_l(kb) - kn_l'(kb)} \tag{3.44}$$

from which we can obtain the phase-shift up to an additive multiple of π.

Low-energy scattering

In the asymptotic region we have seen that the scattering wavefunction has the form of a sine wave. The left panel of figure 3.1 shows a low-energy scattering wavefunction of Rb-Cs on the ground state PEC. In continuation of the trend of highly excited states discussed earlier and shown in figure 2.5, low-energy scattering states oscillate rapidly in the short range in contrast to the behavior at long range. The amplitude of the wavefunction in the long range is much bigger. This means that the probability of finding the particles in close proximity to each other is very
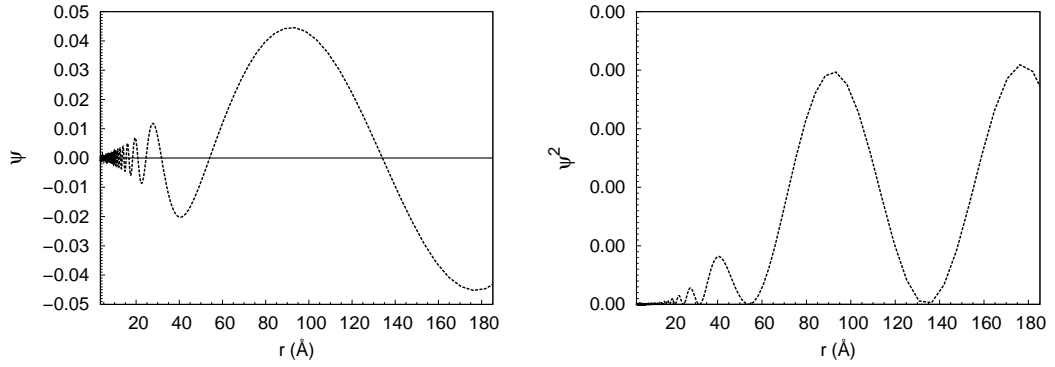
Figure 3.1: The wavefunction and its square of a low energy scattering state of RbCs on the ground state interaction energy (P.E.S shown in figure 2.1).

small and vanishes rapidly with reducing collision energy as is evident also from the square of the wavefunction shown on the right-hand panel. In general the scattering properties are determined mainly by the long-ranged details of the interaction. In this low-energy limit, defined by $kb \rightarrow 0$, we note that

$$j_l(kb) \longrightarrow \frac{(kb)^l}{(2l+1)!} \tag{3.45}$$

and

$$n_l(kb) \longrightarrow -\frac{(2l+1)!}{(kb)^{l+1}} \tag{3.46}$$

where ! denotes factorial. Substitution into equation 3.44 yields

$$\tan(\delta_l) \approx \frac{\hat{\gamma}_l \frac{(kb)^l}{(2l+1)!} - kl\frac{(kb)^{l-1}}{(2l+1)!}}{\hat{\gamma}_l \frac{(2l+1)!}{(kb)^{l+1}} - k(l+1)\frac{(2l+1)!}{(kb)^{l+2}}}. \tag{3.47}$$

Where $\hat{\gamma}_l = \lim_{kb \rightarrow 0} \gamma_l(kb)$

$$\tan(\delta_l) \approx \frac{(kb)^{2l+1}(\hat{\gamma}_l b - l)}{[(2l+1)!]^2(\hat{\gamma}_l b + l + 1)} \tag{3.48}$$

Thus, as long as $\hat{\gamma}_l b \neq -(l+1)$, which would result in a singularity,

$$\tan(\delta_l) \propto k^{2l+1}. \tag{3.49}$$

Restricting the range of the phase-shift to $-\pi \leq \delta_l \leq \pi$ and using $\tan(\delta_l) \approx \sin(\delta_l)$ for $\delta_l \approx 0$ and equations 3.41 and 3.49 we conclude

$$\sigma_l \approx 4\pi(2l+1)k^{4l}. \tag{3.50}$$

So for vanishingly small energies the low energy cross sections vanish for all but the $l = 0$ partial wave, also referred to as the S partial-wave. The S partial-wave contribution tends to a constant value.

Scattering length

The scattering length $a_l(k)$ is defined by

$$a_l(k) = \lim_{k \to 0} \frac{\tan(\delta_l)}{k}. \tag{3.51}$$

It is a truly low energy concept. From 3.49 we see that

$$a_l(k) \sim k^{2l}. \tag{3.52}$$

By arguments similar to those of low-energy cross sections the scattering lengths is also dominated by the S partial-wave in the low energy regime. Using 3.50 and 3.52

$$\sigma_l(k) \approx 4\pi(2l+1)a_0^2(k). \tag{3.53}$$

The scattering length is used to characterizes low-energies scattering and determines properties of low *ultra-low* temperature gases including the chemical potential [289] and the stability in traps [4,5]. We can develop an instructive intuitive understanding of the scattering length by considering low energy scattering by a *hard* ball potential of radius $\bar{r}_0$. The potential is infinite for $r < \bar{r}_0$ and zero for $r > \bar{r}_0$. An incoming sine wave is totally reflected upon contact with the potential and can be expressed as

$$\phi(r) \sim \sin(k[r - \bar{r}_0]). \tag{3.54}$$

The scattered wave has a phase-shift $\delta_0 = k\bar{r}_0$. If we recall that at low energy $a_0 \approx \delta_0/k$ we have $a_0 \approx \bar{r}_0$. This suggests that in order to reproduce collision properties of a real system by a model contact potential the radius $\bar{r}_0$ of the model potential must be equal to the scattering length of the real system.

Resonances

The phase-shift generally changes slowly with energy, however at times it will change rapidly and as it crosses some multiple of $\pi/2$ produces peaks in the cross sections. The scattering length will have a pole precisely when $\delta_l = \pi(n+1/2)$, with n a natural number, which corresponds to the pole in the $\tan(\delta_l)$ function. This phenomenon is referred to as a resonance and happens when the scattering state crosses the energy of a *quasi-bound* state. If we expand $\cot(\delta_l)$ as a function of energy about the energy E_{res} corresponding to the pole in the scattering length we get

$$
\begin{aligned}
\cot(\delta_l(E)) &= \cot(\delta_l(E_{\mathrm{res}})) + (E - E_{\mathrm{res}}) \left(\tfrac{d\cot(\delta_l(E))}{dE} \right)_{E=E_{\mathrm{res}}} + o(E - E_{\mathrm{res}})^2 \\
&\approx -(E - E_{\mathrm{res}}) \left(\tfrac{1}{\sin^2(\delta_l(E))} \tfrac{d\delta_l(E)}{dE} \right)_{E=E_{\mathrm{res}}} + o(E - E_{\mathrm{res}})^2.
\end{aligned}
\tag{3.55}
$$

Noting that $\sin(\delta_l(E_{\mathrm{res}})) \approx 1$ and defining Γ by

$$
\frac{1}{2} \left(\frac{d\delta_l(E)}{dE} \right)_{E=E_{\mathrm{res}}} = \frac{1}{\Gamma}
\tag{3.56}
$$

we have

$$
\cot(\delta(E)) \approx (E - E_{\mathrm{res}}) \frac{2}{\Gamma}.
\tag{3.57}
$$

The quantity Γ has units of energy and is referred to as the *width* of the resonance. Thus near a resonance, substituting $1/[\cot^2(\delta_l(E)) + 1]$ for $\sin^2(\delta_l(E))$ in equation 3.41, we can express the partial wave cross section as

$$
\begin{aligned}
\sigma_l(E) &= \tfrac{4\pi}{k^2}(2l+1)\tfrac{1}{\cot^2(\delta_l)+1} \\
&= \tfrac{4\pi}{k^2}(2l+1)\tfrac{\Gamma^2}{4(E-E_{\mathrm{res}})^2+\Gamma^2}.
\end{aligned}
\tag{3.58}
$$

This final form is the well known Breit-Wigner form.

Inelastic scattering

As a prelude to our discussion of multi-channel scattering we consider inelastic scattering from the viewpoint of loss of flux from an incoming channel. We start by expressing the asymptotic solution 3.36 as

$$\Phi(\mathbf{r}, \theta) = F_{\text{in}}(k, \theta)\frac{\exp(-ikr)}{r}\hat{\mathbf{r}} + F_{\text{out}}(k, \theta)\frac{\exp(ikr)}{r}\hat{\mathbf{r}}. \tag{3.59}$$

The coefficients of $\exp(-ikr)/r$ and $\exp(ikr)/r$ have been captured in $F_{\text{in}}(k, \theta)$ and $F_{\text{out}}(k, \theta)$, respectively. The outgoing flux through a point $\mathbf{J}_{\text{out}}(r, \theta)$ is given by

$$\mathbf{J}_{\text{out}} = \frac{|F_{\text{out}}(k, \theta)|^2}{r^2}k\hat{\mathbf{r}} + O(r^{-3}).$$

To obtain the total outgoing flux, I_{out}, we must integrate $\mathbf{J}_{\text{out}}$ over a closed surface containing the scatterer. We conveniently choose the surface of a sphere centered at the scatterer so that

$$
\begin{aligned}
I_{\text{out}} &= \oiint_{\mathbf{S}} \mathbf{J}_{\text{out}} \cdot \mathbf{ds} \\
&= \oiint_{\mathbf{S}} [|F_{\text{out}}(k, \theta)_{\text{out}}|^2 k + O(r^{-1})]d\Omega.
\end{aligned}
$$

If we let the surface be arbitrarily large, which we are at liberty to do, the contribution of the terms $O(r^{-1})$ can be neglected and we end up with

$$
\begin{aligned}
I_{\text{out}} &= \oiint_{\mathbf{S}} |F_{\text{out}}(k, \theta)|^2 k d\Omega \\
&= \frac{\pi}{k}\sum_{l=0}^{\infty}(2l + 1)|S_l(k)|^2.
\end{aligned}
$$

Similarly the total incoming radial flux is

$$
\begin{aligned}
I_{\text{in}} &= \oiint_{\mathbf{S}} |F_{\text{in}}(k, \theta)|^2 k d\Omega \\
&= \frac{\pi}{k}\sum_{l=0}^{\infty}(2l + 1).
\end{aligned}
$$

The total inelastic cross section $\sigma^{\text{tot,inel}}(k)$ is given by

$$\sigma^{\text{tot,inel}}(k) = -\frac{I_{\text{in}} - I_{\text{out}}}{I_{\text{in}}}.$$

The minus sign is there because we are expressing a loss in flux. This gives

$$\sigma^{\text{tot,inel}}(k) = \frac{\pi}{k^2}\sum_{l=0}^{\infty}(2l + 1)[1 - |S_l(k)|^2].$$

3.2 Multi-channel scattering

For collisions between structured particles it is necessary to consider transitions between internal states before and after the encounter. Such transitions generally allow for an exchange of energy between the internal states and the relative motion. Multi-channel scattering methods are formulations that account for this additional structure. If we consider collisions between two structured particles, 1 and 2, with internal states ϕ_n^1 and ϕ_m^2 given by

$$H_1\phi_n^1 = E_n\phi_n^1$$
$$H_2\phi_m^2 = E_m\phi_n^2,$$

then a unique combination of internal states $\phi_k^1\phi_l^2$ constitutes a *channel*. The equations of motion are identical to those of the multi-channel *bound states* . The difference as in the single-channel case is in the boundary conditions which we describe below.

3.2.1 Boundary conditions and cross sections

The conditions at $R = 0$ remain the same but the second condition is applied in the asymptotic region where the interaction is negligible. For an incoming channel α the asymptotic form of the wavefunction is

$$\chi_{\alpha,\alpha}(R) \sim \exp(ik_\alpha z) + f_{\alpha,\alpha}(\theta,\phi)\frac{\exp(ik_\alpha R)}{R}. \tag{3.60}$$

On all outgoing channels β we do not have an incoming component so that the asymptotic form of the wavefunction is

$$\chi_{\alpha,\beta}(R) \sim f_{\alpha,\beta}(\theta,\phi)\frac{\exp(ik_\beta R)}{R}. \tag{3.61}$$

We can summarize this by

$$\chi_{\alpha,\beta}(R) \sim \exp(ik_\beta z)\delta_{\alpha,\beta} + f_{\alpha,\beta}(\theta,\phi)\frac{\exp(ik_\beta R)}{R}. \tag{3.62}$$

The $f_{\alpha\beta}(\theta,\phi)$ are the probability amplitudes associated with the transitions from α to β and $\delta_{\alpha,\beta}$ is the kronecker-delta. The number of particles, dN_β, scattered

through a solid angle $d\Omega$ at R per unit time is

$$dN_\beta = v_\beta |f_{\alpha,\beta}(\theta,\phi)|^2 d\Omega. \tag{3.63}$$

The square of the probability amplitude gives the probability density but this must be multiplied by the asymptotic velocity of the channel to obtain the outgoing flux. As the incoming wavefunction is of unit intensity the flux is v_α. Noting that $v_\alpha = k_\alpha \hbar / 2\mu$ and similarly for v_β the differential cross section associated with the transition is

$$\frac{d\sigma_{\alpha,\beta}}{d\Omega} = \frac{k_\alpha}{k_\beta} |f_{\alpha,\beta}(\theta,\phi)|^2 d\Omega. \tag{3.64}$$

The integral cross section is then

$$\sigma_{\alpha,\beta} = \frac{k_\alpha}{k_\beta} \int_\Omega |f_{\alpha,\beta}(\theta,\phi)|^2 d\Omega. \tag{3.65}$$

The boundary condition can be written in terms of the S-matrix as

$$
\begin{aligned}
\chi_{\alpha L, \beta L'}(R) \quad \sim \quad & \exp(-i[k_\alpha R - L\pi/2])\delta_{\alpha,\beta}\delta_{L,L'} \\
& - \left(\frac{k_\alpha}{k_\beta}\right)^{1/2} S_{\alpha L, \beta L'} \exp(i[k_\beta R - L'\pi/2]),
\end{aligned}
$$

where the partial-wave dependence of the channels has been made explicit so that the previous channel labels, α, β, etc. now do not include the partial wave label L. We have used a capital letter L to distinguish the current discussion from the single-channel case. These boundary conditions apply to the channel functions. In general it is of course not necessary to use the eigenfunctions of the asymptotic hamiltonian for the basis set so that the it would be necessary to diagonalize for the true channels before applying the boundary conditions.

The elastic and inelastic cross sections can be expressed in terms of the S-matrix as

$$\sigma_{\alpha,\beta} = \frac{4\pi}{k_\alpha} \sum_J \sum_L \sum_{L'} |\delta_{L,L'}\delta_{\alpha,\beta} - S^J_{\alpha L, \beta L'}|^2. \tag{3.66}$$

3.2.2 Multi-channel S-matrix

We now outline how to evaluate the S-matrix from the propagated solutions. We begin by expressing the form of the channel functions in the asymptotic region. The open channels have the form of the spherical Bessel functions

$$[J(R)]_{\beta,\alpha} = \delta_{\beta,\alpha} k_\alpha^{-1/2} \hat{j}(k_\alpha R) \tag{3.67}$$

$$[N(R)]_{\beta,\alpha} = \delta_{\beta,\alpha} k_\alpha^{-1/2} \hat{n}(k_\alpha R). \tag{3.68}$$

The closed channel functions

$$[J(R)]_{\beta,\alpha} = \delta_{\beta,\alpha} (k_\alpha^{1/2} R) I_{L+1/2}(k_\alpha R) \tag{3.69}$$

$$[N(R)]_{\beta,\alpha} = \delta_{\beta,\alpha} (k_\alpha^{1/2} R) I_{L+1/2}(k_\alpha R) \tag{3.70}$$

are modified spherical Bessel functions. The multi-channel wavefunction $\Psi(R)$ in the asymptotic region can the be expressed as

$$\Psi(R) = J(R) + N(R)K \tag{3.71}$$

where K is the reaction matrix which connects the channels. It can be written as

$$K = \begin{pmatrix} K_{\text{oo}} & K_{\text{oc}} \\ K_{\text{co}} & K_{\text{cc}} \end{pmatrix}. \tag{3.72}$$

where K_{oo}, K_{oc}, K_{co} and K_{cc} are the open-open, open-closed, closed-open and closed-closed sub-matrices. In terms of the log-derivative the K-matrix is given by

$$K = -[Y(R)N(R) - N'(R)]^{-1} \times [Y(R)J(R) - J'(R)]. \tag{3.73}$$

Finally, the S-matrix can be calculated from the open-open sub-matrix K_{oo} by

$$S = (I + iK_{\text{oo}})^{-1}(I - iK_{\text{oo}}). \tag{3.74}$$

Note the similarity with the equation 3.24.

3.2.3 Rate constants

Cross sections $\sigma_{\alpha,\beta}$ give transition probabilities following a collision and do not contain information on the likelihood of collisions. The collision rate is proportional to the velocity so that we can define a rate coefficient $K_{\alpha,\beta}$ for a flux of particles of velocity v as $v\sigma_{\alpha,\beta}$. Real experiments involve thermal samples characterized by a distribution of velocities. The thermally averaged rate coefficient $< K_{\alpha,\beta} >$ is given by

$$< K_{\alpha,\beta} >= \int_0^\infty v\sigma_{\alpha,\beta}g(v,T)\,dv. \tag{3.75}$$

The $g(v,T)$ is a velocity distribution function which depends on the temperature T. In the classical limit the distribution is typically Maxwellian, at very low temperatures where quantum effects become important the distribution is governed by Bose-Einstein or Fermi-Dirac statistics depending on whether the particles are fermions or bosons. The $< K_{\alpha,\beta} >$ gives the overall transition rate for a sample at given temperature which is often of more direct value in an experiment than the cross sections.

Chapter 4

Bound states of He-O$_2$

4.1   Introduction

The decision to study He-O$_2$ was motivated by several reasons. In its ground state molecular oxygen is a $^3\Sigma$ molecule. This combines the simplest electronic state with a Zeeman structure necessary to tune zero-energy resonances which is a central requirement of our study. The paramagnetic nature also means that O$_2$ is suitable for magnetic trapping. Because of its closed-shell nature He introduces the least number of terms to the Hamiltonian of the total system making the complex a relatively simple one to study. Helium is the most common buffer gas and has also been used as a carrier gas in the supersonic expansion of O$_2$ [290, 291]. The availability of good *ab initio* potential energy surfaces [292, 293] was also an important factor in our choice of system.

We are ultimately interested in studying the collision dynamics in a magnetic field and in particular the behavior across Fesbach resonances at ultra-low collision energies. As we shall see, locating resonances requires calculation of *bound* and *quasi-bound* or *resonance* states of the complex. The range of energy and field that must be considered is determined by the need to locate zero-energy resonances and to characterize the bound states in order to understand their interaction with scattering states. In this chapter we present calculations of the bound states of the He-O$_2$ van der Waals complex.

Factoring out the translational motion of the center-of-mass, we can express the Hamiltonian $\hat{H}_\text{c}$ of the complex in Jacobi coordinates (depicted in figure 4.8 on page 95) as

$$\hat{H}_\text{c} = -\frac{\hbar^2}{2\mu}\nabla^2_{\mathbf{R}} + \hat{H}_\text{mon} + V(R, r, \Theta), \tag{4.1}$$

where $\mathbf{r}$ is the vector connecting the two oxygen atoms, $\mathbf{R}$ the separation of the centers of mass of O$_2$ and the He atom and Θ the angle between $\mathbf{r}$ and $\mathbf{R}$. The reduced mass of the complex is μ, and $\hat{H}_\text{mon}$ denotes the O$_2$ monomer Hamiltonian. The $V(R, r, \Theta)$ is the interaction potential of O$_2$ with He. We assume He to have no internal structure and it thus makes no separate contributions to $\hat{H}_\text{c}$. As we shall see later, this assumption also means that the channels are defined by the internal structure of molecular oxygen and the end-over-end angular momentum. An understanding of the field-free and Zeeman structures of O$_2$ is indispensable for a clear understanding of the energy level structure of He-O$_2$.

In the following sections we proceed by first examining $\hat{H}_\text{mon}$ to determine the structure of O$_2$. We follow this with a discussion outlining the method used in calculating the interaction potential $V(R, r, \Theta)$ and features of the He-O$_2$ PES of Groenenboom and Struniewicz [292] which we have used in our *bound* and *scattering* states calculations. The results of bound state calculations are presenting at the end.

4.2 Properties of O$_2$

The structure of any molecule is determined by the limitation imposed by the various interactions on the spacial and spin degrees of freedom of the constituent particles, the electrons and nuclei. As we shall see in the next section, the nuclear and the electronic degrees of freedom are approximately separable, however, the nuclear framework imposes strong restrictions on electronic spacial degrees of freedom and determines the spacial symmetry and therefore the classification of the electronic structure. Unlike atoms, molecules are not spherically symmetric and so the total electronic orbital angular momentum is not a good quantum number, but all diatomic molecules have an axis of rotational symmetry along the bond of the two
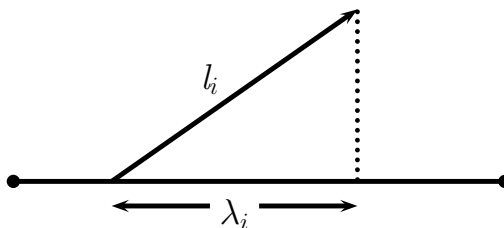
Figure 4.1: The projection, λ_i, of the orbital angular momentum l_i is a good quantum number used in the classification of diatomic molecular orbitals.
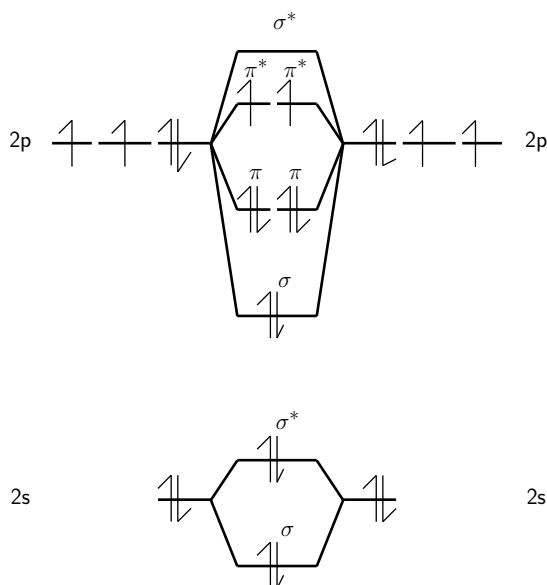

Figure 4.2: A simple molecular orbital diagram for O$_2$.

nuclei. The projection, λ_i, of the orbital angular momentum on the intermolecular axis is therefore a good quantum number and forms a basis for classifying electronic structure states. In analogy to atomic orbitals molecular orbitals are labeled σ,π,δ, *etc.* depending on whether $\lambda_i = 0, 1, 2$, *etc.* The total projection, Λ, is the sum of the individual projections of occupied states. The total symmetry of the electronic-structure is said to be Σ, Δ, Π, *etc.* according to the value of Λ. Oxygen has atomic number 8 with electronic configuration 1s^{2}2s^{2}2p^4. Figure 4.2 is a simple molecular orbital diagram showing the construction of the electronic structure of molecular oxygen from two atoms. Only the valence electrons are shown. Two unpaired electrons of O$_2$ contribute to the angular momentum. They occupy two degenerate π orbitals to minimize repulsion energy and have parallel spins in accordance with Hund's rule. This results in an overall spin 1 state which makes the ground state

a triplet. The two π orbitals have opposite angular momentum projection on the intermolecular axis giving a total projection of zero. The electronic states are subject to a reflection symmetry about a plane containing the two atoms. The two highest π orbitals have +1 and -1 symmetry with respect to this reflection. The resulting symmetry of the ground state is $-1 \times +1 = -1$. Finally, homonuclear diatomic molecules have a center of inversion and thus the wavefunction must be an eigenfunction of the parity operator. The electronic ground state of O$_2$ is of even parity. In summary, the ground state is an overall *gerade* triplet sigma state or $^3\Sigma_g^-$ in short. The g stands for gerade which is German for even in description of the parity. The superscript on the right-hand side signifies the symmetry with respect to reflection discussed above. In general, the contribution of the electrons to the total wavefunction of O$_2$ can be expanded in terms of products of electronic spin and electronic structure basis functions. However, the energy required to excite the electronic structure are many orders of magnitude larger than is available at ultra-low temperatures, therefore, the electronic structure is confined to the ground state and is often omitted in expressions of the basis functions.

The electronic structure solved for different nuclear configurations defines a potential surface which determines the rotational and vibrational structure of the nuclear framework. Due to the high energies involved in vibrational excitations they are inaccessible at ultra-low energy collisions which allows us to suppress vibrational motion. We thus restrict our calculations to the electronic and vibrational ground states $(^3\Sigma_g^-, v = 0)$. Nuclei will also posses spin and an associated magnetic moment, however, magnetic moments are inversely proportional to the mass which makes nuclear magnetic moments three orders of magnitude smaller than electronic magnetic moments. For this reason the energy contributions of nuclear spin are ignored. As we shall see however, the nuclear spin has a profound impact on the rotational energy structure which we must account for. The complete form of an element of the basis set for O$_2$ would include the electronic-structure, vibrational, rotational and electronic and nuclear spin functions. As the electronic-structure and vibrational motion are restricted to their respective ground states, and nuclear spin

is neglected, elements of the basis set can be written simply as

$$|sm_s\rangle|nm_n\rangle \tag{4.1}$$

where $|sm_s\rangle$ and $|nm_n\rangle$ are basis functions of the electronic spin and nuclear rotation angular momentum, respectively. Following González-Martínez and Hutson [294], we adopt the convention that monomer quantum numbers are represented by small letters while capital letters are used for quantum numbers of the complex. The spin $s = 1$, which means $-1 \leq m_s \leq 1$. Alternatively $|sm_s\rangle$ and $|nm_n\rangle$ can be coupled to give $|nsjm_j\rangle$ according to

$$|nsjm_j\rangle = \sum_{n,s} c(n, m_n, j, m_j)|nm_n\rangle|sm_s\rangle \tag{4.2}$$

with $c(n, m_\mathrm{n}, j, m_j)$ the Clebsh-Gordon coupling coefficients and $m_j = m_n + m_s$. The $|nsjm_j\rangle$ would then be elements of a coupled basis set.

In the absence of a field, the O$_2$ Hamiltonian is

$$
\begin{aligned}
\hat{H}_\mathrm{mon} &= -\frac{\hbar^2}{2\mu_\mathrm{mon}}\nabla_r^2 + V(r) + \hat{H}_\mathrm{ss} + \hat{H}_\mathrm{sn} \\
&= -\frac{\hbar^2}{2\mu_\mathrm{mon}}\frac{1}{r}\frac{\partial^2}{\partial r^2}r + \frac{\hat{n}^2}{2\mu_\mathrm{mon}r^2} + V(r) + \hat{H}_\mathrm{ss} + \hat{H}_\mathrm{sn}.
\end{aligned}
\tag{4.3}
$$

The first two terms are kinetic energy terms, with the first a vibrational term and the second a rotational term. The operator $\hat{n}^2$ is an angular momentum operator associated with the rotation of the diatomic. The last two terms are the spin-spin and the spin-rotation interactions respectively. The potential $V(r)$ incorporates all other interactions between the constituent particles. The ground-state vibrational wavefunction of the monomer, $\nu_0(r)$, is an eigenfunction of

$$-\frac{\hbar^2}{2\mu_\mathrm{mon}}\frac{1}{r}\frac{\partial^2}{\partial r^2}r + V(r) \tag{4.4}$$

with eigenvalue E_0. Averaging over $\nu_0(r)$ and taking E_0 as the zero of energy gives the effective Hamiltonian

$$\hat{H}_\mathrm{mon} = b\hat{n}^2 + \hat{H}_\mathrm{ss} + \hat{H}_\mathrm{sn}. \tag{4.5}$$

The monomer rotational constant b is approximated by $b = \hbar^2/2\mu_{\text{mon}}r_e^2$ with r_e the equilibrium O$_2$ bond-length. The spin-spin term

$$\hat{H}_{\text{ss}} = \frac{2}{3}\lambda_{\text{ss}}\left[\frac{4\pi}{5}\right]^{\frac{1}{2}}\sqrt{6}\sum_q(-1)^q Y_{2-q}(\hat{r})[\hat{s}\otimes\hat{s}]_q^{(2)} \tag{4.6}$$

with $[\hat{s}\otimes\hat{s}]^2$ a tensorial product of $\hat{s}$ with itself and $Y_{2-q}(\hat{r})$ are spherical harmonics and the spin-rotation term

$$\hat{H}_{\text{sn}} = \gamma\hat{n}\cdot\hat{s}. \tag{4.7}$$

For O$_2$ the spin-spin constant $\lambda_{\text{ss}} = 1.9848$ cm^{-1} [295] and the spin-rotation constant $\gamma = -0.0084$ cm^{-1} [295]. The relative difference in magnitude of the constants points to the relative strength of the spin-spin interaction. The eigenfunctions and eigenvalues are obtained by standard matrix diagonalization. The matrix elements are

$$\langle sm_s|\langle nm_n|b\hat{n}^2|s'm_s'\rangle|n'm_n'\rangle = \delta_{nn'}\delta_{m_n m_n'}\delta_{ss'}\delta_{m_s m_s'}bn(n+1) \tag{4.8}$$

for the rotation,

$$
\begin{aligned}
\langle sm_s|\langle nm_n|\hat{H}_{\text{sn}}|s'm_s'\rangle|n'm_n'\rangle = {} & \delta_{nn'}\delta_{m_n m_n'}\delta_{m_s m_s'}\gamma m_n m_s + \delta_{nn'}\delta_{m_n m_n'\pm 1}\delta_{m_s m_s'\mp 1} \\
& \times \frac{\gamma}{2}[n(n+1) - m_n'(m_n'\pm 1)]^{1/2} \\
& \times [s(s+1) - m_s'(m_s'\mp 1)]^{1/2}
\end{aligned}
\tag{4.9}
$$

for the spin-rotation and

$$
\begin{aligned}
\langle sm_s|\langle nm_n|\hat{H}_{\text{ss}}|s'm_s'\rangle|n'm_n'\rangle = {} & \frac{2\sqrt{30}}{3}\lambda_{\text{ss}}(-1)^{s-m_s-m_n}[(2n+1)(2n'+1)]^{1/2} \\
& \times [s(s+1)(2s+1)]\begin{pmatrix} n & 2 & n' \\ 0 & 0 & 0 \end{pmatrix}\begin{Bmatrix} 1 & 1 & 2 \\ s & s & s \end{Bmatrix} \\
& \times \sum_q(-1)^q\begin{pmatrix} n & 2 & n' \\ -m_n & -q & m_n' \end{pmatrix} \\
& \times \begin{pmatrix} s & 2 & s' \\ -m_s & q & m_s' \end{pmatrix}
\end{aligned}
\tag{4.10}
$$

for the spin-spin interactions in the decoupled basis set [294]. The terms in ordinary and curly brackets are three-j and six-j symbols [296], respectively. In the coupled basis set we have

$$\langle snjm_j|\hat{n}^2|s'n'j'm_j'\rangle \;=\; \delta_{nn'}\delta_{ss'}\delta_{jj'}\delta_{m_jm_j'}bn(n+1) \tag{4.11}$$

for the rotation,

$$\langle snjm_j|\hat{H}_{\mathrm{sn}}|s'n'j'm_j'\rangle \;=\; \delta_{nn'}\delta_{jj'}\delta m_jm_j'\gamma(-1)^{n+j+s}$$
$$\times\,[n(n+1)(2n+1)s(s+1)(2s+1)]^{1/2}$$
$$\times\,\begin{Bmatrix} s & n & j \\ n & s & 1 \end{Bmatrix}, \tag{4.12}$$

for the spin-rotation and

$$\langle snjm_j|\hat{H}_{\mathrm{ss}}|s'n'j'm_j'\rangle \;=\; \delta_{jj'}\delta_{m_jm_j'}\frac{2\sqrt{30}}{3}\lambda_{\mathrm{ss}}(-1)^{j+n+n'+s}[(2n+1)(2n'+1)]^{1/2}$$
$$\times\,\begin{pmatrix} n & 2 & n' \\ 0 & 0 & 0 \end{pmatrix}\begin{Bmatrix} s & n' & j \\ n & s & 2 \end{Bmatrix} \tag{4.13}$$

for the spin-spin interactions. For ground-state molecular oxygen we must remember that $s = s' = 1$. The diagonal nature of the matrix elements with respect to s is therefore not emphasized in the expressions above.

The rotational term is diagonal in both basis sets with the same eigenvalue $bn(n+1)$. In the uncoupled representation the spin-rotation term makes different contributions to diagonal elements depending on the product $m_s m_n$ and couples states of the same rotational level that differ by 1 in m_n or m_s but have the same $m_n + m_s$. The spin-spin term couples rotational states that differ in rotational quantum number by exactly 2 (ie. $\Delta n = \pm 2$) but have the same $m_n + m_s$. So it is clear that in zero-field $m_n + m_s$ is a good quantum number. In the coupled basis set the spin-rotation term is completely diagonal while the spin-spin interaction
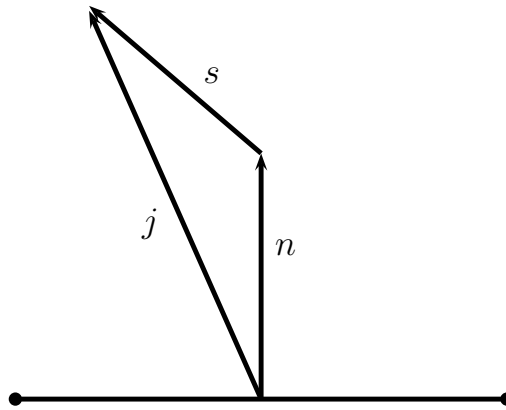
Figure 4.3: O$_2$ is very nearly a Hund's case (b) molecule.

couples terms with $\Delta n \pm 2$. As we would expect from discussion of the uncoupled representation all terms in the coupled basis are diagonal in m_j. In fact both m_j and j are good quantum numbers making the coupled representation a better one in zero field.

Diatomic molecules are also classified according to the relative coupling strengths of the different angular momenta. In O$_2$ the electronic spin s is coupled to the nuclear framework rotational angular momentum n to give the total angular momentum j as shown in figure 4.3. The ground state of molecular oxygen is nearly a Hund's case (b).

In a magnetic field we must add a Zeeman term

$$\hat{H}_z = g_e \mu_B \hat{B} \cdot \hat{s} \tag{4.14}$$

to the monomer Hamiltonian 4.5 where g_e is the g-factor for the electron, μ_B is the Bohr magneton and $\hat{B}$ is the magnetic field operator. Choosing our z-axis to coincide with the space fixed direction of the magnetic field, the matrix element is

$$\langle nm_n|\langle sm_s|\hat{H}_z|s'm_s'\rangle|n'm_n'\rangle = \delta_{nn'}\delta_{m_n m_n'}\delta_{m_s m_s'} g_e \mu_B B m_s \tag{4.15}$$

in the uncoupled representation and

Isotope ^{x}O	Atomic mass	Nuclear spin	b (cm^{-1}) of ^{x}O$_2$	Ground n
^{16}O	15.995	0	1.4377	1
^{17}O	16.999	$\frac{5}{2}$	1.3527	0 or 1
^{18}O	17.999	0	1.2776	1

Table 4.1: The atomic mass and nuclear spin of three isotopes of atomic oxygen, and the rotational constant and rotational ground-state quantum numbers of corresponding homonuclear diatomic molecules.

$$
\begin{aligned}
\langle nsjm_j|\hat{H}_z|s'n'j'm_j'\rangle &= \delta_{nn'}\delta_{m_jm_j'}g_e\mu_BB(-1)^{n+s-m_j+1} \\
&\times [s(s+1)(2s+1)(2j+1)(2j'+1)]^{\frac{1}{2}} \\
&\times \begin{pmatrix} j & 1 & {}'j \\ -m_j & 0 & m_j \end{pmatrix} \begin{Bmatrix} s & j' & n \\ j & s & 1 \end{Bmatrix}
\end{aligned}
\tag{4.16}
$$

in the coupled representation. We see that the Zeeman term is diagonal in the uncoupled representation but not in the coupled representation. This makes the choice of representation in the presence of a field a little more complicated. In the low-field limit where the Zeeman term is negligible the coupled basis is a better representation, however, in the high-field limit where the Zeeman term dominates the energy the uncoupled representation is better.

Usually, all the rotational levels of the molecular framework are allowed. However, this is not the case for molecules with identical nuclei. Homonuclear diatomic molecules are symmetric with respect to the interchange of the nuclei. This requires the total wavefunction, ψ_{mon}, which can be written as a product

$$
\psi_{\mathrm{mon}} = \psi_{\mathrm{el}}^{\mathrm{tot}} \cdot \psi_{\mathrm{vib}} \cdot \psi_{\mathrm{rot}} \cdot \psi_{\mathrm{ns}}
\tag{4.17}
$$

of the electronic, vibrational, rotational and nuclear spin components, respectively, to be either symmetric (eigenvalue $+1$) or antisymmetric (eigenvalue -1) with respect to nuclear permutation according to whether the nuclei are bosons or fermions,
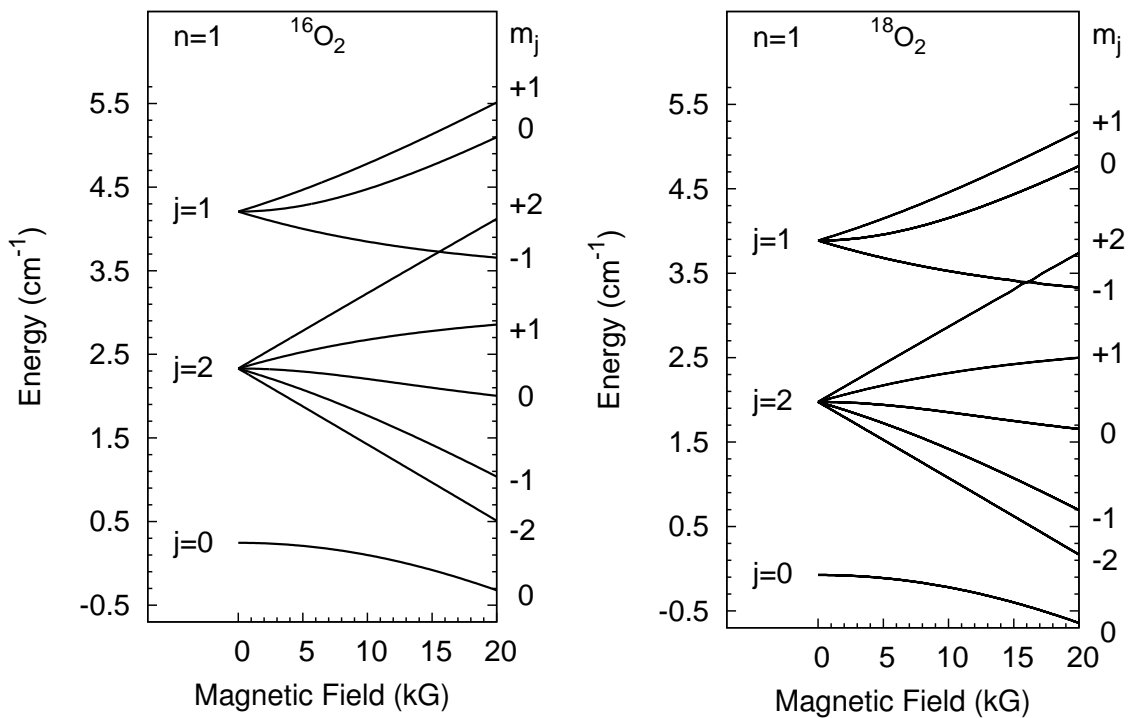
Figure 4.4: Rotational ground state levels of ^{16}O$_2$ and ^{18}O$_2$.

respectively. The vibrational wavefunction depends only on the magnitude of separation of the nuclei and is unaffected by permutation. For O$_2$ the electronic wavefunction is antisymmetric with respects to permutation. From table 4.1 ^{16}O and ^{18}O are bosons with nuclear spin 0 which only allows for the construction of molecular nuclear spin functions that are symmetric with respect to nuclear permutation. As the total wavefunction of ^{16}O$_2$ and ^{18}O$_2$ must be symmetric we must have rotational wavefunctions that are antisymmetric. The rotational functions $|n, m_n\rangle$ are symmetric for even n and antisymmetric for odd n. This means that ψ_{mon} can only contain odd rotational levels. An important consequence is that the ground rotational level is $n = 1$. For ^{17}O$_2$ the atomic nuclear spins is 5/2 from which both symmetric and anti-symmetric molecular nuclear spin functions can result. However, the nuclei are fermions and the wavefunction must be antisymmetric under permutation. This means that the even n rotational functions must combine with the symmetric nuclear spin functions while the odd n functions must combine with antisymmetric nuclear spin functions. The rotational levels of ^{17}O$_2$ are divided into even and odd n manifolds. For the even n levels the ground state is $n = 0$.
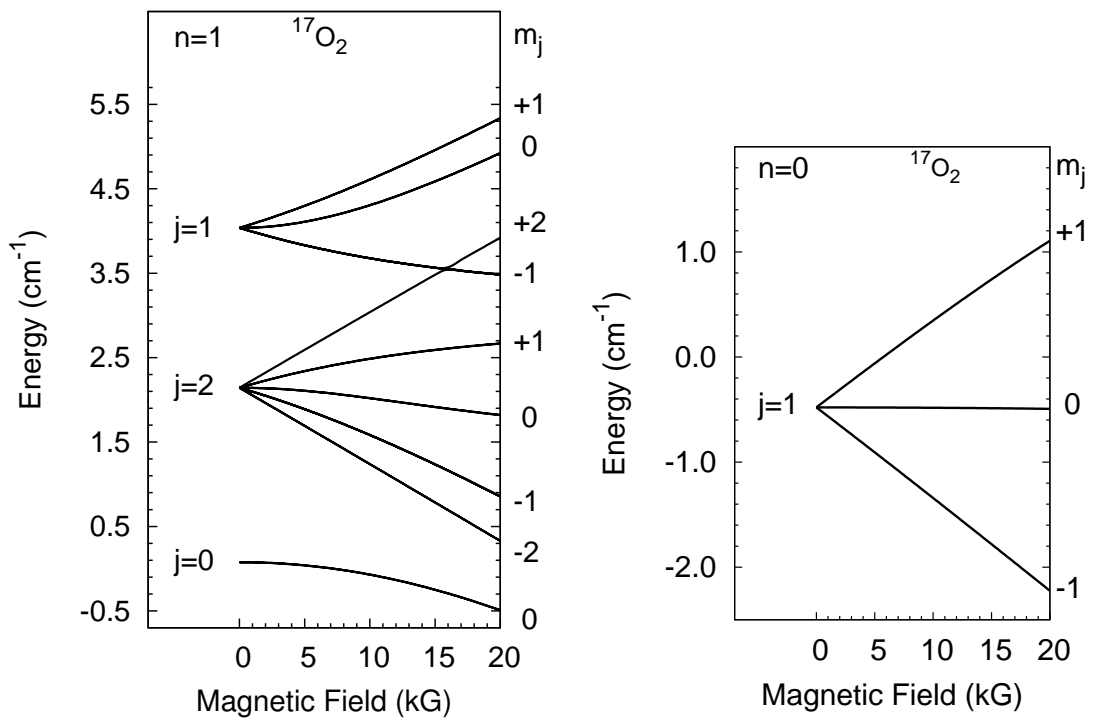
Figure 4.5: Rotational ground state levels of $^{17}O_2$ for the odd (left panel) and even n manifolds.

Let us consider the rotational ground state of $^{16}O_2$ depicted on the left panel of figure 4.4. These are $n = 1$ levels each with rotational energy $2b \approx 2.9$ cm^{-1}. There are three rotational functions $|nm_n\rangle$ for $n = 1$ and three spin functions $|sm_s\rangle$ for $s = 1$ giving a product of nine basis functions. As we have seen, the coupled representation is better at low fields so we use these in our initial interpretations. Restricting our basis set to $n = 1$ levels means that the spin-spin interaction makes no contribution. However, the spin-rotation interaction has contributions that depend only upon j which has values $0, 1$ and 2. Because at zero field all contributions are diagonal in m_j, we can predict three levels, one for each j. This is consistent with the figure 4.4. Although the Zeeman term is diagonal in m_j it depends on the actual value of m_j. This has the effect of lifting the degeneracy of the different m_j levels within the same j. So in non-zero field $j = 2$ splits into $m_j = \pm 2, \pm 1, 0$ and $j = 1$ into $m_j = \pm 1, 0$ while $j = 0$ remains a single $m_j = 0$ level. Once a field is applied we have nine separate levels, equal to the size of our restricted basis set which is independent of the choice of representation. This means that all degeneracy

has been lifted. We also note that 2.9 cm^{-1} is nearly at the middle of the levels. The spin-rotation term will split levels of the same n according to j and n and the spin-spin terms will couple levels of $\Delta n = \pm 2$ shifting them according to j and n. It is only the Zeeman term that breaks the isotropy of space and couples different j, destroying the total angular momentum as a good quantum number. If we identify the direction of the projection of j with that of the field, then m_j is conserved by all interactions, including the Zeeman term, reflecting the rotational symmetry about the axis defined by the field. The m_j remains a good quantum number at any field.

Although the j quantum number is not strictly a good quantum number it is approximately good for low fields. In this region the pair (j, m_j) is a good label for the levels. From figure 4.4 we note that the low-field region extends to approximately 15000 G at which point the lines $(2, +2)$ and $(1, -1)$ cross. In reality, the levels of the same symmetry avoid crossing so that even from the high field limit it is possible to adiabatically follow a label (j, m_j) unambiguously back to a single level allowing us to retain the labels if we choose. However, the character of the levels are mixed and these labels no longer retain reliable information on the nature of the levels. In the limit of very high fields known as the *Paschen-Back limit*, where the Zeeman contribution is dominant, n and s are decoupled from each other and are independently coupled to the field. This means that j is no longer a good quantum number, even approximately, but m_s becomes approximately a good quantum number. As $m_s = \pm 1, 0$ and each m_s can couple with the three m_n of $n = 1$ there should be three sets of levels with each set triply degenerate. The groups of levels and the corresponding m_s are shown in figure 4.6 which depicts ^{16}O$_2$ levels up to 40 kG. Strictly, it is the gradient of each set of levels that approaches the same limit. As the levels are at different energies to start with it is clear that they cannot become degenerate. However, in the limit of very hight field the difference, which originates from all the other terms, becomes less significant. The energy is almost entirely due to the interaction with the field, which, from equation 4.15, is equal for levels with the same m_s making them essentially degenerate.
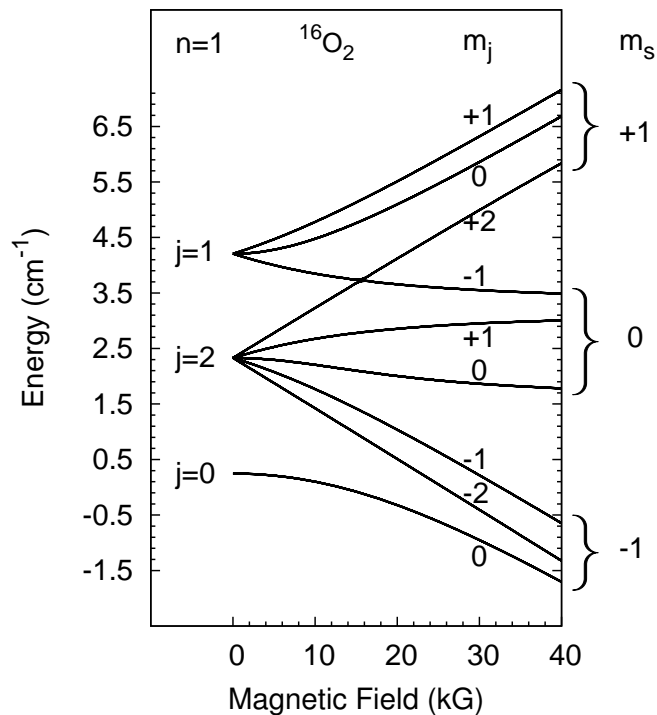
Figure 4.6: The Zeeman structure beyond the boundary of the *Paschen-Back* limit of the ground rotational level of $^{16}O_2$.

On comparison of $^{16}O_2$, $^{18}O_2$ and odd n levels of $^{17}O_2$ shown in figures 4.4 and 4.5 we see that the pattern of levels is essentially the same. The increase in mass has the effect of reducing the rotational constant b which reduces the energy of the levels and their separation. The $j = 0$ levels are at 0.2459 cm^{-1}, 0.0760 cm^{-1} and -0.0743 cm^{-1} for $^{16}O_2$, $^{17}O_2$ and $^{18}O_2$, respectively. Similarly, the $j = 2$ levels are at 2.330 cm^{-1}, 2.143 cm^{-1} and 1.975 cm^{-1}, respectively. For the even n levels of $^{17}O_2$, the ground rotational state is $n = 0$. This gives $j = s = 1$ and $-1 \leq m_j = m_s \leq 1$. Figure 4.5 shows the three levels of the ground state. We see that the gradient of the $m_j = \pm 1$ levels have the same magnitude but opposite sign and the $m_j = 0$ level is unaffected by the field as would be expected when the contributions to the m_j are only from m_s.

For O_2 molecules with nonidentical oxygen atoms, such as $^{16}O^{17}O$ and $^{16}O^{17}O$, nuclear permutation symmetry does not apply. All rotational states are allowed and, as shown in figure 4.7, the ground state is $n = 0$ and the first excited state is $n = 1$.
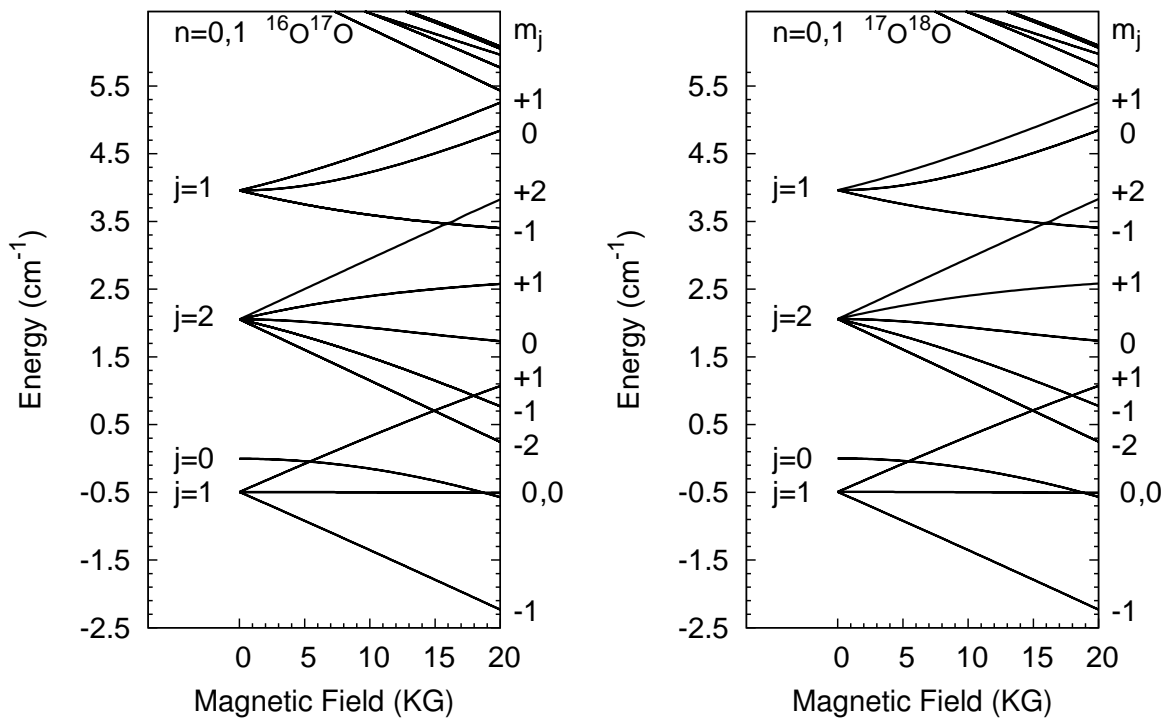
Figure 4.7: Rotational ground, $n = 0$, and first excited state, $n = 1$, of $^{16}O^{17}O$ and $^{17}O^{18}O$.

The sub-levels of these two levels are also not far apart with the $|nsjm_j\rangle = |1110\rangle$ and $|nsjm_j\rangle = |0110\rangle$ states avoided-crossing at approximately 18,500 Gauss. We also note that the levels visible on the top right of the figures are $n = 2$ levels which come within the plotted range at about 7,000 Gauss. The difference between the levels of the two diatomic molecules is not easily visible on the scale of the graphs. The lowest two levels at zero field for example are -0.4950 cm^{-1} and -0.0039 cm^{-1} for $^{16}O^{17}O$ and -0.4941 cm^{-1} and 0.008 cm^{-1} for $^{17}O^{18}O$. Our bound and scattering state calculations are restricted to homonuclear molecules and we do not consider non-identical Oxygen complexes any further.

4.3 Potential energy surface (PES)

In this section we will outline the basic ideas that underpin the calculation of the interaction energy $V(R, r, \Theta)$. In the absence of a field, and ignoring fine and hyperfine

interaction, the full Hamiltonian $\hat{H}$ of a molecule can be written as

$$\hat{H} = \hat{T}_{\mathrm{N}}(\mathbf{R}) + \hat{T}_{\mathrm{e}}(\mathbf{x}) + V_{\mathrm{eN}}(\mathbf{x}, R) + V_{\mathrm{ee}}(\mathbf{x}) + V_{\mathrm{NN}}(\mathbf{R}). \tag{4.1}$$

The first two terms on the right-hand side are nuclear and electronic kinetic energy operators with $\mathbf{R}$ and $\mathbf{x}$ the nuclear and electronic coordinates respectively. The other terms are the sum of electron-nuclear, electron-electron and nuclear-nuclear interactions. Not surprisingly, this equation is impossible to solve exactly, even for relatively few particles, and simplifying approximations must be made. The first is the separation of the electronic and nuclear motions. This is the Born-Oppenheimer approximation and it has physical basis in the fact that the nuclei are much more massive than the electrons. The electrons in effect respond instantaneously to any motion of the nuclei. This approximation allows us to separate an electronic Hamiltonian $\hat{H}_{\mathrm{elec}}$

$$\hat{H}_{\mathrm{elec}}(\mathbf{x}; R) = \hat{T}_{\mathrm{e}}(\mathbf{x}) + V_{\mathrm{ee}}(\mathbf{x}) + V_{\mathrm{eN}}(\mathbf{x}; R) \tag{4.2}$$

and to conveniently write the total wavefunction as a product of a nuclear and electronic wavefunction. The electronic wavefunction $\Psi_{\mathrm{elec}}(\mathbf{x}; R)$ satisfies

$$\hat{H}_{\mathrm{elec}}\Psi_{\mathrm{elec}}(\mathbf{x}; R) = E_{\mathrm{elec}}\Psi_{\mathrm{elec}}(\mathbf{x}; R), \tag{4.3}$$

an eigenvalue equation with a parametric dependence on the nuclear coordinates $\mathbf{R}$. The solutions $\Psi_{\mathrm{elec}}(\mathbf{x}; R)$ and the corresponding energies E_{elec} calculated for different geometries give us the electronic structure and the potential energy surface on which the nuclei move.

The starting point for many modern electronic structure calculations is the Hartree-Fock self-consistent field method. This is a variational method which con-

structs the trial solution from a set of molecular spin-orbitals $\chi_i(\mathbf{x}_j)$ in the form

$$\Psi^{\mathrm{HF}} = \frac{1}{\sqrt{M!}} \begin{vmatrix} \chi_1(\mathbf{x}_1) & \chi_2(\mathbf{x}_1) & ...... & \chi_M(\mathbf{x}_1) \\ \chi_1(\mathbf{x}_2) & \chi_2(\mathbf{x}_2) & ...... & \chi_M(\mathbf{x}_2) \\ .... & .... & .... & .... \\ .... & .... & .... & .... \\ \chi_1(\mathbf{x}_M) & \chi_2(\mathbf{x}_M) & ...... & \chi_M(\mathbf{x}_M) \end{vmatrix} \tag{4.4}$$

where M is the number of electrons and $\mathbf{x}_j$ represents the spacial and spin coordinates of electron j. The spin-orbitals (or simply orbitals from here on) are a product of spacial and spin wavefunctions. The determinant is referred to as a Slater determinant and satisfies the symmetry requirements imposed by the Pauli principle. The molecular orbitals are themselves a linear combinations of atomic orbitals centered at the nuclei. Optimization involves varying the coefficients and is done one molecular orbital at a time. The process is repeated until the set of orbitals are unchanged or *self consistent*. For better solutions, the atomic orbitals are usually from the best available atomic calculations and include the first few virtual (unoccupied) orbitals. Atomic orbitals with higher angular momentum than is required for the atomic ground state are included in order to better reproduce polarization properties. For a system with M electrons the ground state is the determinant constructed from the first M molecular spin-orbitals. Excited states are obtained by replacing some of these with higher energy molecular spin-orbitals. Singly excited states replace one orbital, doubly excited states replace two *etc*. A common practice employed when there are an even number of electrons is to restrict them to pair up. This is done by requiring each spacial component of $\chi_i(\mathbf{x}_j)$ be occupied by two electrons of opposite spin. This reduces the number of spacial orbitals reducing computational cost. This practice is referred to as restricted Hartree-Fock, or RHF for short. Unrestricted Hartree-Fock produces lower and therefore better energies at higher computational cost. The restricted open-shell formalism is a compromise employed for open-shell systems. It applies the restriction to the electrons occupying closed shells, relaxing it for the electrons in the open shell.

Hartree-Fock is a mean-field theory which treats the interaction of an arbitrary electron with all others in an averaged way. The position of any one electron is assumed not to affect the position of the others. In reality, electron motion is correlated and the largest error in the energy as determined by self-consistent methods originates from failure to account for this effect. There are several methods that extend Hartree-Fock to correct for correlation. One such method used in the calculation of the PES of Groenenboom and Struniewicz [292] is the coupled cluster approach. In the coupled cluster method the ground state solution Ψ^{CC} is expanded as

$$\Psi^{CC} = e^{(\hat{T})}\Psi^{HF} \tag{4.5}$$

where

$$\hat{T} = \hat{T}_1 + \hat{T}_2 + \hat{T}_3 + ... \tag{4.6}$$

with the operator $\hat{T}_1$ turning the Hartree-Fock ground-state function into a linear combination of singly excited states, $\hat{T}_2$ into a linear combination of doubly excited states *etc*. Typically, the sum is truncated at the second or third term. The exponential ensures that coupled cluster is size-consistent but must in practice also be truncated after a few terms. When the truncation stops at triply excited states computational cost scales as the seventh power of the size of the basis set. The coupled cluster method is highly accurate for small to medium sized systems.

Groenenboom and Struniewicz [292] used the Jacobi coordinate system depicted by figure 4.8. They used the partially restricted coupled cluster method with single, double and triple excitations or RCCSD(T) for short. The restriction was applied to electrons of the closed 1s shell of oxygen. The "T" in brackets indicates that the triply excited states were included perturbatively. Augmented correlation-consistent triple-zeta (aug-cc-pVTZ) basis set was employed with additional bonding functions between He and O_2. The calculations were corrected for basis set superposition error using the Boys and Bernardi [297] method. All three coordinates (r, R and Θ) were varied producing a 3-dimensional hypersurface from 754 geometries. Symmetry considerations allowed Θ to be restricted between $0°$ and $90°$. Particular care was
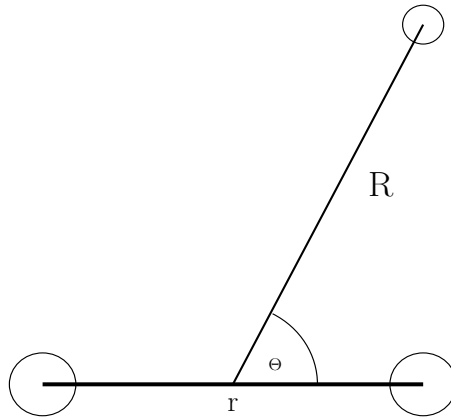
Figure 4.8: The Jacobi coordinate system for He-O_2. The distance r is the separation between the two oxygen atoms of O_2, R is the distance between the centers of mass of the oxygen molecule and He, and Θ the angle between the vectors $\mathbf{R}$ and $\mathbf{r}$.

taken to reproduce the long-range properties.

In our calculations the O-O bond length is frozen to the equilibrium value $r = r_e = 2.282$ a_0 (1.208 Å). Figure 4.9 depicts the equipotential lines of the PES of He-O_2 with the bond length fixed at this equilibrium value. The energy is in units of cm^{-1}. For $r_e = 2.282$ a_0 Groenenboom and Struniewicz [292] report a global minimum of -127.71 μE_h (-27.90 cm^{-1}), with E_h the atomic unit of energy of Hartree, at a T-shape geometry ($\Theta = 90°$) with a separation $R = 6.0$ a_0 (3.18 Å). There are two local minimum -116.4 μE_h (-25.55 cm^{-1}) deep at a linear geometries $\Theta = 0.0°$ and $\Theta = 180.0°$ at a distance $R = 6.9$ a_0 (3.65 Å). The saddle point, 36.8 μE_h (8.08 cm^{-1}) above the global minimum is at $\Theta = 49°$, $R = 6.8$ a_0 (3.60 Å). Figure 4.10 shows cross sections of the PES at various angles. The repulsive wall starts at very different distances for the different angles. The minima also occur at different distances. For $\Theta = 90°$ the curve shows a minimum at the distance of approximately 6.0 a_0 consisted with the reported global minimum.
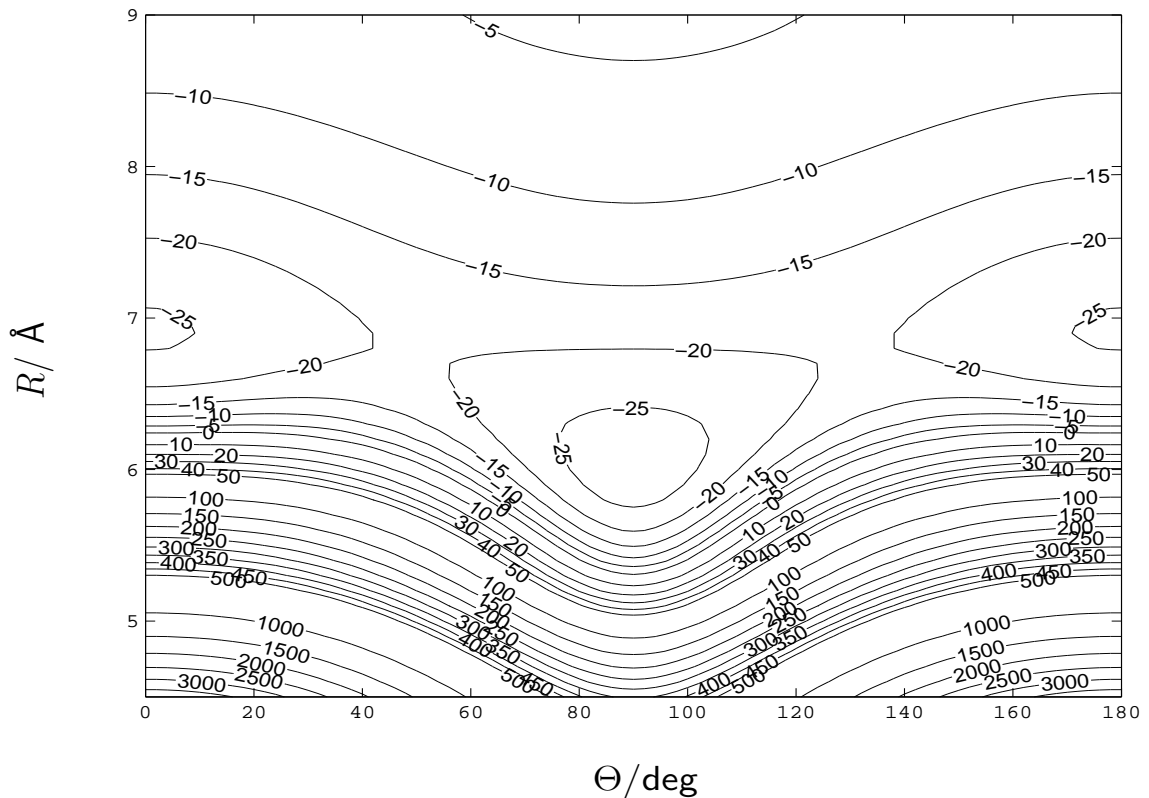
Figure 4.9: Potential energy surface, in cm^{-1}, of He+O$_2$ with O$_2$ with bondlength held at $r_\text{e} = 1.208$ Å.

4.4   Bound state equations

We can recast equation 4.1 as

$$\hat{H}_\text{c} = -\frac{\hbar^2}{2\mu} R^{-1} \frac{d^2}{dR^2} R + \frac{\hat{L}^2}{2\mu R^2} + \hat{H}_\text{mon} + V(R, \Theta) \qquad (4.7)$$

where the kinetic energy term has been separated into the relative radial and angular motions of the pair. The $\hat{L}^2$ is the space-fixed end-over-end angular momentum operator as discussed earlier. We have dropped the r from the potential $V(R, \Theta)$ as we have fixed it to the equilibrium value. The potential is fitted to a functional form

$$V(R, \Theta) = \sum_\lambda P_\lambda(\cos\Theta) V_\lambda(R) \qquad (4.8)$$

where the $P_\lambda(\cos\Theta)$ are Legendre polynomials. The argument $\cos\Theta$ is used due to cylindrical symmetry. For a homonuclear molecule such as O$_2$, symmetry about $\Theta = 90°$ means that only the even polynomials are present in the expansion. These
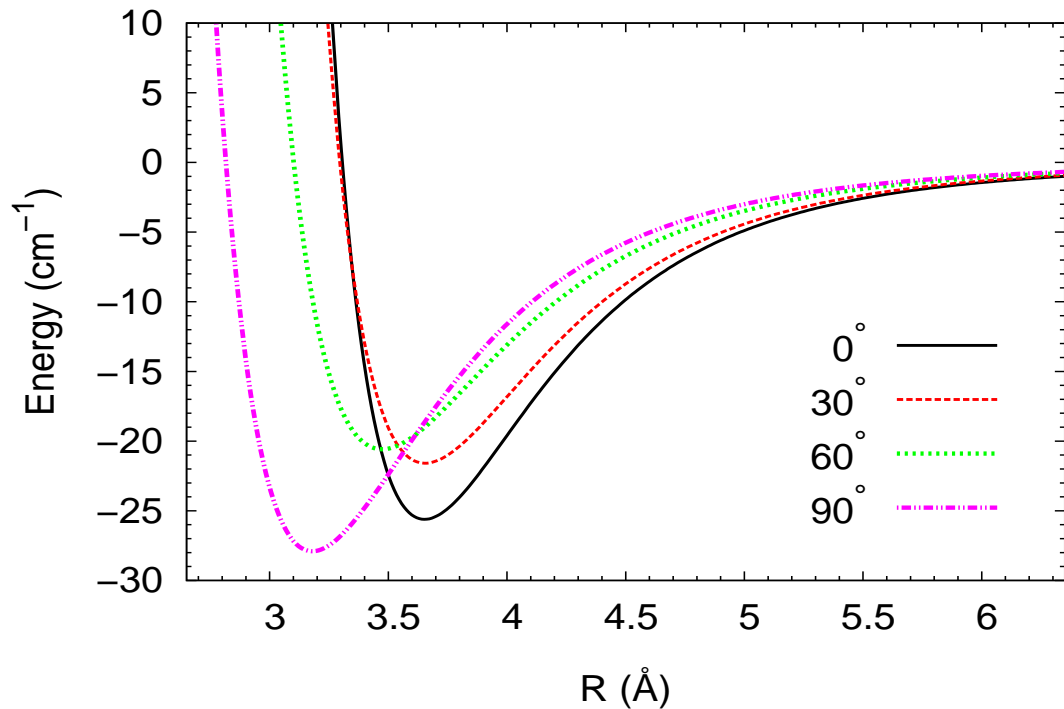
Figure 4.10: Potential energy curves across the interaction surface, $V(R, \Theta)$, at $\Theta = 0°, 30°, 60°,$ and $90°$. The minimum of the curves at $0°$ and $90°$, which corresponds to the local and global minimum respectively, are consistent with the reported estimate [292].

correspond to even values of λ. The bound states are calculated using the coupled-channel method with the total wavefunction $\Phi(R, \Omega)$ expanded as

$$\Phi(R, \Omega) = R^{-1} \sum_{\beta} \chi(R)_{\beta} \psi_{\beta}(\Omega). \tag{4.9}$$

The $\psi_{\beta}(\Omega)$ are channel functions with β denoting a channel $|sm_s\rangle|nm_n\rangle|LM_L\rangle$ in the uncoupled representation or $|nsjm_j\rangle|LM_L\rangle$ in the coupled representation. The inclusion of the angular momentum basis set $|LM_L\rangle$ reflects the corresponding end-over-end degree of freedom of the complex. The matrix elements of the Legendre polynomials are given by [294]

$$\langle LM_L|\langle nsjm_j|P_\lambda(\cos(\Theta))|n's'j'm'_j\rangle|L'M'_L\rangle = [(2n+1)(2n'+1)(2j+1)(2j'+1)]^{\frac{1}{2}}$$

$$\times [(2L+1)(2L'+1)]^{\frac{1}{2}} \begin{pmatrix} n & \lambda & n' \\ 0 & 0 & 0 \end{pmatrix}$$

$$\times \begin{pmatrix} L & \lambda & L' \\ 0 & 0 & 0 \end{pmatrix}$$

$$\times \sum_{m_\lambda} (-1)^{s+j+j'+\lambda+m_\lambda-M_L-m_j}$$

$$\times \begin{pmatrix} L & \lambda & L' \\ -M_L & -m_\lambda & M'_L \end{pmatrix}$$

$$\times \begin{pmatrix} j & \lambda & j' \\ -m_j & m_\lambda & m'_j \end{pmatrix}$$

$$\times \begin{Bmatrix} j & j' & \lambda \\ n' & n' & s \end{Bmatrix} \tag{4.10}$$

in the coupled representation and

$$
\begin{aligned}
\langle LM_L | \langle nm_n | \langle sm_s | P_\lambda(\cos(\Theta)) | s'm'_s \rangle | n'm'_n \rangle | L'M'_L \rangle \;=\;& \delta_{m_s m'_s} [(2n+1)(2n'+1)]^{\frac{1}{2}} \\
& \times [(2L+1)(2L'+1)]^{\frac{1}{2}} \\
& \times \begin{pmatrix} n & \lambda & n' \\ 0 & 0 & 0 \end{pmatrix} \\
& \times \begin{pmatrix} L & \lambda & L' \\ 0 & 0 & 0 \end{pmatrix} \\
& \times \sum_{m_\lambda} (-1)^{m_\lambda - M_L - m_j} \\
& \times \begin{pmatrix} L & \lambda & L' \\ -M_L & -m_\lambda & M'_L \end{pmatrix} \\
& \times \begin{pmatrix} n & \lambda & n' \\ -m_n & m_\lambda & m'_n \end{pmatrix}
\end{aligned}
$$

(4.11)

in the uncoupled representation. These elements are off-diagonal in both representations. The isotropic part of the potential does not couple different channels. As the potential has no odd terms we note from the matrix element in both representations that the first anisotropic term $P_2(\cos\Theta)$ couples terms with $\Delta n = \pm 2$. From 4.10 we note that potential elements that couple channels with $\Delta m_j = m_\lambda$ also couple channels with $\Delta M_L = -m_\lambda$ so that there is no coupling of channels with different $M_J = m_j + M_L$. In the uncoupled representation the interaction potential is diagonal in m_s and couples channels with different m_n and M_L in such a way that the sum $m_n + M_L$ is conserved leading, as in the coupled representation, to the conservation of $M_J = m_n + m_s + M_L$.

The calculations are performed using BOUND [279, 298, 299]. The radial component is propagated outward from a point $R_{\min}$ and inward from a point $R_{\max}$ using

a log-derivative propagator. Apart from the basis set the mid and boundary points and the propagation step-size, which we denote by ΔR, must be fixed. Convergence tests of the energy levels were performed for each of these variables. As there is considerable experience in the group, choosing initial values did not present a challenge and the tests were aimed at tuning the values to the He-O$_2$ system. We chose ^{4}He-^{16}O$_2$ as our representative system. Convergence calculations were performed at zero field and the results are presented below.

4.5 Convergence calculations

The first convergence investigation tested convergence of the energy levels with respect to the size of the basis set. With the spin basis functions fixed by the spin value, $s = 1$, there was the possibility to choose the size of rotational $|nm_n\rangle$ and end-over-end $|LM_L\rangle$ basis functions. In BOUND, this is chosen by setting the maximum values of n and L, which we refer to as $n_{\max}$ and $L_{\max}$, respectively. The initial propagation points were set at $R_{\min} = 1.0$ Å and $R_{\max} = 15.0$ Å. As we can see from figure 4.10, these values place the points deep inside their respective classically forbidden regions. The mid point R_{mid} was set at 3.5 Å, and the step size ΔR to 0.02 Å. The calculations were done at zero field for a range of energies that spans the depth of the interaction energy. The basis set was varied by changing both $n_{\max}$ and $L_{\max}$. With no reason to expect any basis to have a more important effect, we imposed the constraint $n_{\max} = L_{\max}$. This would allow us to investigate the change in the combined basis. The results are shown in figure 4.11. The left panel shows the whole bound-state energy range.

We note that on the scale of the graph there is visible reduction in the energy of most states up to $n_{\max} = L_{\max} = 7$. Between $L_{\max} = 5$ and 7 the changes in the least-bound states are more clearly visible. The right panel, which shows the four least-bound states allows us to discern a further reduction in the energy of the least-bound state as $L_{\max}$ is increased to 9. Another important observation is that we do not always have all the states for any given $L_{\max}$. In fact for $L_{\max} = 1$ there
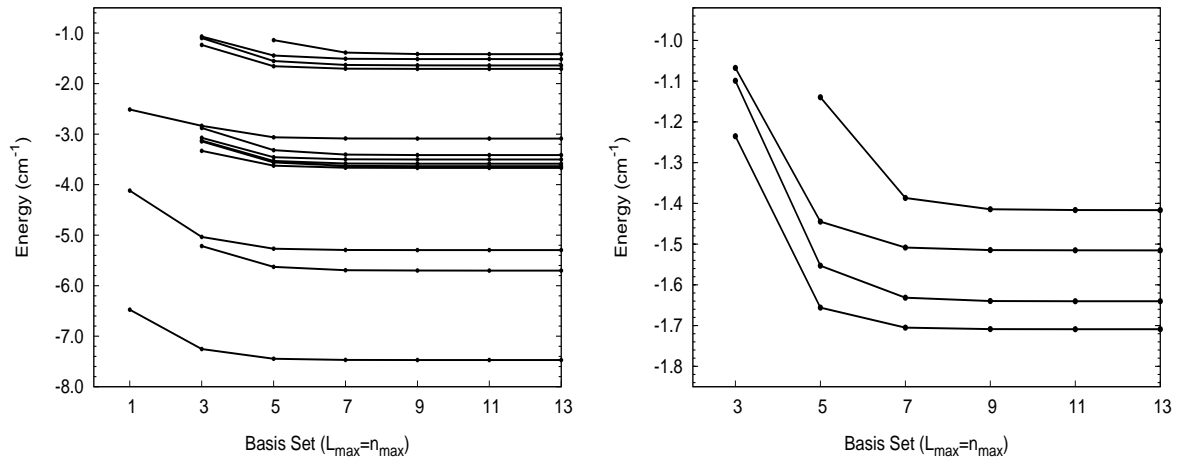
Figure 4.11: Convergence test of ^{4}He-^{16}O$_2$ levels with respect to the basis set. The x-axis indicates the size of the basis set $|sm_s\rangle|nm_n\rangle|LM_L\rangle$ defined by $L = n$ and $s = 1$. The left panel shows all bound states, while the right panel shows the four least-bound states.

are only *three* levels. The calculations are restricted to even parity which restricts L to even values, so that for $L_{\mathrm{max}} = 1$ only the $L = 0$ basis set is included. The end-over-end quantum number is an approximately good quantum number, and as we shall see following complete characterization of the bound states, there are three bound levels in the energy range in question belonging to $L = 0$. We are also able to conclude that all the remaining bound states, except the least bound one which first appears at the basis set size $L = 5$ and therefore belongs to $L = 4$, belong to $L = 2$ surfaces.

Having decided on a basis set defined by $n_{\mathrm{max}} = L_{\mathrm{max}} = 9$ we proceeded to vary the step size. All other variables were unchanged. Calculations were performed for five step sizes. The results are shown in figures 4.12. Once again the left panel shows all the levels while the right shows the four least-bound states. The figures show no discernable changes in the energy of the levels. However, figure 4.13 shows the least-bound state on its own. In the left panel we see a clear change in the energy, however, the changes are in the fifth significant figure. We are ultimately interested in locating low energy resonances. From the figures of the O$_2$ Zeeman structure we note that the threshold levels change by roughly 1 cm^{-1} in the 20 kG range,
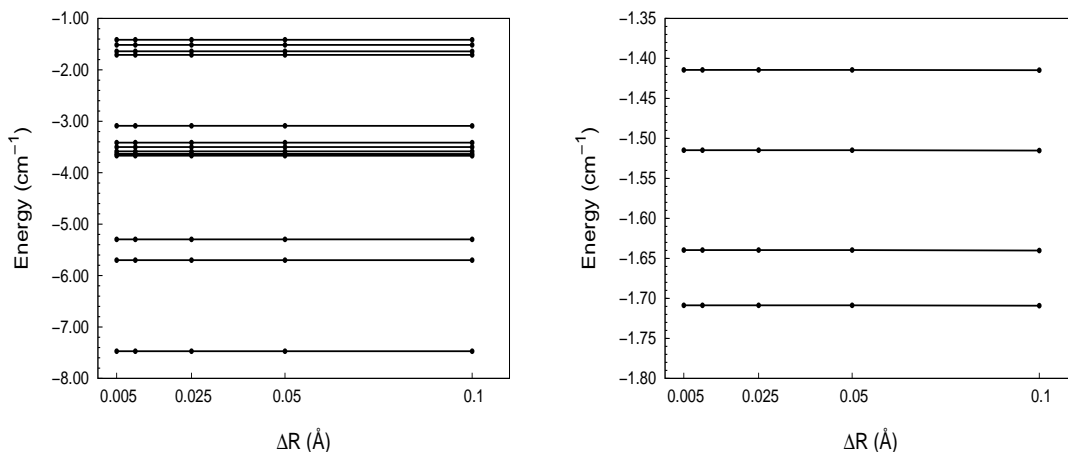
Figure 4.12: Convergence test of bound states of ^{4}He-^{16}O$_2$ with respect to ΔR. The left panel shows all states, while on the right panel shows the four least-bound states.

which corresponds to a gradient of approximately 5×10^{-5} cm^{-1}/ G. This means that the changes in energy of the least-bound state, which is of the order 10^{-4} cm^{-1} for the range of ΔR considered, will shift the position of the resonance by about 10 Gauss. The right panel of figure 4.13 shows the computing time taken for the various ΔR. The time increases nearly ten-fold between the two extreme values of ΔR. Comparing the two panels of 4.13 we conclude that a value of $\Delta R = 0.02$ Å presents a good compromise between computational time and the convergence of the levels. We note in particular that it is about four-fold in the computational time compared to the largest step-size ($\Delta R = 0.1$ Å), but reduces the difference with the best value by an order of magnitude. The remaining parameters were set, based on similar convergence tests, to $R_{\text{max}} = 15.0$ Å, $R_{\text{min}} = 1.7$ Å, and $R_{\text{mid}} = 3.5$ Å.

4.6 Bound states

In the absence of a field the total angular momentum $J = j + L$ and its projection M_J are rigorously good quantum numbers and must be used to label the bound states. However, He-O$_2$ is weakly anisotropic and the monomer quantum numbers n, s, j and the end-over-end angular momentum L are approximately conserved. This makes them a useful set of labels for understanding the bound-state spectrum. In addition, bound states are of even or odd parity $P = (-1)^{L+n+1}$ depending on
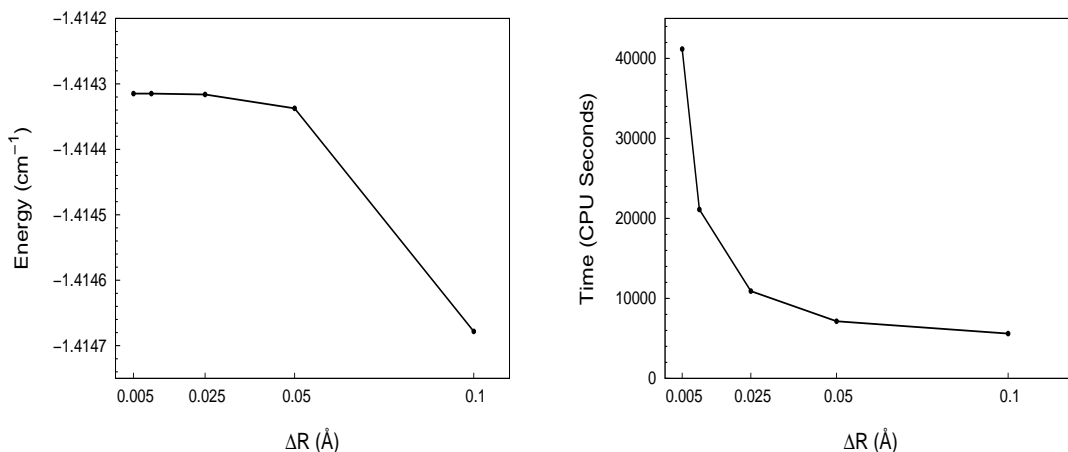
Figure 4.13: Left panel shows convergence of the highest bound state with respect to ΔR. The right panel shows ΔR versus time in CPU seconds.

whether $P = +1$ or $P = -1$ respectively. Even in the presence of a magnetic field parity remains a good quantum number and levels of different parity do not interact. In our study we are interested ultimately in characterizing zero-energy resonances. This requires the interaction of a discrete state with a scattering state dominated by the $L = 0$ partial wave. For collisions of He with O_2 molecules in the $n = 1$ ground states, the relevant scattering and bound states are of even parity.

Table 4.2 is a listing of the even-parity energy levels of four He-O_2 complexes involving molecular oxygen with ground state $n = 1$. As vibrational motion is frozen the largest contribution to the energy of the complex, apart for the interaction, is due to rotation of the O_2 monomer. For $^{16}O_2$ the first excited rotational state of $n = 3$ has energy $12b \approx 17.25$ cm^{-1}, much higher than the binding energy of the deepest levels of the complexes. This indicates that all the bound states belong to the rotational ground state. In fact this becomes clearer from the pattern of levels in a magnetic field as we shall see latter. At zero field, the rotational ground state $n = 1$ level of O_2 has three sub-levels $j = 0, 2$ and 1, respectively. For the bound states of the complex, the O_2 molecule, in any one of these levels, binds to He with the whole complex potentially rotating with an end-over-end angular momentum L to give a series of closely spaced levels with total angular momentum values J

ranging from $|L - j|$ to $|L + j|$.

Let us take for example the ^{3}He-^{16}O$_2$ system. Its lowest level is at -6.1018 cm^{-1}. This state belongs to the lowest ^{16}O$_2$ threshold with no end-over-end angular momentum. The pair $(j = 0, L = 0)$ can only result in a total angular momentum $J = 0$, which is indeed the total angular momentum of the lowest level. The second deepest level at -4.1089 cm^{-1} has the same $j = 0$ state but the monomers are rotating about each other. The first allowed end-over-end excitation of the complex is $L = 2$ which, assuming an equilibrium separation corresponding to the potential minimum, requires and energy of about 2.5 cm^{-1}. This energy is approximately the difference between the two lowest levels. Similarly, the second allowed end-over-end excitation $L = 4$ would require an energy of roughly 8 cm^{-1} which would place a $j = 0, L = 4$ level at approximately 2 cm^{-1} above threshold. In fact the $(j, L, J) = (0, 4, 4)$ level is at 1.0498 cm^{-1}. This level is a quasi-bound state included here to illuminate the discussion. We will discuss quasi-bound levels in greater detail in the next chapter.

The first level with $j = 2$ at -3.7375 cm^{-1} is 2.3643 cm^{-1} above the lowest. This difference is roughly the difference between $j = 0$ and $j = 2$ levels of ^{16}O$_2$ which is 2.0843 cm^{-1}. Figure 4.14 shows bound levels of ^{3}He-^{16}O$_2$ and ^{4}He-^{16}O$_2$ plotted according to their j quantum numbers in order to make the pattern of levels more apparent. The L quantum numbers are also indicated to the left of the levels. Naturally only parity-allowed L quantum numbers are present and appear in ascending order up the energy scale. So the first level of each j is an $L = 0$ level and as j and L pair to give J these levels have $J = j$ and always occur individually. Levels belonging to $j = 0$ also occur singly because for these levels $J = L$. For an end-over-end excited complex with j equal to 1 or 2 there are several closely packed levels. For example for ^{4}He-^{16}O$_2$ with $j = 1$ and $L = 2$ there are three levels, $J = 1,2$ and 3. The corresponding levels for ^{3}He-^{16}O$_2$ are quasi-bound and do not appear in the figure, but, they are listed in table 4.2 for illustration. For both complexes the
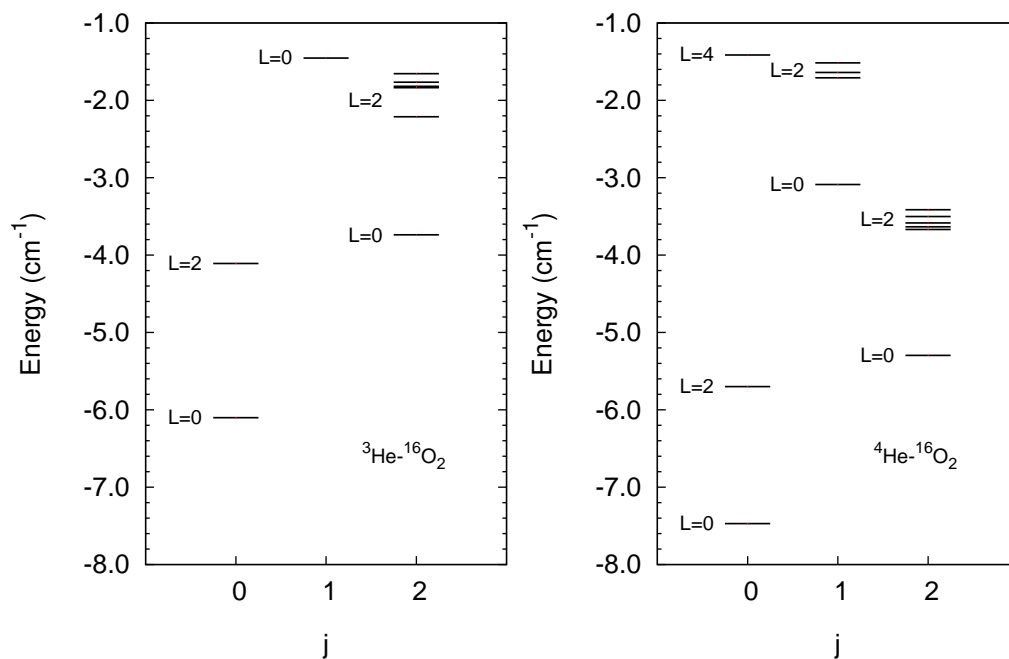
Figure 4.14: Bound states of ^{3}He-^{16}O$_2$ and ^{4}He-^{16}O$_2$ shown according to their j quantum number. Like L, the j quantum number is only an approximately good quantum number, but it is indispensable for an understanding of the pattern of levels.

pair $j = 2$ and $L = 2$ result in four bound states with $J = 0, 1, 2, 3$ and 4.

The difference in the levels shown in the left and right hand panels of Figure 4.14 reveal the effects of increased mass. The lowest level of ^{4}He-^{16}O$_2$ is at -7.4713 cm^{-1}. The increase in mass pulls the levels further down the potential well and at the top end what were quasi-bound states in ^{3}He-^{16}O$_2$ have been pulled below threshold increasing the total number of bound states from 9 for ^{3}He-^{16}O$_2$ to 13 for ^{4}He-^{16}O$_2$. As the bottom of the well remains at the same position the increase in levels reduces their separation but leaves the pattern essentially unchanged.

The pattern of levels for the even n manifold of ^{17}O$_2$ is quite different to that of the odd levels. For this reason the pattern of bound states of ^{4}He-^{17}O$_2$ is different to the complexes we have discussed so far. The levels and their quantum numbers are shown in table 4.3. The difference in energy between the deepest and least-bound

Table 4.2: Field-free even-parity levels of ^{3}He-^{16}O$_2$, ^{4}He-^{16}O$_2$, ^{4}He-^{17}O$_2$ (for the odd rotational manifold of ^{17}O$_2$) and ^{4}He-^{18}O$_2$. The first column indicates the total angular momentum quantum number J which is a rigorously good quantum number. The second column is the approximate good quantum number L.

		^{3}He-^{16}O$_2$	^{4}He-^{16}O$_2$	^{4}He-^{17}O$_2$ (odd n)	^{4}He-^{18}O$_2$
J	L	Energy(cm^{-1})	Energy(cm^{-1})	Energy(cm^{-1})	Energy(cm^{-1})
0	0	-6.1018	-7.4713	-7.6888	-7.8823
2	2	-4.1089	-5.7001	-5.9311	-6.1373
2	0	-3.7375	-5.2957	-5.5255	-5.7309
1	2	-2.2119	-3.6694	-3.8912	-4.0984
3	2	-1.8360	-3.6345	-3.8791	-4.0886
2	2	-1.8184	-3.5846	-3.8284	-4.0468
0	2	-1.7651	-3.5012	-3.7493	-3.9724
4	2	-1.6560	-3.4143	-3.6558	-3.8721
1	0	-1.4540	-3.0883	-3.3123	-3.5117
1	2	$+0.0628$	-1.7086	-1.9337	-2.1338
3	2	$+0.1355$	-1.6396	-1.8653	-2.0660
2	2	$+0.2289$	-1.5147	-1.7383	-1.9371
4	4	$+1.0498$	-1.4143	-1.6557	-1.8702

states is approximately 6.0 cm^{-1}. This is much less than the difference between the ground $n = 0$ and first exited $n = 2$ rotational levels of ^{17}O$_2$ which indicates that all the levels shown belong to the $n = 0$ state. The deepest level at -8.2074 cm^{-1} is a result of the coupling of the lowest $j = 1$ level of ^{17}O$_2$ with $L = 0$. The next two sets of three closely packed states result from the coupling of the same monomer level with $L = 2$ and $L = 4$ quantum numbers, respectively. Note that for this system

the correct parity for the S partial-wave is odd.

Table 4.3: Field-free, odd parity levels of $^4\text{He-}^{17}\text{O}_2$, belonging to the $n = 0$ ground state of the even n manifold of $^{17}\text{O}_2$. The rigourously good quantum number J is the total angular-momentum while L is the approximate good quantum number representing the end-over-end angular momentum.

		$^4\text{He-}^{17}\text{O}_2$ (even n)
J	L	Energy(cm^{-1})
0	0	-8.2074
2	2	-6.4367
3	2	-6.3207
1	2	-6.2494
4	4	-2.2218
3	4	-2.2035
5	4	-2.1900

In the presence of a magnetic field each zero-field J level splits into the $2J + 1$ levels labeled by the projection quantum number M_J. Figure 4.15 shows the splitting of some levels of $^4\text{He-}^{16}\text{O}_2$ in a field of 100 G. Unlike the total angular momentum quantum number, M_J remains a rigorously good quantum number. However, for complexes with odd n, J remains a good quantum number up to approximately 1000 G, after which point the levels are strongly mixed. Figures 4.16 to 4.19 show the Zeeman structure of complexes of odd rotational manifold of O_2. We note, for example, that the lowest level of the complexes has a field dependence very similar to the $j = 0$ of O_2 shown on 4.4. Between -1 and -2 cm^{-1} on Fig. 4.17, despite mixing of levels belonging to $j = 0$ and 1, it is possible to discern a pattern similar to the O_2 $j = 1$ Zeeman structure. The $j = 2$ levels of the complex bear a similar resemblance to the monomer levels of the same quantum number.
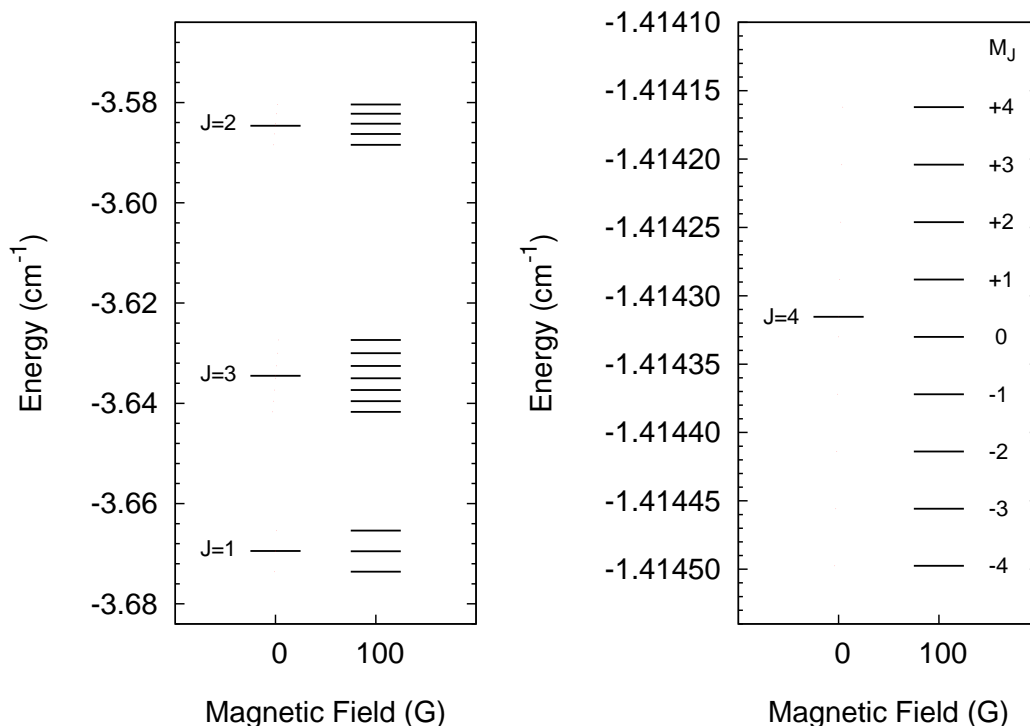
Figure 4.15: The lifting of degeneracy of the levels of ^{4}He-^{16}O$_2$ by a magnetic field. The left-hand panel shows several levels splitting according to their J quantum number. On the right, we have the splitting of a $J = 4$ level into 9 levels labeled by their M_J quantum number.

The magnetic quantum number M_J can be written as the sum of m_j and M_L. As the magnetic moment due to the end-over-end rotation is not included, M_L makes no contribution to the magnetic field dependence of M_J, so that the Zeeman structure is strongly determined by m_j. However, M_L influences the point at which the levels avoided-cross. The similarity in the pattern of the complex and O$_2$ levels points to m_j being an approximately good quantum number even for the complex. The Zeeman structure of ^{4}He-^{17}O$_2$ is shown in Figure 4.20. The first three sets of levels have quantum number $j = 1$. The similarity with the $j = 1$ ground-level of ^{17}O$_2$ is more striking. We note an avoided crossing between $M_J = +1$ levels of the first two sets of levels at about 10000 Gauss. Many of the lines above the bound states are artificial states which should be ignored for the purpose of the discussion at hand.
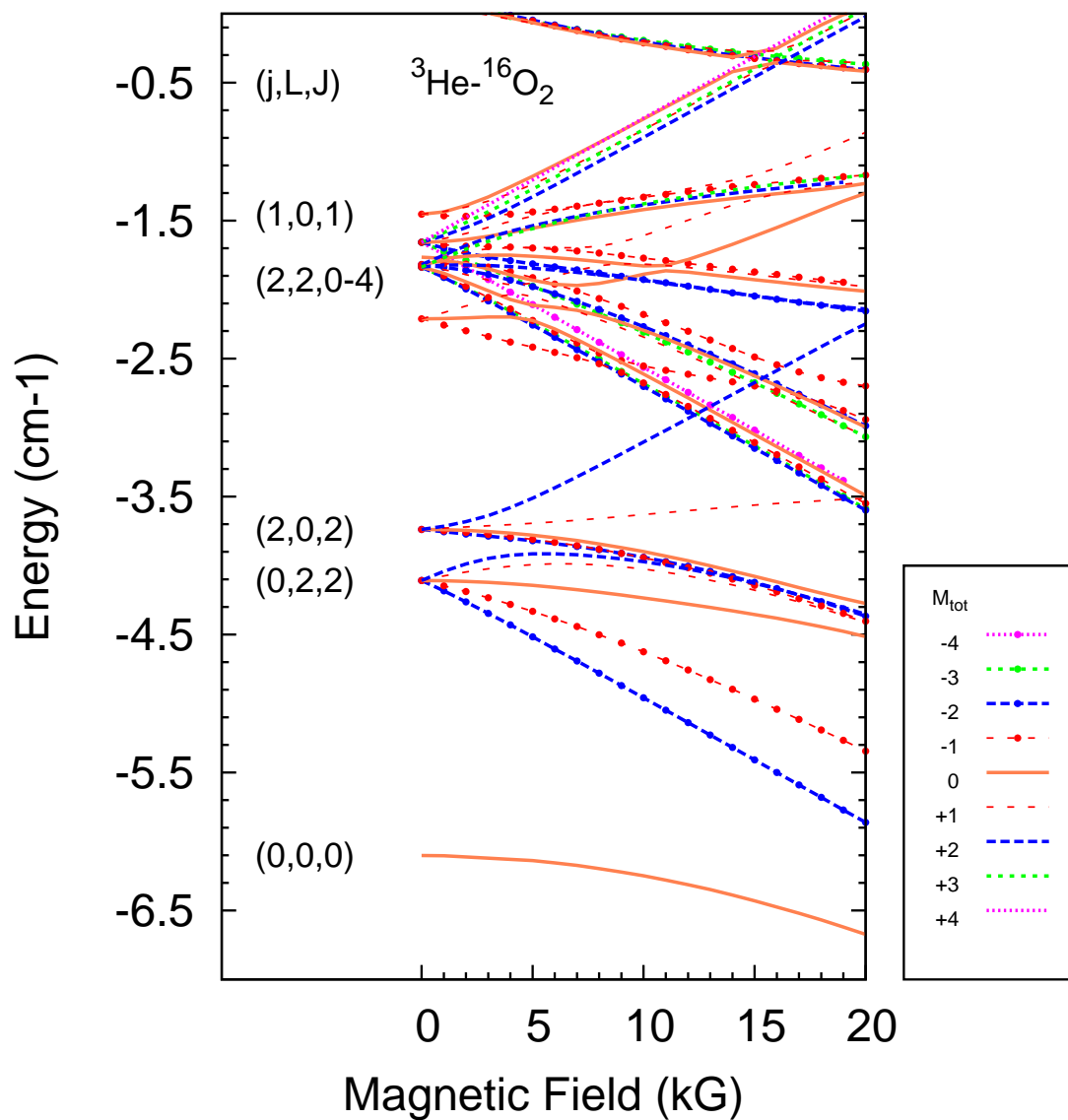
Figure 4.16: The Zeeman structures of the bound states of ^{3}He-^{16}O$_2$. These states correspond to the ground rotational level ($n = 1$) of the ^{16}O$_2$ monomer.
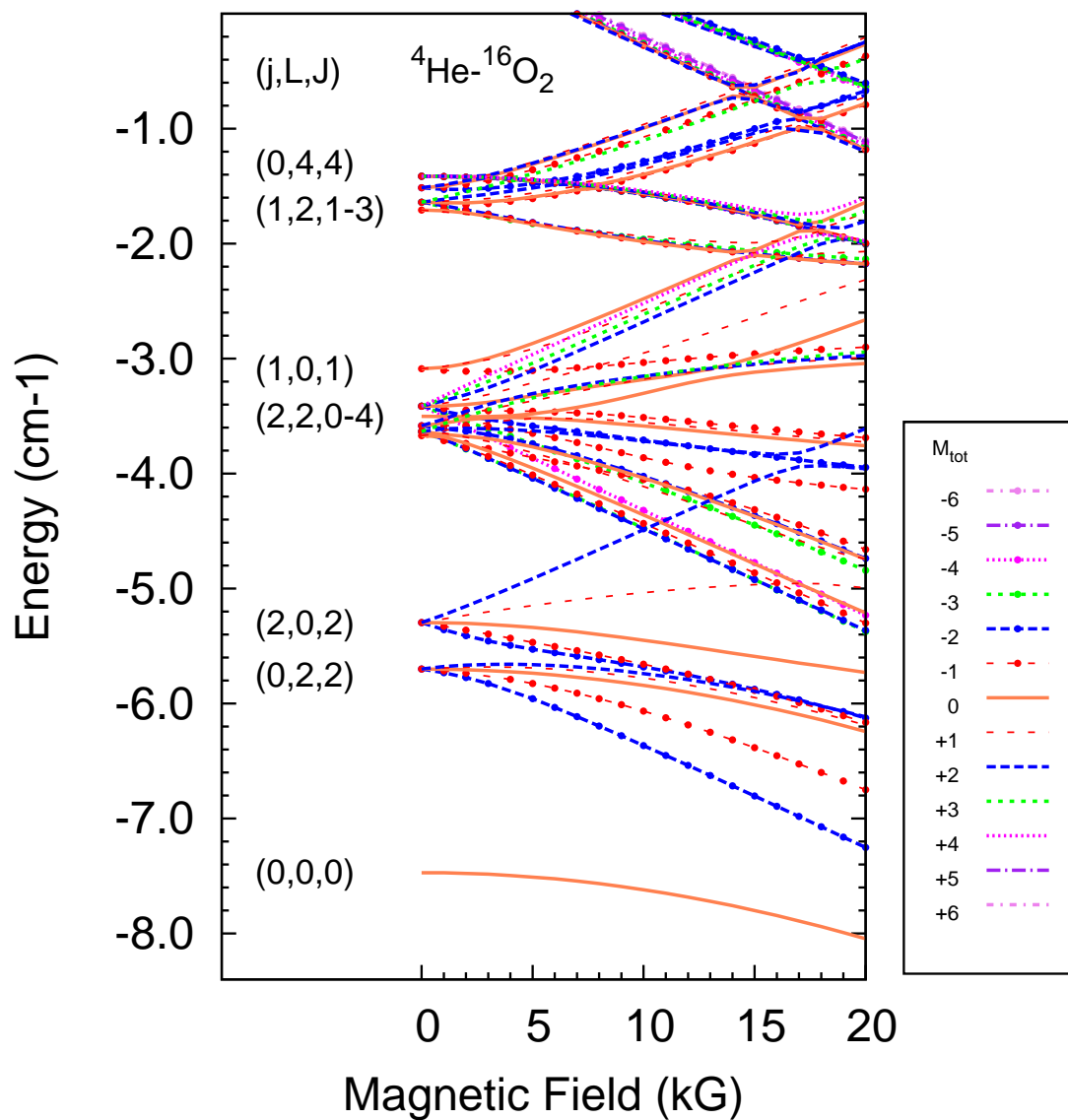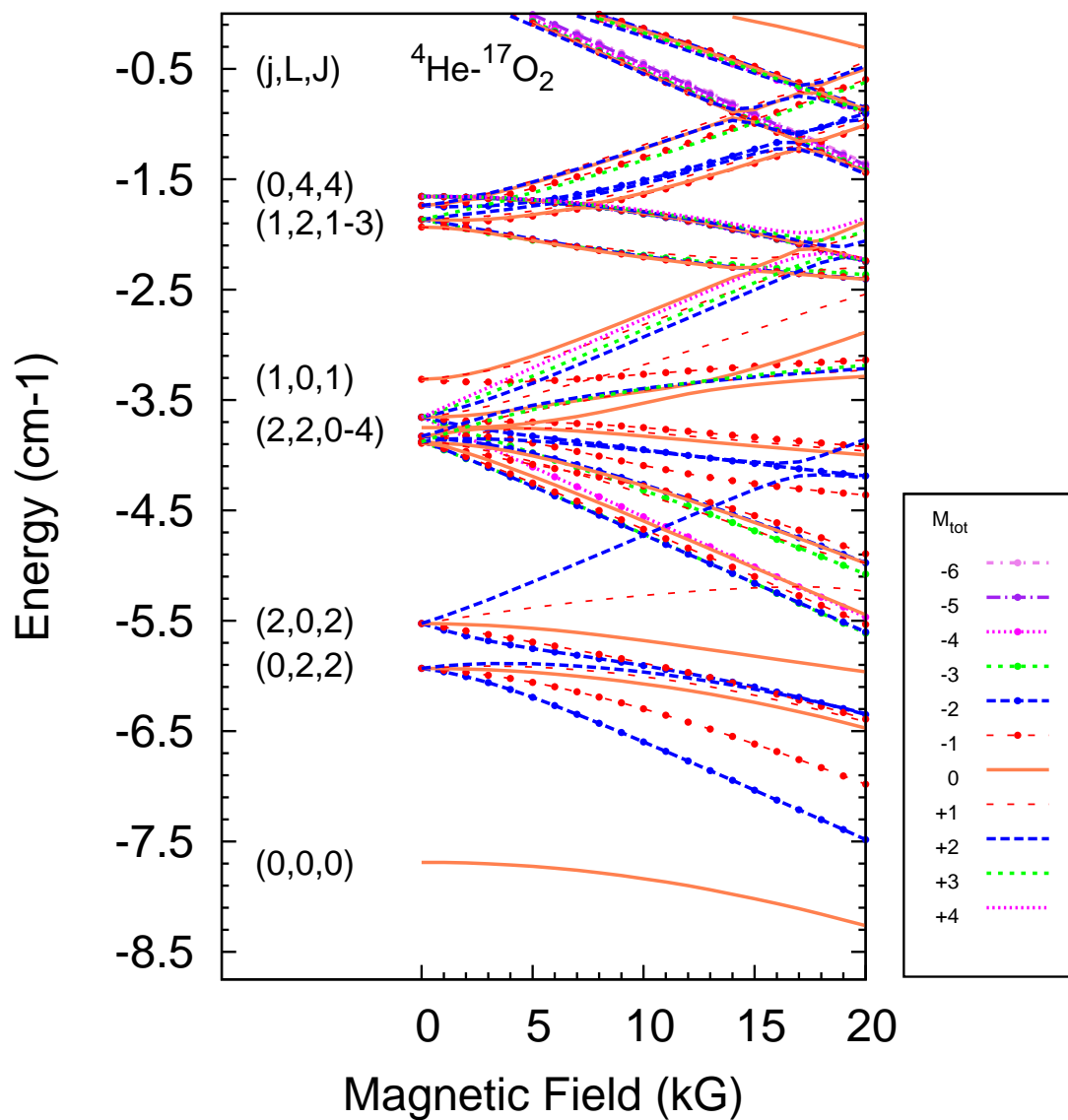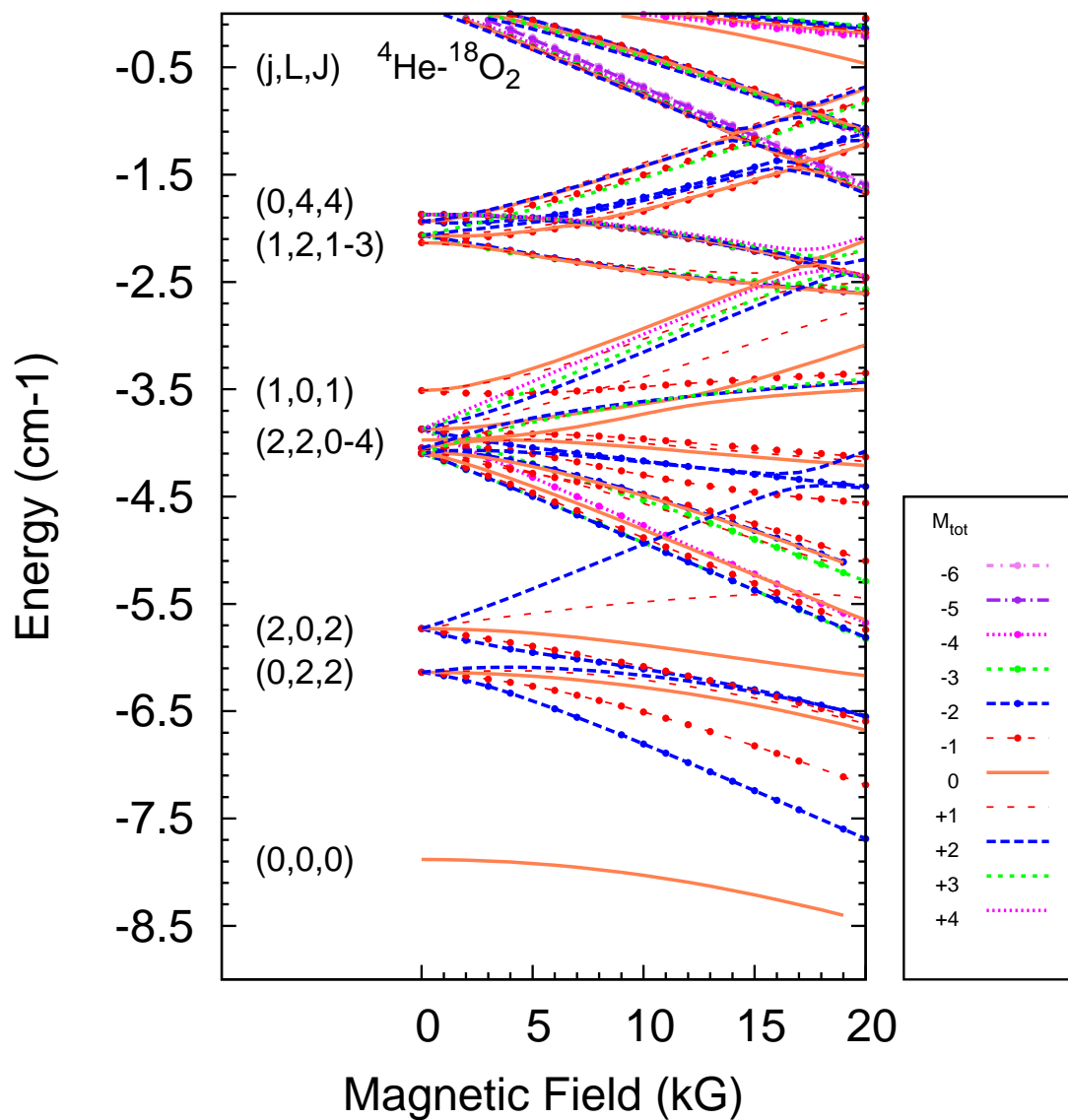
Figure 4.17: The Zeeman structures of the bound states of ^{4}He-^{16}O$_2$. These states correspond to the ground rotational level ($n = 1$) of the ^{16}O$_2$ monomer.

Figure 4.18: The Zeeman structures of the bound states of ^{4}He-^{17}O$_2$. The states correspond to the ground rotational level ($n = 1$) of the odd series of ^{17}O$_2$ monomer.

Figure 4.19: The Zeeman structures of the bound states of ^{4}He-^{18}O$_2$. These states correspond to the ground rotational level ($n = 1$) of ^{18}O$_2$ monomer.

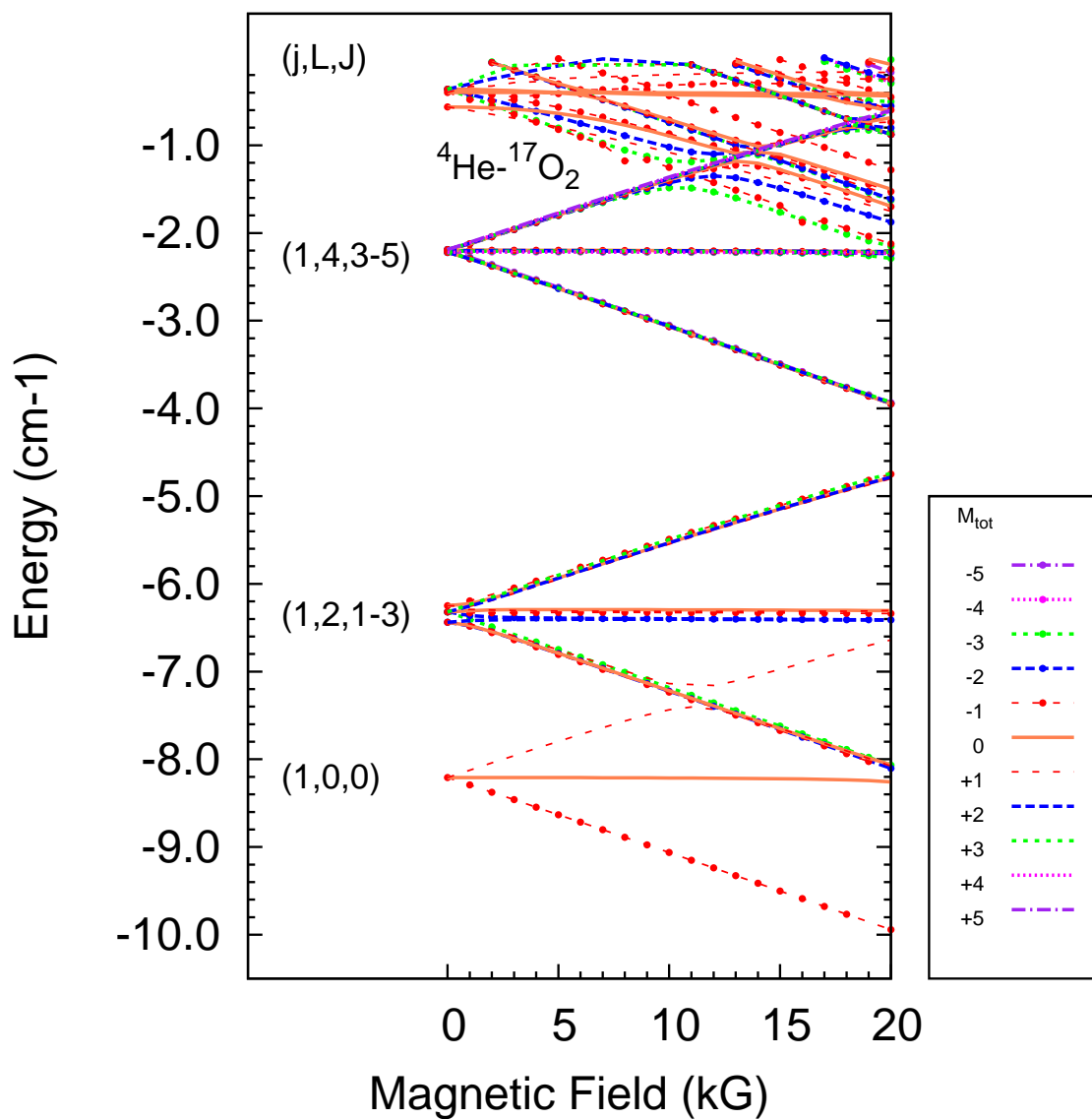Figure 4.20: The Zeeman structures of the bound states of ^{4}He-^{17}O$_2$. These states correspond to the ground rotational level ($n = 0$) of the even series of ^{17}O$_2$ monomer.

Chapter 5

Scattering resonances of He-O$_2$

5.1 Introduction

Like bound states, scattering states in principle extend to $R_{\mathrm{max}} = \infty$. In practice, we must of course limit calculation to some finite range. However, scattering states do not decay to zero at the outer limit and we are required to propagate to significantly larger values of R_{max} to recover scattering properties accurately. In our scattering calculations we found $R_{\mathrm{max}} = 120$ Å to be sufficient. The instability of propagating into the outer classically forbidden region is still an important consideration as the threshold of at least some, and often most, adiabatic surfaces will be higher than the energy of the scattering state. The long-range nature of the incoming wavefunction allows us to use a variable step-size propagator for the range beyond R_{mid}. Varying the step-size ΔR according to the curvature of the wavefunction avoids unnecessarily small steps, saving time and computational resources.

In this chapter we will locate and characterize zero-energy resonances of collisions of ^{3}He and ^{4}He with ^{16}O$_2$. These systems were chosen as representative of the structure of discrete states of He-O$_2$ complexes belonging to the approximate quantum number $n = 1$. Preliminary calculations supported this conclusion. Our group previously studied $n = 0$ collisions of NH (a triplet Sigma molecule like O$_2$) with He. The He-O$_2$ system is more anisotropic, resulting in higher inelastic cross sections. Additionally, the $n = 1$ levels are more directly coupled to each other and to higher

n levels by the potential anisotropy, increasing inelasticity and resonance widths. Because He is assumed to have no internal structure, the levels of molecular oxygen are the collision thresholds. We present low-energy resonances of scattering states incoming in the two lowest thresholds, $m_j = -2$ and $m_j = -1$, of the $j = 2$ level of O_2. This restriction was motivated by our interest in inelastic collisions in the low-energy limit. Scattering calculations were performed using the MOLSCAT [300] package, as modified to include magnetic fields [294], using a decoupled basis set. The potential energy surface was provided by Groenenboom and Struniewicz [292].

5.2 Wigner threshold regime

At long range, the interaction of He with O_2 is dominated by a leading $-C_6/R^6$ term of the interaction potential, and, the centrifugal energy. We can express the interaction in this range as

$$V(R) = -\frac{C_6}{R^6} + \frac{\hbar^2 L(L+1)}{2\mu R^2}. \tag{5.1}$$

We omit the angular dependence here as the anisotropy becomes increasingly less significant with distance. The two terms are opposite in sign, with the attractive dispersion term stronger initially and the repulsive centrifugal term dominating at longer range. This results in a *centrifugal barrier*, with positions and height given by

$$R_{\text{max}} = \left[\frac{6C_6\mu}{\hbar^2 L(L+1)} \right]^{\frac{1}{4}} \tag{5.2}$$

and

$$V_{\text{max}} = 2C_6 \left[\frac{\hbar^2 L(L+1)}{6C_6\mu} \right]^{\frac{3}{2}}, \tag{5.3}$$

respectively. Groenenboom and Struniewicz [292] give a value $9.17\ E_{\text{h}}/a_0^6$ for the C_6 coefficient. This places the lowest even-parity ($L = 2$) barrier of the ^{4}He-^{16}O$_2$ system at $R_{\text{max}} = 8.2637$ Å with a height of 0.3994 K (0.2776 cm^{-1}). For *low* and *ultra-low* collision energies, the centrifugal barriers are insurmountable, and the wavefunction has to tunnel through in order to sample the short range interaction. Tunneling reduces rapidly with energy so that in the zero-energy limit the repulsive centrifugal term dampens all but the S partial wave, which has no centrifugal interaction and

dominates the wavefunction at low energy. However the wavefunction has very long wavelength, washing out the effect of the short range interaction. What matters is the long range character of the potential. The cross sections follow Wigner's threshold laws [71]

$$\sigma_{\text{elas}} \quad \propto \quad E^{2L} \tag{5.4}$$

$$\sigma_{\text{inel}} \quad \propto \quad E^{L-1/2} \tag{5.5}$$

where E is the energy. The positions and heights of the centrifugal barriers corresponding to even-parity thresholds of ^{3}He-^{16}O$_2$ and ^{4}He-^{16}O$_2$, up to $L = 6$, are given in table 5.1.

Table 5.1: The position and height of the centrifugal barriers for $L = 2, 4$, and 6 for ^{3}He-^{16}O$_2$ and ^{4}He-^{16}O$_2$.

	^{3}He-^{16}O$_2$		^{4}He-^{16}O$_2$	
L	$R_{\text{max}}(\text{Å})$	$V_{\text{max}}(\text{cm}^{-1})$	$R_{\text{max}}(\text{Å})$	$V_{\text{max}}(\text{cm}^{-1})$
2	7.7529	0.4070	8.2637	0.2776
4	5.7378	2.4770	6.1158	1.6892
6	4.7664	7.5380	5.0804	5.1405

Figure 5.1 is a plot of calculated total elastic and inelastic cross sections for collisions of ^{4}He with ^{17}O$_2$ for a range of collision energies in a field of 2000 Gauss. The scattering state has $M_J = 0$ symmetry and is incoming in the channel corresponding to the $m_j = 0$ level of the $n = 0$ rotational ground state of ^{17}O$_2$ shown in figure 4.5. This level has $m_s = 0$. The cross sections are of the same order of magnitude with the elastic cross section dominating up to about 0.2 mK, at which point the inelastic cross section takes over. Below about 1 mK, the elastic cross section tends to a constant value, while the inelastic cross section is linear with a gradient of $-1/2$ in the log-scaled graph. We note from the threshold laws 5.5 that this is consistent with an S-wave dominated process for which the elastic cross section at
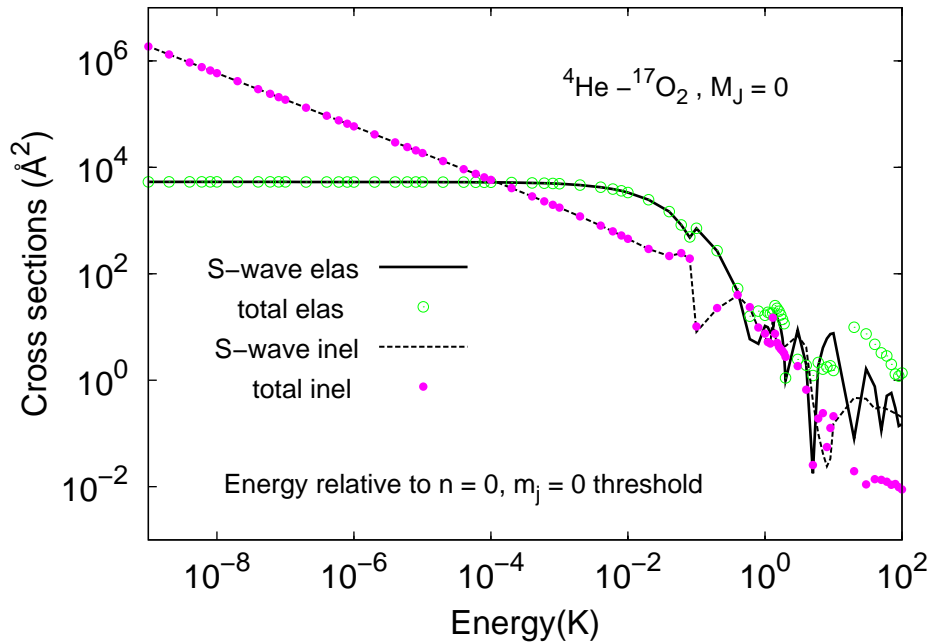
Figure 5.1: Elastic and inelastic cross sections of collisions of ^{4}He with ^{17}O$_2$ in the limit of low energy. The incoming channel belongs to the $(n, j, m_j) = (0, 1, 0)$ threshold of the even rotational manifold of ^{17}O$_2$ and is of $M_J = 0$ symmetry.

low-energy is predicted to be constant and the inelastic cross section to have an $E^{-1/2}$ dependence. This dependence of the inelastic scattering results in a constant, in some systems significant [72], inelastic rate-constant in the low-energy limit. The S-wave elastic and inelastic cross sections are also included in the figure. For most of the energy range, S-wave cross sections practically coincide with the corresponding cross sections, underlining the dominance of the S partial-wave. Figure 5.1 indicates that the threshold laws begin to hold from a few mK. At low energy the only open inelastic channels will correspond to the $m_j = m_s = -1$ threshold. In order to conserve the total symmetry contributions from the partial waves to the total projection must be $+1$. This forbids $L = 0$ partial waves in the outgoing channel requiring all inelastic scattering to take place via tunneling. With the barriers of $L = 2$ and $L = 4$ at 0.3993 K and 2.406 K, respectively, inelastic scattering is dominated by $L = 2$, with little contribution from the $L = 4$ partial wave. The prohibition of some partial-waves in the outgoing channel, coupled with the ability to tune the levels can potentially be exploited to suppress inelastic collisions. This is especially true
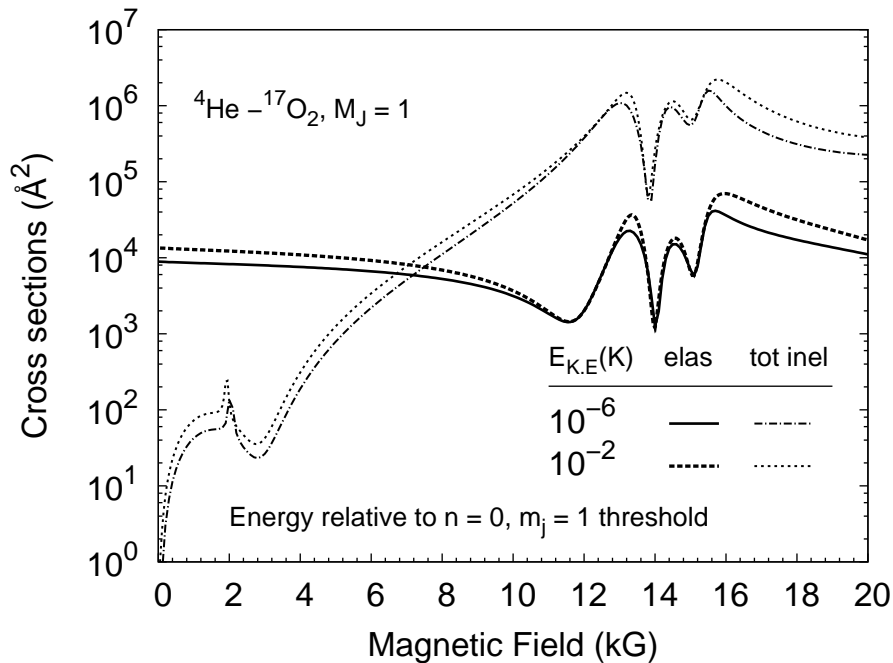
Figure 5.2: Elastic and inelastic cross sections of collisions of ^{4}He with $^{17}O_2$ for collision energies 10 mK and 1 μK. The incoming channel belongs to the trappable $(n, j, m_j) = (0, 1, 1)$ threshold of $^{17}O_2$. The overall symmetry of the scattering state is $M_J = 1$.

for systems with large centrifugal barriers.

The graph in figure 5.2 shows cross sections for collisions with incoming channel belonging to the $m_j = +1$ threshold of the ground state $n = 0$ of $^{17}O_2$. As we can see from figure 4.5 this is a *weak-field-seeking* state and is therefore trappable. The collision energy was held at 1 μK for the whole range of fields. The open channels belong to $m_j = 0$ and $m_j = -1$ thresholds. In both cases the first allowable outgoing partial wave is $L = 2$. Sufficient energy to clear the $L = 2$ centrifugal barrier is available on exit to the lowest threshold at a field of about 1800 Gauss, and on exit to the $m_j = 0$ threshold at a field of approximately 2000 Gauss, which correspond to the peak in the inelastic cross section. The oscillations beginning around 12000 Gauss are close to the value at which sufficient energy is released, on transition to the lowest threshold, to clear the $L = 4$ barrier.
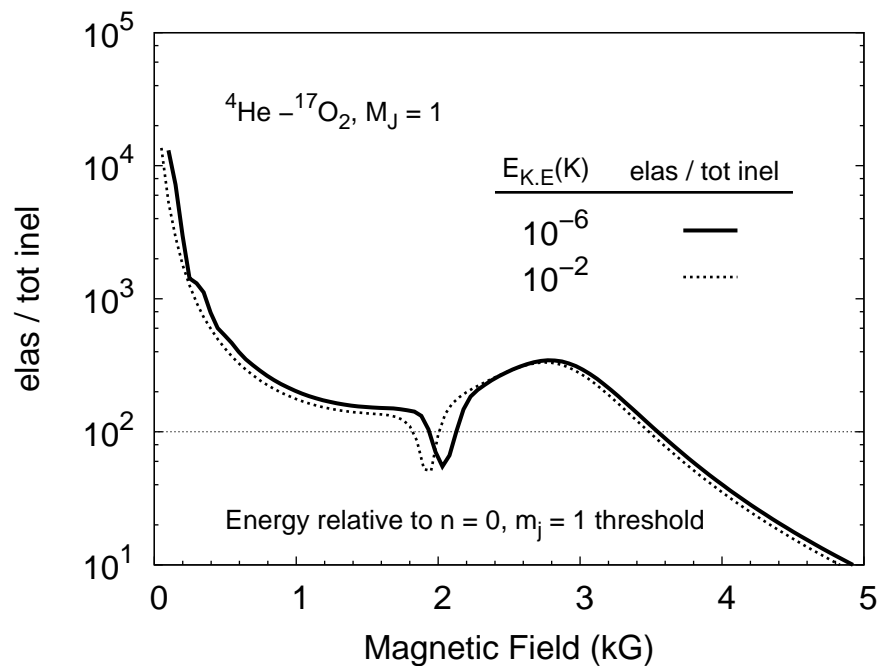
Figure 5.3: The ratio of elastic to inelastic cross section of collisions of ^{4}He with $^{17}O_2$ for collision energies of 10 mK and 1 μK. The incoming channel belongs to the trappable $(n, j, m_j) = (0, 1, 1)$ threshold of $^{17}O_2$.

There is a generally upward trend in the inelastic cross sections as the field increases. This is due to the increase in the energy available for inelastic collisions, resulting in increased tunneling and the opening of channels. We observe also that from zero field up to about 7000 Gauss the inelastic cross sections are lower than the elastic cross sections. Figure 5.3 shows that for fields up to about 1800 Gauss, which correspond to a trap depth of 0.2 K, the elastic cross sections are at least two orders of magnitude higher. This is also the case for a wide region between 2200 Gauss and 3600 Gauss. At its highest, the ratio of elastic to inelastic cross section is about 10^4 for the first 100 Gauss and about 10^3 for the second 100 Gauss. A 200 Gauss change in field would correspond to a trap-depth of about 20 mK. The two temperatures for which calculations were performed were chosen so as to sample the *cold* and *ultra-cold* regions. We observe that despite the wide range of between the two values, the cross sections, and thus their ratios, are very similar.

We have seen that all information on the scattering processes is stored in the

scattering or S-matrix. For an incoming channel i, the elastic cross section σ_{el} is given by

$$\sigma_{\text{el}} = \frac{\pi}{k^2}|1 - S_{ii}|^2 \tag{5.6}$$

and the total inelastic cross section by

$$\sigma_{\text{inel}}^{\text{tot}} = \frac{\pi}{k^2}\{1 - |S_{ii}|^2\}. \tag{5.7}$$

The diagonal element S_{ii} can be written as

$$S_{ii} = e^{2i\delta_i}, \tag{5.8}$$

where δ_i is the phase-shift. The S-matrix is unitary, imposing the condition $|S_{ii}| \leq 1$, which requires the phase-shift to be generally complex with a non-negative imaginary part [301].

In the Wigner regime the phase-shift is proportional to the wavevector k and tends to zero with the reducing energy. The scattering length $a(k)$, defined by

$$a(k) = \lim_{k \to 0} -\frac{\tan(\delta_0(k))}{k} \tag{5.9}$$

where 0 denotes the incoming channel, is a parameter that characterizes the scattering process. The scattering length is usually a finite quantity and can be written as $a(k) = \alpha - i\beta$ [11, 180] where α and β are real quantities. The elastic and total inelastic cross sections can then be written in terms of α and β exactly as [214]

$$\sigma_{\text{el}} = \frac{4\pi|a|^2}{1 + k_0^2|a|^2 + 2k_0\beta} \tag{5.10}$$

and

$$\sigma_{\text{inel}}^{\text{tot}} = \frac{4\pi\beta}{k_0(1 + k_0^2|a|^2 + 2k_0\beta)}. \tag{5.11}$$

In the zero-energy limit these equations give $\sigma_{\text{el}} = 4\pi|a|^2$ and $\sigma_{\text{inel}}^{\text{tot}} = 4\pi\beta/k_0$, in consistence with Wigner's threshold laws [71].

5.3 Quasi-bound states and resonances

The term resonance is sometimes used to refer to a bound state embedded in a continuum. These localized states are above the lowest threshold and are there-

fore quasi-bound. Elastic and inelastic cross sections are generally slowly varying functions of energy, however, when traversing a quasi-bound level they vary quite dramatically. Resonance is at other times used to describe this dramatic change, which is how we will use the term from hereon. Regardless of how the term is used, locating resonances involves the determination of the position of quasi-bound levels. In the low-energy limit we can write the scattering amplitude, $f(k)$, of systems with long-range interactions V^{-n} where $n \geq 4$ as

$$f(k) = \frac{1}{g(k) - ik}. \tag{5.12}$$

The function $g(k)$ is an even and generally complex function of the wavenumber k. Singularities in $f(k)$ correspond to bound and quasi-bound states of the system and can be determined by the condition $g(k) = ik$. We can expand $g(k)$ as

$$g(k_0) = g_0 + g_2 k_0^2 + O(k_0^4) \tag{5.13}$$

where $g_0 = -1/a$, with a the scattering length and $g_2 = r_0/2$. The quantity r_0 is the effective range [302] of the interaction. Taking only the leading term of 5.13 and equating it to ik we get an estimate of the energy, E_b, of the least-bound state as

$$E_b = -\frac{\hbar^2}{2\mu a^2} \tag{5.14}$$

where μ is the reduced mass of the complex. If there is a discrete state just below threshold the interaction is overall repulsive, the phase-shift is negative, and the scattering length is large and positive. For a bound state just above threshold the scattering length is large and negative, indicating an overall attractive interaction. A more accurate approximation of E_b can be obtained by taking higher-order terms in the expansion of $f(k)$. This will also allow estimation of other discrete states.

As the scattering state crosses the discrete state the eigenphase sum [303, 304], which is the sum of the phases of the eigenvalues of the S-matrix, changes by π. The eigenphases, and thus their sum, are real unlike the phase-shifts. The eigenphase sum follows a Breit-Wigner form

$$\Sigma(E) = \Sigma_{\mathrm{bg}} + \arctan\left[\frac{\Gamma_E}{2(E_{\mathrm{res}} - E)}\right] \tag{5.15}$$

across resonance. The first term, Σ_{bg}, is a slowly varying background, while the second is a rapidly changing resonant term. The individual elements of the S-matrix trace a circle on the complex plane across resonance. The diagonal element of the incoming channel can be written

$$S_{00} = S_{\text{bg},00} + \frac{ig_{E0}^2}{E - E_{\text{res}} + i\Gamma_E/2} \tag{5.16}$$

as a function of energy. The Γ_E is the width of the resonance with units of energy. The quantity g_{E0} is complex with the radius r_0 of the circle given by $r_0 = |g_{E0}^2|/\Gamma_E$. The quantity $|g_{E0}^2|$, usually denoted simply by Γ_{E0}, is the *partial width* of channel 0.

5.3.1   Artificial states

We have established the central role of discrete states in collision resonances. Quasi-bound states are localized, and, although less accurately than true bound states, can be located by applying bound-state boundary conditions on the continuum. However, box-quantization of the continuum converts some of the non-localized scattering states into artificial quasi-bound states. It is not possible to avoid artificial states as they result directly from the boundary conditions required to locate the discrete states. Fortunately artificial levels are strongly dependent on the boundary points. For energies well above a given threshold, where the interaction potential can be ignored, artificial levels supported by an adiabatic surface of that threshold have a $1/(R_{\text{max}} - R_{\text{min}})^2$ dependence. For $R_{\text{max}} \gg R_{\text{min}}$, artificial states have effectively a $1/R_{\text{max}}^2$ dependence.

In figure 5.4 we see the relaxation of a large number of artificial states as the outer boundary point R_{max} is increased. The levels flatten off as they approach the lowest threshold and do not cross it. There are three true quasi-bound levels between 0.0 and 0.25 cm^{-1}. The artificial states do not cross this set of levels but do cross a quasi-bound state at about 1.05 cm^{-1}. A close-up of this crossing is depicted by figure 5.5. The artificial states mix and avoided-cross with the quasi-bound level, reappearing below it at higher R_{max}. A problem arises when an artificial states lies close to a real state for a particular R_{max} used to locate quasi-bound states. In such
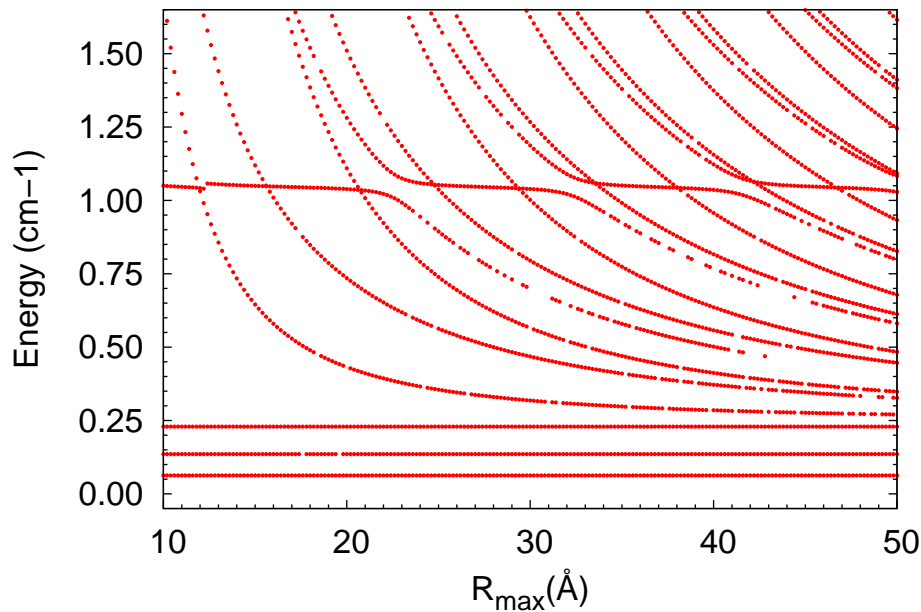
Figure 5.4: Artificial and real quasi-bound states of ^{3}He-^{16}O$_2$. The artificial states relax as R_{max} is increased, avoided-crossing the unchanging quasi-bound levels on their way down.

a case, the real state can be strongly perturbed. To avoid this calculations were performed for a range of R_{max}, which allowed not only the identification of artificial states, but also the best R_{max} values to use for accurate determination of quasi-bound states. In figure 5.5 some artificial states avoid the quasi-bound level more strongly. This is because like bound states, quasi-bound states, artificial or not, overlap strongly with a single threshold. Consequently, artificial states supported by the same threshold as the quasi-bound state are more strongly coupled to it. This causes a stronger avoided-crossing. The crossings are genuine indicators of the degree of coupling of the discrete states with the continua. This has a direct bearing of the width of resonance.

The density of artificial states is highest near thresholds, but, we have been able to find suitable R_{max} values to calculate the energy of quasi-bound states of our complexes. The challenge will be greater for heavier systems for which the density of artificial states is higher.
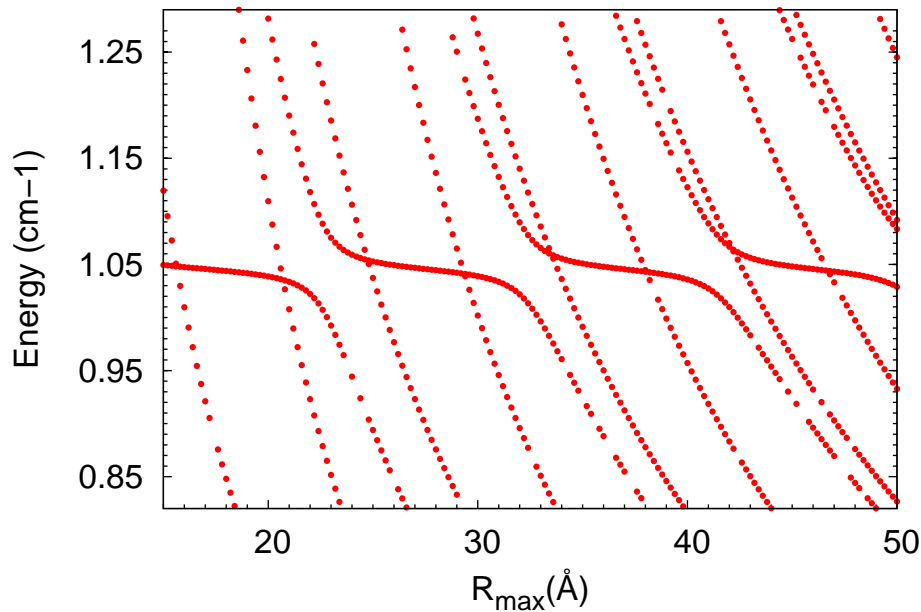
Figure 5.5: A close-up of artificial states crossing a quasi-bound state of ^{3}He-^{16}O$_2$.

5.3.2 Quasi-bound levels

Even-parity quasi-bound levels below 3 cm^{-1} at zero field of ^{3}He-^{16}O$_2$ and ^{4}He-^{16}O$_2$, with all artificial states removed, are listed in table 5.2. The j, L and total angular momentum quantum number J of the levels are shown. We observe that the quasi-bound levels are an extension of the structure of bound states discussed in the previous chapter. We saw in the previous chapter that the least-bound state of ^{3}He-^{16}O$_2$ belongs to $L = 0$ of the $j = 1$ threshold. The first three quasi-bound states of the same complex belong to the first excited end-over-end rotational level, $L = 2$, of the same threshold. In continuation of the bound-state series of the $j = 0$ and 2 levels, which ended with levels of $L = 2$, the remaining quasi-bound states result from coupling of the same monomer levels to the next allowed end-over-end excitation, $L = 4$. In the case of ^{4}He-^{16}O$_2$ we saw that the highest bound states belong to $L = 2$ of the $j = 2$ threshold. Looking at table 5.2 we observe that the first five quasi-bound states of this complex belong to $L = 4$ of the same threshold. The rest of the quasi-bound states are also $L = 4$ levels but belong to the higher $j = 1$ monomer level. The maximum value of the total angular momentum for the range of energy considered is $J = 6$. The first few levels of both systems are shown in

Table 5.2: Field-free, even-parity, quasi-bound levels of ^{3}He-^{16}O$_2$ and ^{4}He-^{16}O$_2$. The first and second columns are the approximately good quantum numbers j and L, respectively. The total angular momentum quantum number J, which is a rigorously good quantum number, is indicated by a separate column for each system. The energies are given relative to the lowest dissociation channel.

		^{3}He-^{16}O$_2$		^{4}He-^{16}O$_2$	
j	L	Energy(cm^{-1})	J	Energy(cm^{-1})	J
1	2	0.0628	1	——-	-
1	2	0.1355	3	——-	-
1	2	0.2289	2	——-	-
0	4	1.0498	4	——-	-
2	4	3.0120	2	0.5543	4
2	4	3.0988	4	0.5808	2
2	4	3.1584	6	0.6775	5
2	4	3.1619	3	0.7106	3
2	4	3.7409	5	0.7171	6
1	4	——	-	2.4824	3
1	4	——	-	2.5326	4
1	4	——	-	2.5531	5

figures 5.6 and 5.7. They are depicted in adiabats corresponding to their parentage.

The energies of quasi-bound states are the collision energies for which we can expect resonances. This usually refers to energies above the complex threshold. For resonances at zero collision energy we would require the quasi-bound state to have the same energy as the threshold. In general this does not happen naturally.

Figure 5.6: The first few quasi-bound states of ^{3}He-^{16}O$_2$ in zero field. The adiabatic curves and the inset table indicate the parentage of the levels.
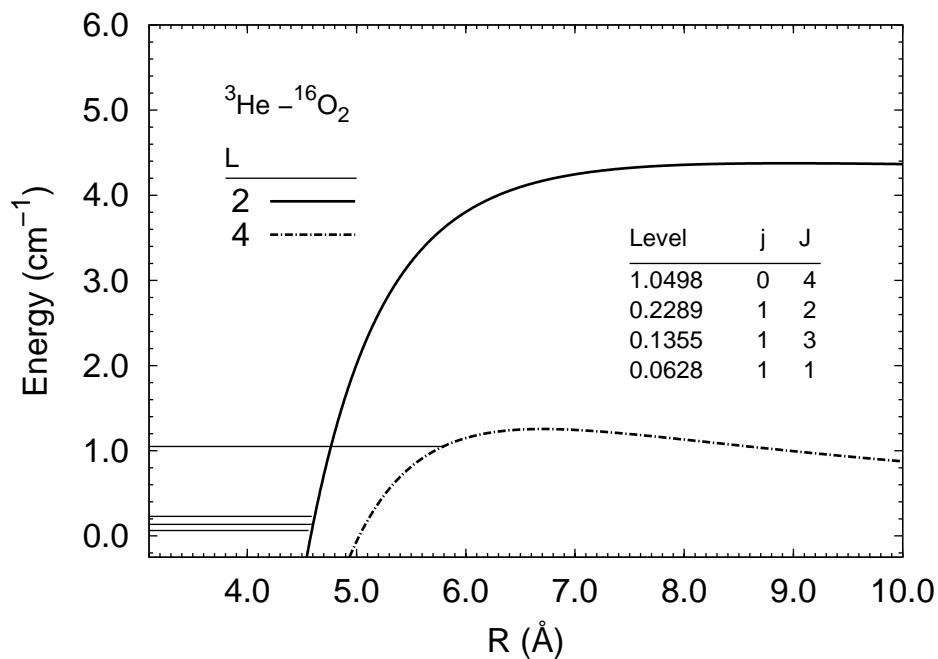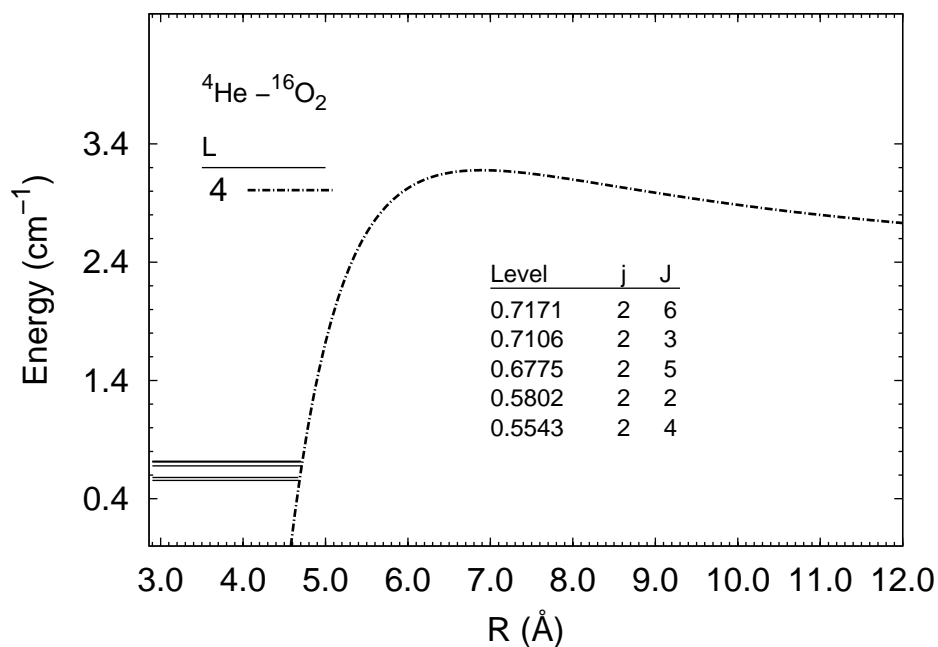

Figure 5.7: The first few quasi-bound states of ^{4}He-^{16}O$_2$ in zero field. The adiabatic curves and the inset table indicate the parentage of the levels.

However, when the system has magnetic or electrical moments, fields can be used to tune both thresholds and discrete states, causing them to cross. In this way we can use fields to tune zero-energy resonances predictably. Fields split states, resulting in an increased number of levels, but the reduction in symmetry also imposes greater restrictions on their interaction. The Zeeman structure of even-parity quasi-bound levels of ^{3}He-^{16}O$_2$ and ^{4}He-^{16}O$_2$ are shown in figure 5.9 and 5.11. The magnetic quantum numbers range from $M_J = +6$ to $M_J = -6$. The levels of ^{16}O$_2$ are included for comparison. We note, as was the case for bound states, the similarity of the structure of the quasi-bound states with the threshold levels. For example, in figure 5.9 the similarity of the structure of the set of quasi-bound states of ^{3}He-^{16}O$_2$ labeled by $(j, L, J) = (2, 4, 2 - 6)$ with that of the $j = 2$ threshold shown just below is striking. This is due to the fact that the interaction potential only weakly couples different channels, leaving j and m_j as approximately good quantum numbers.

Resonances do not occur at every crossing of threshold and discrete state. The incoming S-wave at the relevant threshold must have the same symmetry as the discrete state. In a field, this means the same projection quantum number M_J and of course the same parity. For an S-wave $M_L = 0$, which means that the projection quantum number $M_J = m_j$. Thus, for a threshold belonging to a given m_j, zero-energy resonances occur at crossings with quasi-bound states belonging to $M_J = m_j$. Figures 5.8 and 5.10 show quasi-bound states of ^{3}He-^{16}O$_2$ and ^{4}He-^{16}O$_2$ belonging to $M_J = \pm 1, \pm 2$. The levels are plotted according to their projection quantum number, with circles indicating the predicted positions of zero-energy resonances.

5.4 Resonances of ^{3}He-^{16}O$_2$ and ^{4}He-^{16}O$_2$

5.4.1 Single open channel

In the energy domain, as collision energy is increased, the scattering state crosses the resonance state from below. Magnetic tuning allows for resonances in which the scattering state crosses the discrete state from above, even with increasing field.

Figure 5.8: Quasi-bound levels of ^{3}He-^{16}O$_2$ of $M_J = \pm 1, \pm 2$ symmetry. Each graph shows levels of unique total angular momentum projection M_J (in dotted colored lines) and the threshold levels (in a solid black line). The circles indicate positions of zero-energy resonances.

Figure 5.9: The Zeeman structure of the quasi-bound states of ^{3}He-^{16}O$_2$. For the energy range depicted, the highest projection quantum number is $M_J = +6$. The solid black lines show the levels of ^{16}O$_2$ which are the collision threshold levels of the complex. Only quasi-bound states with the same symmetry as the ^{16}O$_2$ level can result in zero-energy S-wave resonances.
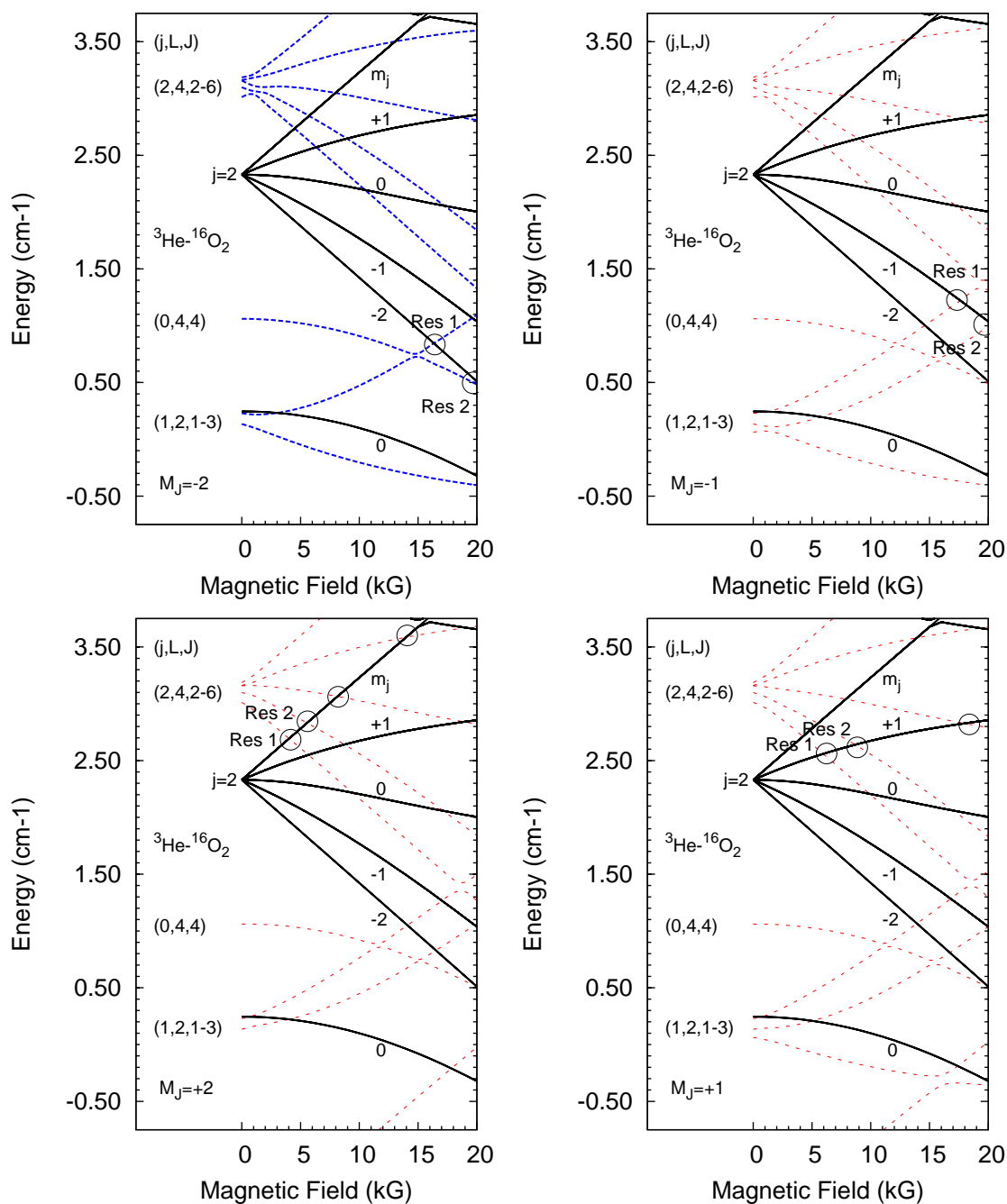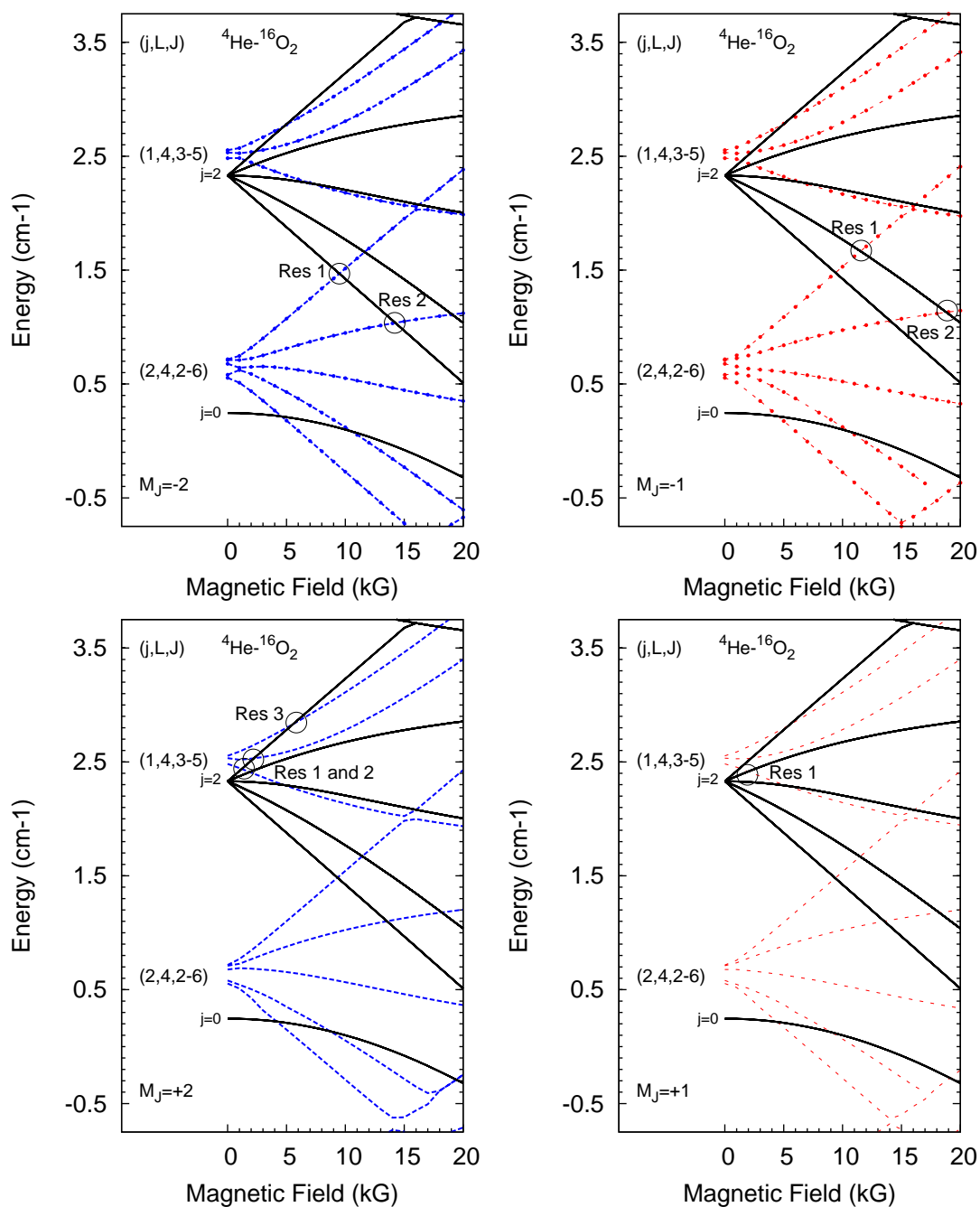
Figure 5.10: Quasi-bound levels of ^{4}He-^{16}O$_2$ of $M_J = \pm 1, \pm 2$ symmetry. Each graph shows levels of unique total angular momentum projection M_J (in dotted colored lines) and the threshold levels (in a solid black line). The circles indicate positions of zero-energy resonances.
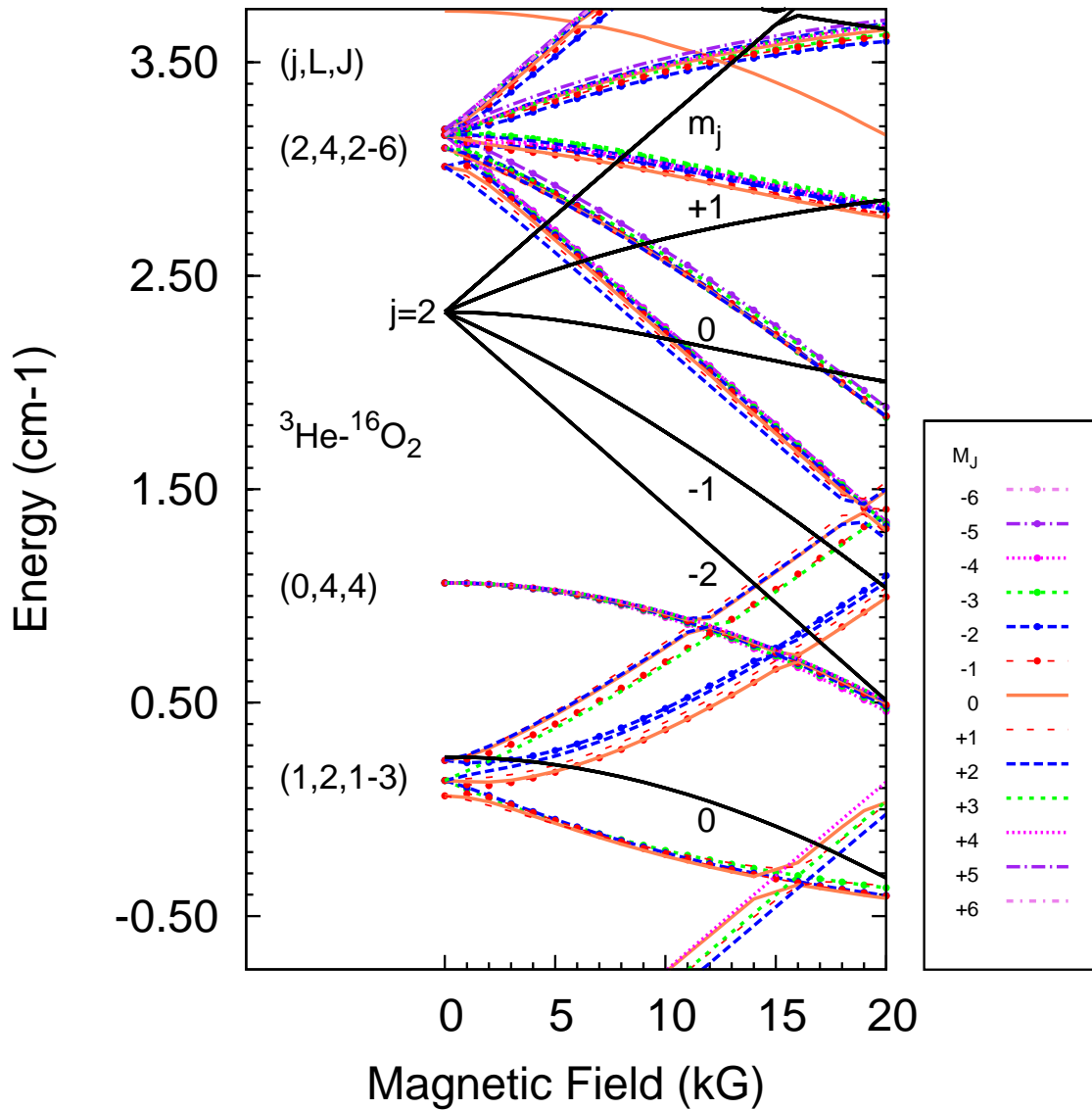
Figure 5.11: The Zeeman structure of the quasi-bound states of ^{4}He-^{16}O$_2$ with M_J between -6 and $+6$. The solid black lines show the levels of ^{16}O$_2$ which are the collision threshold levels of the complex. Only quasi-bound states with the same symmetry as the ^{16}O$_2$ level can result in zero-energy S-wave resonances.
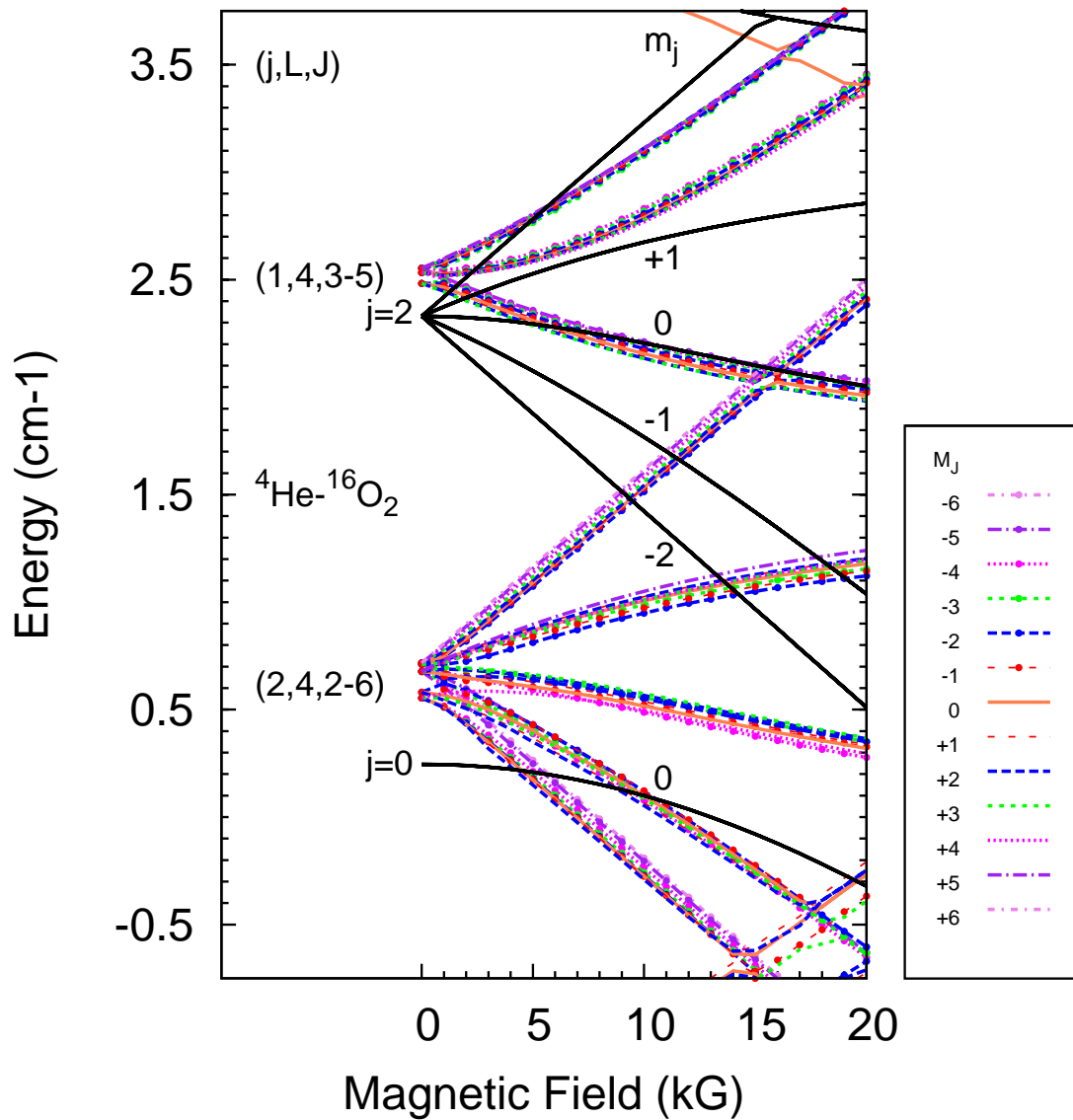
When inelastic scattering is impossible, and only S-wave scattering is present, the S-matrix is 1×1 and the eigenphase sum reduces to the phase-shift $\delta_0(k)$. Across a magnetically tuned resonance the phase-shift can be expressed as [305]

$$\delta(B) = \delta_{\text{bg}} + \arctan\left[\frac{\Gamma_B}{2(B_{\text{res}} - B)}\right]. \tag{5.17}$$

If the collision energy is E, the discrete level $E_{\text{res}}(B)$, and the energy of the threshold of the incoming channel $E_{\text{thresh}}(B)$, then B_{res} is the field B for which $E_{\text{res}}(B) = E + E_{\text{thresh}}(B)$. Such a field exists if the threshold and discrete states cross. The width, Γ_B, is the field-width across which the phase-shift changes by π. It is related to the usual width in the energy domain, Γ_E, by $\Gamma_B = \Gamma_E/\Delta\mu$ [305] where

$$\Delta\mu = \frac{d}{dB}(E_{\text{res}} - E_{\text{thresh}}) \tag{5.18}$$

is the difference in the magnetic moments of the threshold and discrete state. This means that Γ_B is signed according to whether the discrete state crosses resonance from above or below. The phase-shift, as described by equation 5.17, completely characterizes the resonance.

Figure 5.12 shows the predicted zero-resonance positions of both systems for $M_J = 0$. For low-energy scattering, incoming channels corresponding to the lowest threshold result in only elastic cross scattering. This is certainly the case for the energies we use. The phase-shifts for the resonances marked Res 3 on the left panel of figure 5.12 and Res 1 on the right panel of the same figure are shown in figure 5.13. We note the sudden change by π as the scattering state crosses the bound state. In the case of Res 3 we note that the discrete state crosses threshold from below, resulting in a *reduction* in the phase-shift while that of Res 1 on the right *increases* as the discrete state crosses from above.

The scattering length $a(k)$, which describes the effective interaction in the low-temperature limit, has a pole at resonance as the phase-shift is an odd multiple of
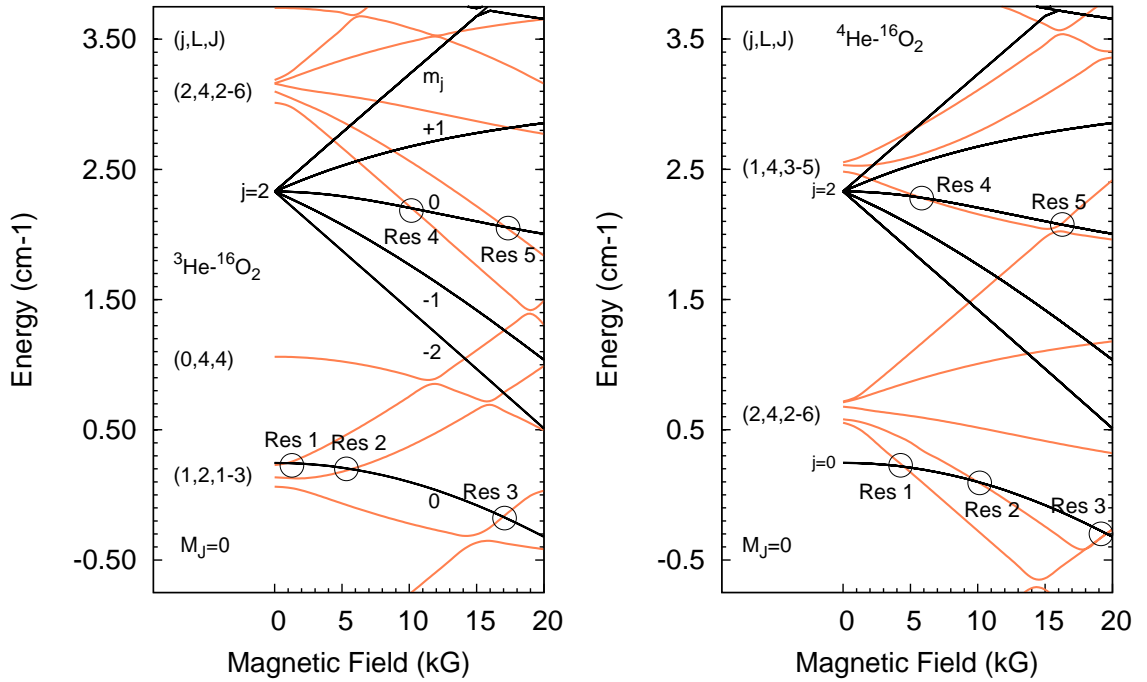
Figure 5.12: Quasi-bound states of $M_J = 0$ symmetry of ^{3}He-^{16}O$_2$ and ^{4}He-^{16}O$_2$ with the S-wave resonance positions indicated by circles. Ultra-low energy collisions incoming at the lowest $m_j = 0$ threshold can only result in elastic scattering.
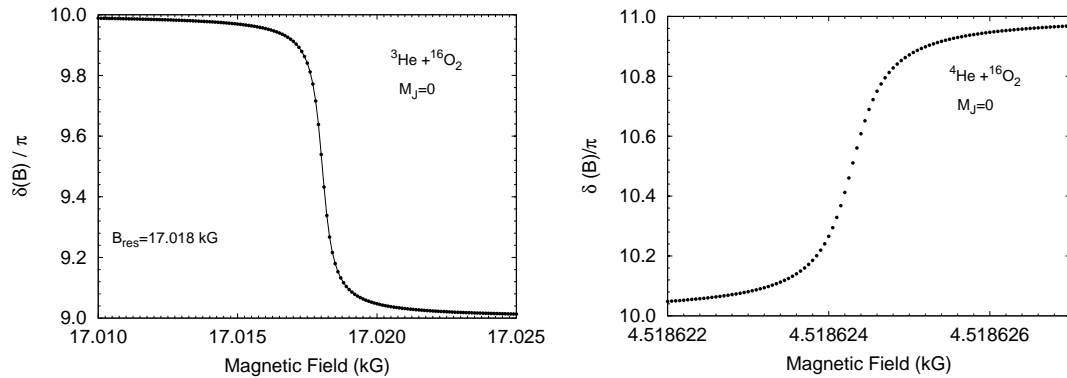
Figure 5.13: The left panel shows the phase-shift across resonance Res 3 indicated in the left panel of figure 5.12 where the discrete state crosses threshold from below. The phase-shift shows a sudden *reduction* by π. The right panel corresponds to resonance Res 1 of ^{4}He-^{16}O$_2$ in figure 5.12. The discrete state crosses threshold from above, resulting in a sudden *increase* in the phase-shift by π.

Figure 5.14: The scattering length across Res 3 of ^{3}He-^{16}O$_2$ depicted in figure 5.12.

π, and changes sign across it. Its behavior is described by [142, 305]

$$a(B) = a_{\text{bg}} \left[1 - \frac{\Delta_B}{B - B_{\text{res}}} \right], \tag{5.19}$$

where Δ_B is related to the resonance width by $\Gamma_B = -2a_{\text{bg}}k\Delta_B$. In the limit of low energy, the quantity Δ_B is co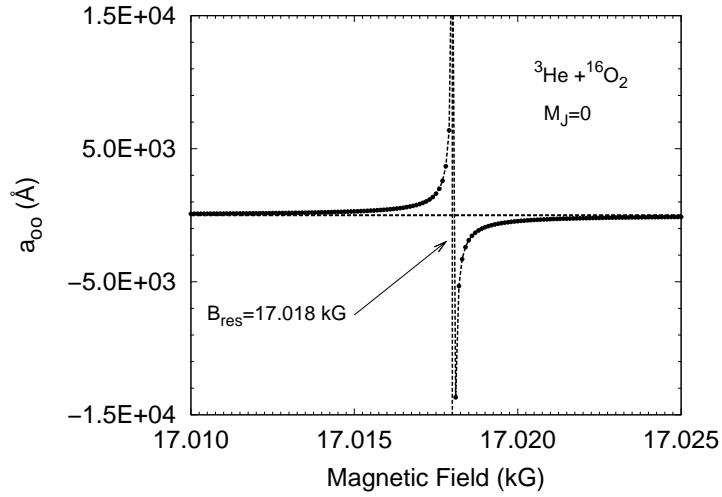nstant. As discussed earlier a negative value of the scattering length corresponds to an overall attractive interaction, while a positive scattering length corresponds to an overall repulsive interaction. Tuning across resonance thus effectively changes the strength and nature of interaction. In the case of elastic scattering the pole means that we can tune the interactions to arbitrary strength. In figure 5.14 is depicted the scattering length of the Res 3. Note that the scattering length starts off above the axis when the discrete state is below threshold, reaching large positive values before reappearing below the axis at large negative values as the discrete state crosses and is just above threshold. The pole, which corresponds to the discrete state and threshold coinciding in energy, is a mathematical point and the calculated values are on either side of this point.

We can obtain the expression for the elastic cross section in the absence of inelastic scattering from equation 5.10 by setting β to zero to get

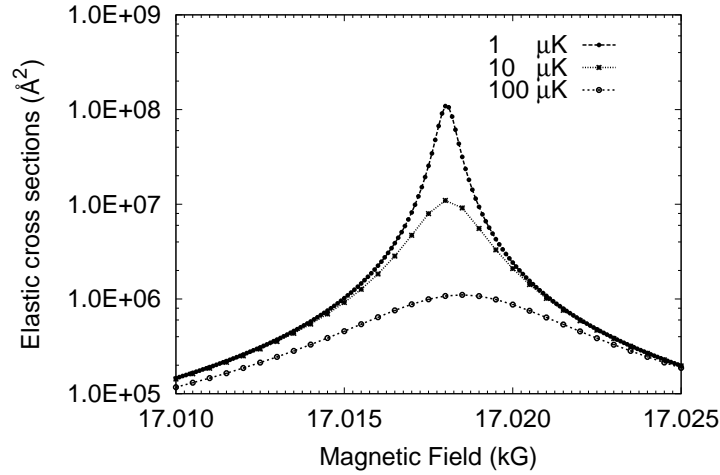$$\sigma_{el}(k) = \frac{4\pi a^2}{1 + k^2 a^2}. \tag{5.20}$$

Figure 5.15: The elastic cross section across Res 3, $M_J = 0$, of ^{3}He-^{16}O$_2$ for collision energies of 1 μK, 10 μK, and 100 μK.

We drop the magnitude sign on the scattering length to emphasize that it is real for pure elastic scattering. The cross section, $\sigma_{\mathrm{el}}(k)$, has a maximum value $4\pi/k^2$ at resonance. Figure 5.15 shows the cross section across Res 3 for collision energies of 1μK, 10μK and 100μK. The peaks of the graphs agree well with maximum values $1.1 \times 10^{+8}$ Å^2, $1.1 \times 10^{+7}$ Å^2 and $1.1 \times 10^{+6}$ Å^2 predicted by the formula.

With a real phase-shift, δ_0, the magnitude $|S_{00}| = |e^{2i\delta_0}| = 1$. Across resonance the element S_{00} traces a unit circle on the complex plane as shown on the right hand panel of figure 5.17. The figure portrays two circles indicated by solid and empty circular points correspond to 1 μK and 4 μK collision energies. We note that both circles are of unit radius. The S-matrix circle is unaffected by the collision energy and will always pass through $S_{00} = (1, 0)$ corresponding to the pole in $a(B)$.

5.4.2 Multiple open channels

When several channels are open inelastic scattering is possible and $|S_{00}| < 1$ or $\beta < 0$. Across a resonance S_{00} still traces a circle. Figure 5.16 is a schematic of S_{00} across a resonance in the case of multiple open channels. The larger circle, which is of unit radius, is the boundary imposed on S_{00} by unitarity. Starting from a background
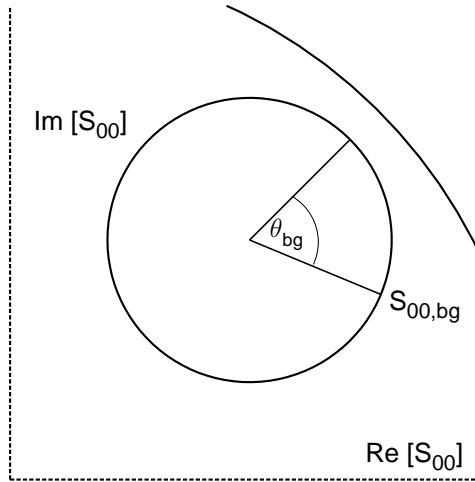
Figure 5.16: Schematic figure showing the S-matrix element, S_{00}, corresponding to the S-wave in the incoming channel across a resonance, in the presence of inelastic scattering. The outer arc is part of the unit circle that unitarity imposes as an outer limiting boundary for all S-matrix elements.

value $S_{00,bg}$ away from resonance, S_{00} is tuned around the smaller circle, completing its journey back at the starting point. The background $S_{00,bg}$ is characterized by an angle θ_{bg} measured from the point of least background inelastic cross section as shown by figure 5.16. This angle allows us to identify several qualitative cross section profiles.

From equations 5.6 and 5.7 we can conclude that the elastic cross section is proportional to the distance of S_{00} from the point $(1,0)$ on the real axis. Similarly the inelastic cross section is proportional to the shortest distance to the unit circle. In the special case where $\theta_{bg} = 0°$ the background inelastic cross section ($\sigma_{\text{inel,bg}}^{\text{tot}}$) is also the minimum value of $\sigma_{\text{inel}}^{\text{tot}}(B)$. Across resonance the inelastic cross section increases to a maximum value before dropping back to the background value. The profile of the inelastic cross section is symmetric about the resonant field B_{res}. The initial behavior of the elastic cross section depends on the sense of circulation, which is determined by the sign of $\Delta\mu$ as defined by equation 5.18. If we assume a clockwise sense, then, as we increase the field $\sigma_{\text{el}}(B)$ starts off at $\sigma_{\text{el,bg}}$, decreases to a minimum, turns round to increase to a maximum before it gradually returns to its background

value. The profile of the elastic cross section is antisymmetric about the resonance position. For systems that have very weak background inelastic scattering, ie. $S_{00,\text{bg}}$ is very nearly on the unit circle, unitarity requires θ_{bg} to be approximately zero, imposing the above behavior.

For strong background inelastic cross sections an extreme case can be identified with $\theta_{\text{bg}} = 180°$ when the background inelastic cross section is the largest value of $\sigma_{\text{inel}}^{\text{tot}}$. The inelastic cross section reduces, reaching a minimum at resonance, and asymptotically rises back to $\sigma_{\text{inel,bg}}^{\text{tot}}$. The profile is symmetric about B_{res} and is an inversion of the $\theta_{\text{bg}} = 0°$ case. The elastic cross section will be antisymmetric as before, except that for circulation in the same direction it will start by rising to a maximum. For $0° < \theta < 180°$, the inelastic cross section will show both a *reduction* as well as an *increase* at different points across a resonance. The profile is asymmetric with two extrema (a maximum and minimum). The degree of oscillations depends on the radius r_0 of the S-matrix circle. The impact of the resonance depends in particular on the relative magnitudes of the oscillation to the background.

For a resonance tuned magnetically at constant collision energy the eigenphase sum is given by

$$\Sigma(B) = \Sigma_{\text{bg}} + \arctan\left[\frac{\Gamma_B}{2(B_{\text{res}} - B)}\right], \tag{5.21}$$

with $\Gamma_B = \Gamma_E/\Delta\mu$. The S-matrix element is given by

$$S_{00}(B) = S_{\text{bg,00}} + \frac{ig_{B0}^2}{B - B_{\text{res}} + i\Gamma_B/2} \tag{5.22}$$

with $g_{B0} = g_{E0}/\Delta\mu^{1/2}$ and $\Gamma_{B0} = \Gamma_{E0}/\Delta\mu$. The radius can be expressed as $r_{00} = \Gamma_{B0}/\Gamma_B$. We note that in the case of a single-channel the total and partial widths are effectively the same, resulting in a circle of unit radius regardless of the collision energy. The singularity in the scattering length cannot be avoided in this case. For a well isolated resonance, the total width is simply the sum of the individual *partial widths*. Expressed mathematically
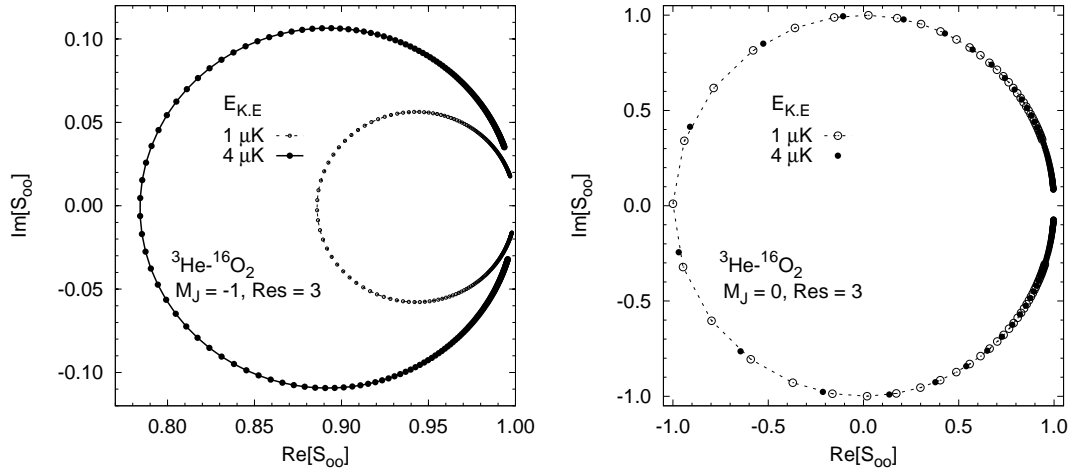
$$\Gamma_B = \sum_i \Gamma_{Bi}. \tag{5.23}$$

Figure 5.17: The left panel shows S-Matrix elements across resonance Res 1, $M_J = -2$, of ^{3}He-^{16}O$_2$, for collision energies 1 μK and 4 μK. Inelastic collisions to channels of the $m_j = 0$ threshold are possible in this case. The radius of the two circles differ by a factor of two, reflecting the $E^{1/2}$ dependence of the S-wave partial width. The right panel shows S-Matrix elements across Res 1, $M_J = 0$, of the same system. Only elastic collisions are possible in this case, and the S-matrix elements at both energies are of unit radius, indicating the independence of the radius in pure elastic scattering. Note the difference in the scales of figures on the left and right hand panels.

In the limit of low energy the magnitude of the partial width corresponding to the incoming channel $|\Gamma_{B0}|$ is proportional to k_0 [143]. The partial widths of inelastic channels on the other hand depend on open-channel wavenumbers, which are much larger and are nearly constant near zero-energy collisions. This means that as the energy decreases Γ_B is dominated by inelastic partial width contributions. Then $r_{00} \approx \Gamma_{B0}/\Gamma_B^{\text{inel}}$, where $\Gamma_B^{\text{inel}} = \Gamma_B - \Gamma_{B0}$, tends linearly to zero in the S-wave regime. The left side panel of figure 5.17 shows the S-matrix elements across Res 1 of the $M_J = -2$ symmetry of ^{3}He-^{16}O$_2$. Note the difference in scale with the circles of the right side panel representing elastic collisions. The two circles correspond to collision energies of 1 μK and 4 μK. The radius corresponding to 1 μK is about a factor of 2 less than that of 4 μK reflecting the $E^{1/2}$ proportionality between r_{00} and k_0. This is in contrast to the insensitivity of the radii of elastic resonances.

Like the S-Matrix element the scattering length traces a circle on the complex plane. With $|S_{00}| < 1$ the circle will not pass through (1,0) on the real axis, removing the singularity in the scattering length and dampening the maximum value of the cross sections. Both the real and complex components of the scattering length still change significantly across resonance. For r_{00} close to 1 the suppression of the scattering length is weak, and the cross sections obtain limiting values of $\sigma_{\text{el}} \approx 4\pi|a_0|^2$ and $\sigma_{\text{inel}}^{\text{tot}} \approx 4\pi\beta/k_0$. The scattering length can be expressed as [294]

$$a(B) = a_{\text{bg}} + \frac{a_{\text{res}}}{2(B - B_{\text{res}})/\Gamma_B^{\text{inel}} + i}. \tag{5.24}$$

where a_{bg} is the background term. The quantity a_{res} is a complex quantity and indicates the strength of resonant oscillations. The a_{bg} and a_{res} can be expressed in a similar manner to $a(B)$ as $a_{\text{res}} = \alpha_{\text{res}} - i\beta_{\text{res}}$, and, $a_{\text{bg}} = \alpha_{\text{bg}} - i\beta_{\text{bg}}$. The special case of purely elastic background scattering corresponds to real values of a_{res}, with a singularity at resonance. The real and imaginary parts of $a(B)$ can be written as [305]

$$\alpha(B) = \alpha_{\text{bg}} + \frac{\alpha_{\text{res}}[2(B - B_{\text{res}})/\Gamma_B^{\text{inel}}] - \beta_{\text{res}}}{[2(B - B_{\text{res}})/\Gamma_B^{\text{inel}}]^2 + 1} \tag{5.25}$$

and

$$\beta(B) = \beta_{\text{bg}} + \frac{\beta_{\text{res}}[2(B - B_{\text{res}})/\Gamma_B^{\text{inel}}] + \alpha_{\text{res}}}{[2(B - B_{\text{res}})/\Gamma_B^{\text{inel}}]^2 + 1}. \tag{5.26}$$

When the background scattering is purely elastic and the oscillations are symmetric, the imaginary part reaches a maximum value $|a_{\text{res}}|$ above its background value, while the real part oscillates between $\alpha_{bg} - |a_{\text{res}}|/2$ and $\alpha_{bg} + |a_{\text{res}}|/2$.

With the zero-energy resonance positions indicated by figures 5.8 and 5.10 we proceeded to performed scattering calculations for a range of fields across the indicated points. The collision energy, given in units of temperature as is conventional in the field, is held constant at 1 μK. The equivalent energy in joules can be calculated by multiplication by the Boltzmann constant k. The data on eigenphase sum output by MOLSCAT is plotted for a definitive signature of resonance. Figure 5.18 shows the eigenphase sum for resonances resulting from S-wave scattering in incoming channels of the $m_j = \pm 1$ and ± 2 thresholds of ^{3}He-^{16}O$_2$ and ^{4}He-^{16}O$_2$. The
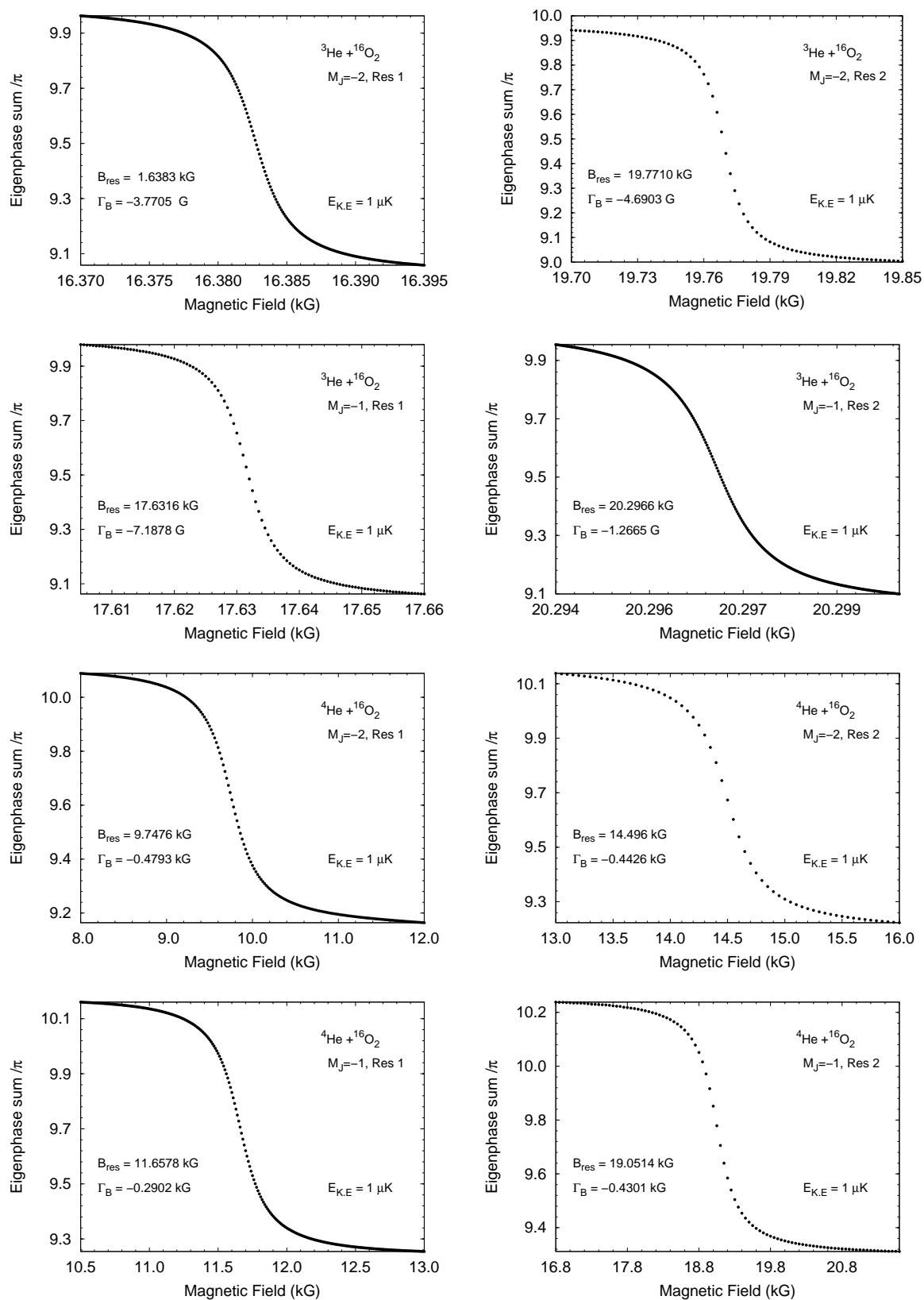
Figure 5.18: The eigenphase sum across resonances of ^{3}He-^{16}O$_2$ and ^{4}He-^{16}O$_2$ for $M_J = -2$ and -1 symmetry.

accuracy with which the quasi-bound state calculations predict the position of the resonance is notable. The calculated points are fitted to equation 5.21 to determine the total width Γ_B and position B_{res}. We use a quadratic term for the background Σ_{bg}. The MOLSCAT program also gives values of the individual S-Matrix elements which are fitted to equation 5.22 with the determined total width and resonance positions to obtain the partial widths. We also get the real and imaginary parts of the scattering length from the scattering calculations, and obtain the resonant and background terms by fitting. All fitting is done using the RESFIT [306] program. The results are given in tables 5.3 and 5.4.

Table 5.3: Characterization data of resonances of ^{3}He-^{16}O$_2$ with $M_J = -2$ and -1 symmetry. The negative sign of the partial widths indicates that the discrete state responsible for resonance crosses threshold from below. The real background term of the scattering length of the resonance at 19.7710 Gauss is best described by a linear function of the field, $\alpha_{\text{bg}}(B) = mB + c$. The gradient $m = 3 \times 10^{-6}$ Å and the constant $c = 0.5303$ Å.

M_J	B_{res}(kG)	Γ_B(G)	Γ_{B0}(G)	α_{bg}(Å)	α_{res}(Å)	β_{bg}(Å)	β_{res}(Å)
-2	16.3827	-3.7705	-0.2151	-0.7989	169.1685	0.02242	-3.7439
-2	19.7710	-4.6903	-0.3972	$----$	0.00040	0.00148	0.00037
-1	17.6316	-7.1878	-0.0836	-0.7679	34.4732	0.03424	-1.7706
-1	20.2966	-1.2665	-0.0940	-0.8642	220.1736	0.03257	2.6297

The real and imaginary parts of the scattering length across the resonances of ^{3}He-^{16}O$_2$ and ^{4}He-^{16}O$_2$ are shown in figures 5.19 and 5.20. From table 5.4 we estimate that for Res 1 of $M_J = -2$ of ^{3}He-^{16}O$_2$, which is at $B_{\text{res}} = 16.3827$ kG, $|a_{\text{res}}| \approx 170$ Å. The imaginary part of this resonance, shown on the top left hand panel of figure 5.19, reaches a maximum very close to this value. We note also that the real part is approximately antisymmetric, with a background value less that 1 percent of α_{res}. It oscillates about its near-zero background value with an amplitude

Table 5.4: Characterization data of resonances of ^{4}He-^{16}O$_2$ with $M_J = -2$ and -1 symmetry. The negative sign of the partial widths indicates that the discrete state responsible for resonance crosses threshold from below.

M_J	B_{res}(kG)	Γ_B(G)	Γ_{B0}(G)	α_{bg}(Å)	α_{res}(Å)	β_{bg}(Å)	β_{res}(Å)
-2	9.7476	-479.323	-14.9573	-65.6299	7.5560	2.3294	30.4895
-2	14.4961	-442.642	-16.2046	-74.6273	8.2622	6.4089	48.0724
-1	11.6577	-290.242	-8.4833	-69.0708	7.0634	3.5276	-28.9025
-1	19.0514	-430.138	-15.4457	-75.0970	8.4798	5.7891	-40.0072

$|a_{\mathrm{res}}|/2 \approx 85$ Å. The resonance at $B_{\mathrm{res}} = 20.2966$ kG has $|a_{\mathrm{res}}| \approx 220$ Å and its oscillations are of the same order. The oscillations of Res 1 at $B_{\mathrm{res}} = 17.6316$ kG are less pronounced, with $|a_{\mathrm{res}}| \approx 35$ Å. Resonance Res 2, of $M_J = -2$ symmetry at a field $B_{\mathrm{res}} = 19.7710$ kG, is even less pronounced with $|a_{\mathrm{res}}| \approx 4 \times 10^{-4}$ Å. The real background term, α_{bg}, varies linearly across the range shown. If we express it as $\alpha_{\mathrm{bg}}(B) = mB + c$, then the gradient $m = 3 \times 10^{-6}$ Å and the constant $c = 0.5303$ Å. For the resonances of ^{3}He-^{16}O$_2$ the real parts of the background scattering, α_{bg}, are at least an order of magnitude higher than the imaginary parts, β_{bg}. The elastic and inelastic cross sections are shown in figure 5.21. The lines represent the formulae 5.10 and 5.11 while the points are calculated values. We observe that inelastic scattering is stronger than elastic scattering across all resonances. The oscillations of the inelastic scattering cross sections are also more pronounced. The profile of these cross sections are qualitatively close to those discussed for $\theta_{\mathrm{bg}} \approx 0$.

Table 5.4 lists resonance data of ^{4}He-^{16}O$_2$. The a_{res} values are less than half those of ^{3}He-^{16}O$_2$ resonances, reducing the strength of the oscillations of $\alpha(B)$ and $\beta(B)$ as can be seen in figure 5.20 (Note the peaks as compared to figures of 5.19). However, in stark contrast, the background terms α_{bg} and β_{bg} are much stronger. The elastic background terms are generally an order of magnitude higher compared to ^{3}He-^{16}O$_2$, while the inelastic terms are two orders of magnitude higher. In ^{3}He-

Figure 5.19: The real and imaginary parts of the scattering length across resonances of ^{3}He-^{16}O$_2$, for $M_J = -2$ and -1 symmetry. For Res 2 of $M_J = -2$ symmetry, the y-axis of the real and imaginary parts have been separated, with the y-axis of the real part to the right. This is because of the difference in magnitude between them. Also note the 10^{-3} scaling factor, which applies to both real and imaginary parts.

^{16}O$_2$, the contributions to a_{res} were predominantly from the real term, α_{res}, while in ^{4}He-^{16}O$_2$ the imaginary terms, β_{res}, are significantly larger than the real components of the scattering length. Most notably, the cross sections of ^{4}He-^{16}O$_2$ are asymmetric about the resonance fields, and the inelastic cross sections show *reductions* across resonance. Figure 5.22 shows the cross sections in log scale. The asymmetry of the cross sections of ^{4}He-^{16}O$_2$, and the contrast with ^{3}He-^{16}O$_2$, is more clearly visible. We are also better able to see just how significant the reductions in the inelastic cross sections in the ^{4}He-^{16}O$_2$ system are. For the resonances of $M_J = -2$ the inelastic cross sections deep below the elastic cross. For Res 2, at $B_{\text{res}} = 9.7476$ kG, the inelastic cross section stays below the elastic cross section for a range of field of over 1000 Gauss. The profile of the cross sections correspond to larger values of the angle θ_{bg} compared to the ^{3}He-^{16}O$_2$ system.
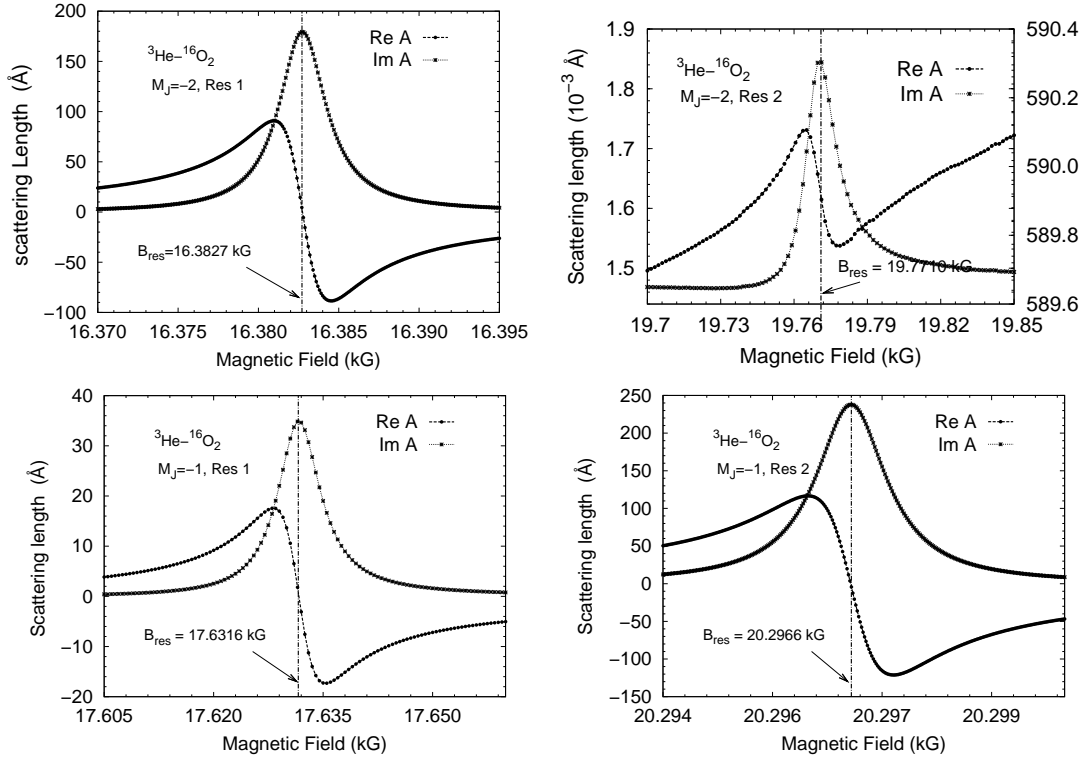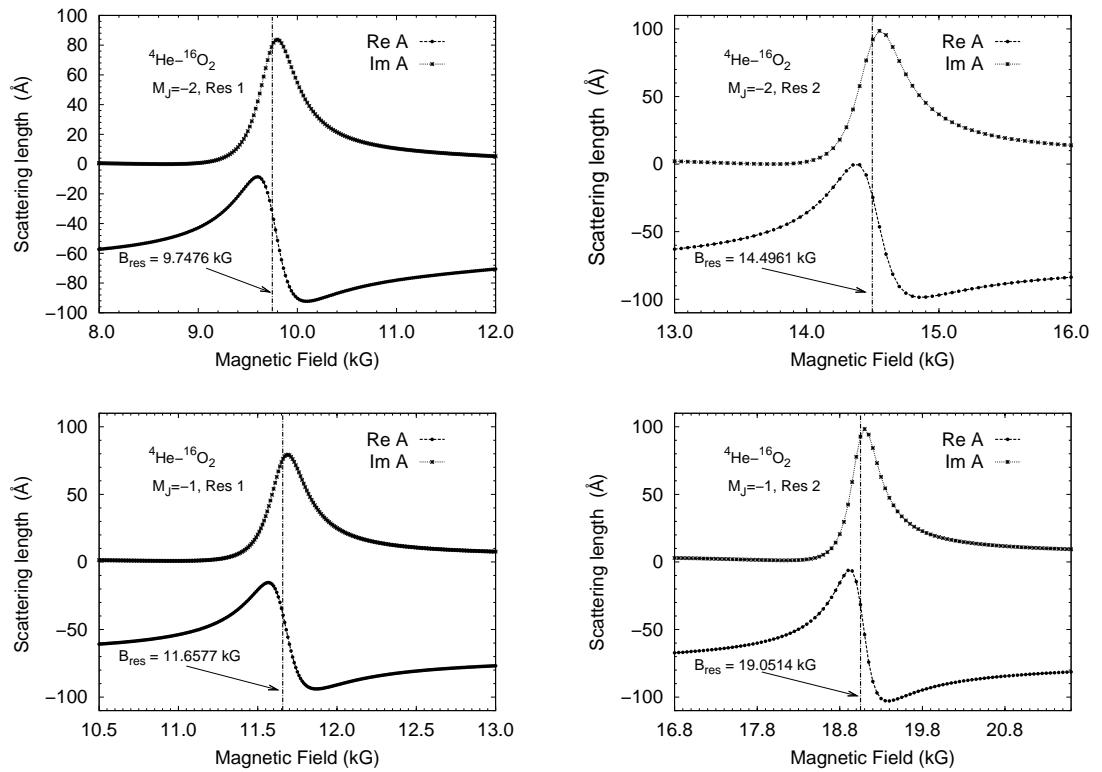
Figure 5.20: The real and imaginary parts of the scattering length across resonances of ^{4}He-^{16}O$_2$, for $M_J = -2$ and -1 symmetry.

5.5   Dramatic suppression of cross sections

The most notable result of our characterization of cross sections is the dramatic suppression of the inelastic cross section across the $M_J = -2$ resonances of ^{4}He-^{16}O$_2$. At its lowest the inelastic cross section reduces by a factor of 10^3 from its background value. This is potentially of great importance to cooling techniques that rely on thermal contact between two species such as evaporative [307] and buffer gas cooling [104]. It is also potentially good news for efforts to reduce trap loss. Figure 5.23 shows the inelastic cross section across Res 1 for collision energies of 1 μK, 100 μK and 10 mK. The figure also shows the resonance position of the 1 μK case. The position of the resonance is shifted slightly for the different collision energies. This is because the quasi-bound state must be raised above threshold by an amount equal to the collision energy to be in exact resonance with the scattering state. This requires different fields for the different energies. The suppression of cross section is of similar magnitude for the different temperatures and has its minimum
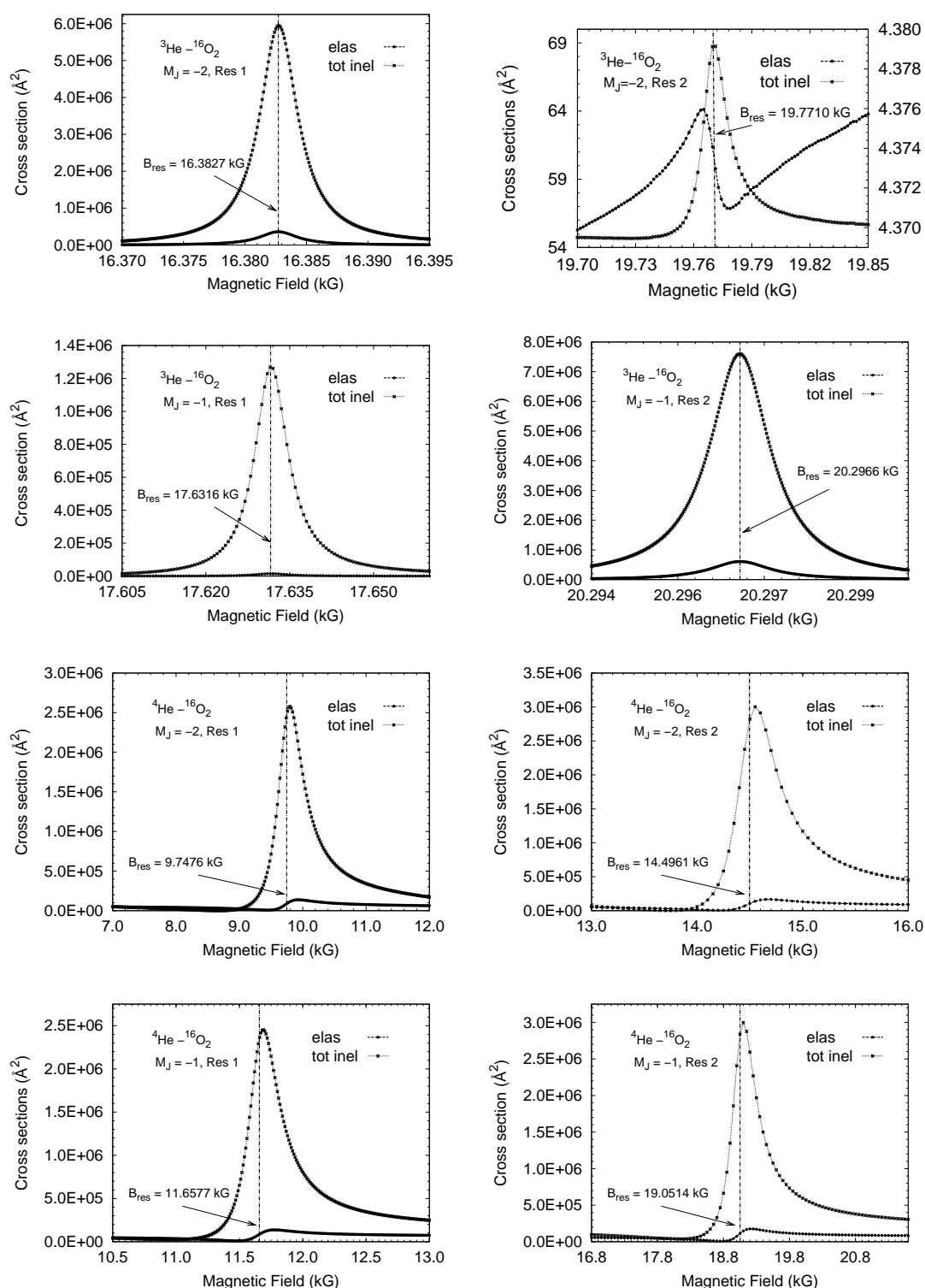
Figure 5.21: The elastic and total inelastic cross sections of ^{3}He-^{16}O$_2$ and ^{4}He-^{16}O$_2$, for $M_J = -2$ and -1 symmetry. For Res 2 of ^{3}He-^{16}O$_2$, $M_J = -2$, the y-axis of the elastic and total inelastic cross sections have been separated, with the y-axis of the total inelastic cross sections to the right.
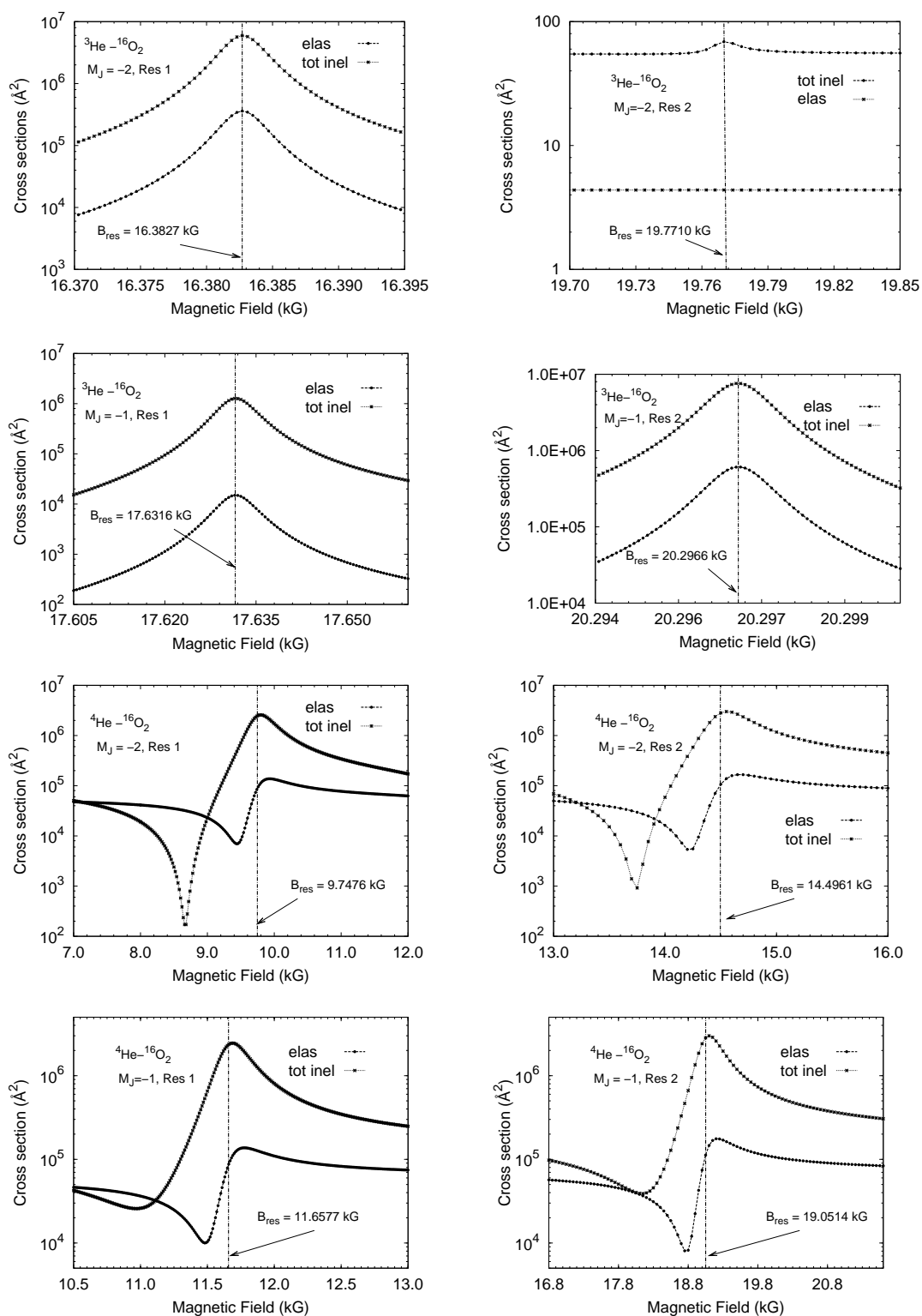
Figure 5.22: The elastic and total inelastic cross sections of ^{3}He-^{16}O$_2$ and ^{4}He-^{16}O$_2$, for $M_J = -2$ and -1 symmetry, plotted in a log-scaled graph. The extent of the suppression across resonance is more clearly visible.
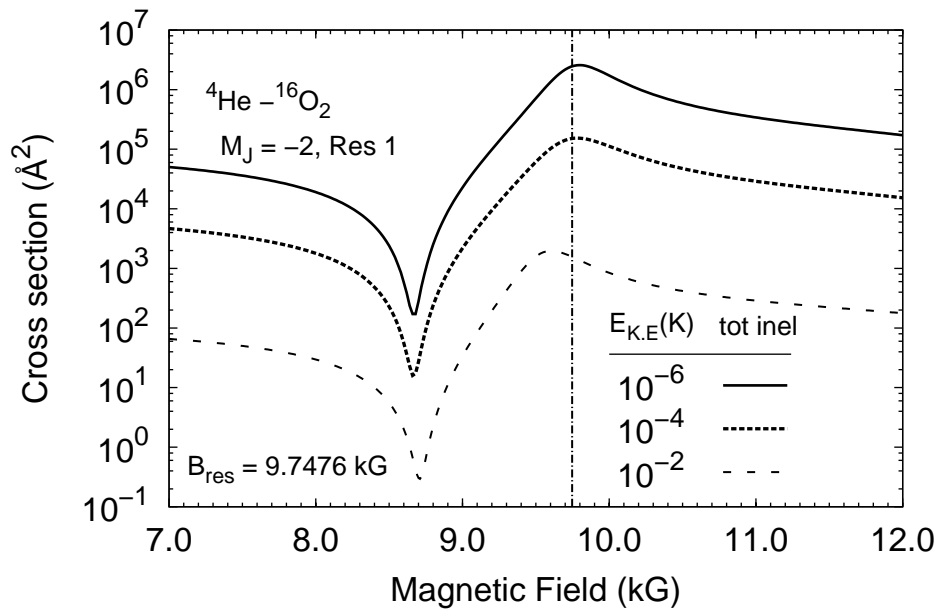
Figure 5.23: The total inelastic cross sections across resonance Res 1, $M_J = -2$, of ^{4}He-^{16}O$_2$. The collision energies are 10 mK, 100 μK and 1 μK.

at about 8700 Gauss. The cross sections are lower at higher temperatures, with the minimum reaching less than 1 Å for 10 mK. We note that the difference in the background inelastic cross section reduces by exactly a factor of 10 between 1 μK and 100 μK. This is indicative of the validity of the Wigner threshold regime. In contrast increasing the collision energy to 10 mK results in nearly two orders of magnitude reduction in the inelastic cross sections. This is a much faster reduction than is predicted by the threshold laws.

Figure 5.24 reveals that the elastic cross section does not oscillate as strongly. We note that the 1 μK and 100 μK elastic cross sections almost completely overlap, as would be expected from the threshold laws, while the 10 mK point is clearly outside the Wigner regime. More significant is the fact that the minima in the elastic cross sections occur at about 9500 Gauss. This is well away from the minima of the inelastic cross sections. As we see from figure 5.25 this results in a dramatic variation in the ratios of the elastic to total inelastic cross sections across both resonances of $M_J = -2$ symmetry. At its peak the ratio is about 100 at 1 μK and over 10^4 at 10 mK. The increase of this ratio with temperature reflects the properties of
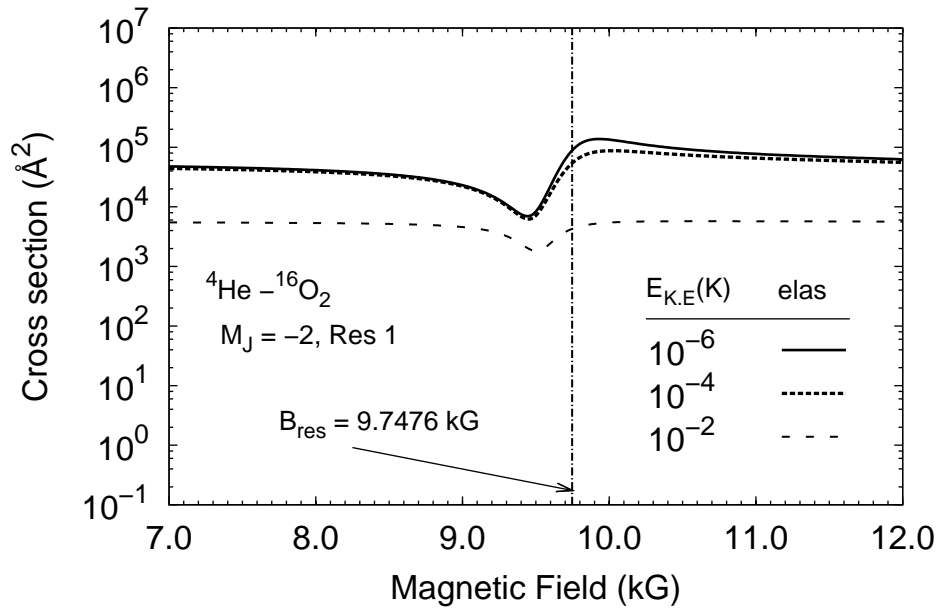
Figure 5.24: The elastic cross sections across resonance Res 1, $M_J = -2$, of ^{4}He-^{16}O$_2$. The collision energies are 10 mK, 100 μK and 1 μK.

the threshold laws and the fact that these laws continue to hold across resonance. This indicates the promise of efficient cooling and trapping across resonance. Cooling efficiency can, under suitable circumstances, increase with temperature. The resonances have widths of hundreds of Gauss. This is much wider than resonances of He-NH [294] considered previously in our group (which are of order 10^{-2} Gauss). For resonances of ^{4}He-^{16}O$_2$ $M_J = -2$, the large widths result in suppression of inelastic cross sections over a field range of more than a 100 Gauss. This results in favorable elastic to inelastic cross section ratios over a similarly wide range of fields as we can see from 5.25.

The cross sections of ^{4}He-^{16}O$_2$ have the profile of Fano line shapes. Fano [308] considered absorbtion spectra across resonances as a function of energy. For a discrete state embedded in a single continuum, he showed that contributions to the transition matrix from the discrete state attains a maximum at resonance, diminishing to zero symmetrically on either side. Contributions from the continuum states reach a maximum furthest from resonance, reaching zero and changing sign at a resonance. This means that there would be only constructive interference between the
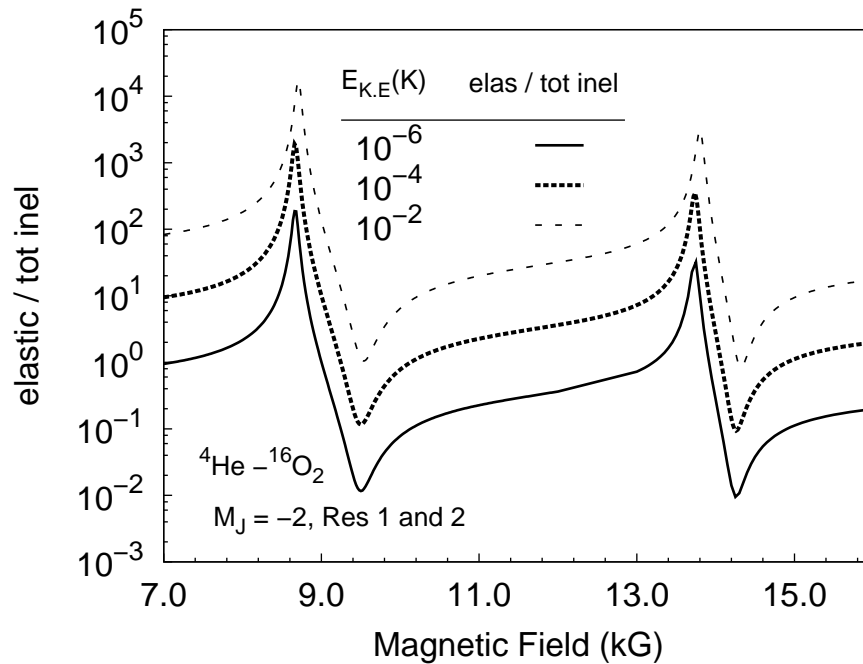
Figure 5.25: The ratio of elastic to total inelastic cross sections across a range of fields that includes resonances Res 1 and Res 2 $M_J = -2$ of ^{4}He-^{16}O$_2$. The collision energies are 10 mK, 100 μK and 1 μK.

contributions of the discrete and continuum states on one side of a resonance. On the other side there would be only destructive interference with complete cancelation at some energy. For a discrete state embedded in N continua it is always possible to diagonalize the Hilbert space such that the discrete state is coupled to a single continuum corresponding to some linear combination of the N continua. Interference, and complete cancelation, will now occur with contributions from states of this continuum. The absorbtion profile is similar to the case of a single continuum with the crucial exception that there is a constant background term, unaffected by resonance, resulting from transitions to the $N - 1$ continua not coupled to the discrete state. The transition probability is never completely zero.

We can apply Fano's explanation of absorbtion spectra to our scattering process which similarly constitutes transitions to states across resonance. We consider the coupling of the discrete state to all open channels. In the low-energy regime coupling to channels of the incoming threshold diminish linearly with the collision energy. For

Res 1 of the $M_J = -2$ symmetry we can therefore ignore coupling to channels of the $j = 2, m_j = -2$ threshold. At resonance the kinetic energy released on transition to the $j = 0, m_j = 0$ threshold is about 1.4 cm^{-1}. This is well above the $L = 2$ barrier but does not clear the $L = 4$ barrier. However, the energy is sufficient to allow significant transitions to the $L = 4$ channel. The magnitude of the partial widths are 455 Gauss and 1.01 Gauss for the $L = 2$ and $L = 4$ partial waves, respectively. The discrete state is more strongly coupled to the $L = 2$ channel. Therefore, the resonance suppresses transitions to the $L = 2$ channel which contributes most to the inelastic cross section, leading to an overall dramatic reduction in the inelastic transitions. The behavior is similar across Res 2.

In contrast suppression of the inelastic cross section is much less pronounced for the resonances of $M_J = -1$ symmetry. In this case there are two thresholds below the incoming channel ($j = 2, m_j = -2$ and $j = 0, m_j = 0$). The release of energy at, say, Res 1 is about 0.3 cm^{-1} on transition to the $j = 2, m_j = -2$ threshold and 1.6 cm^{-1} to the $j = 0, m_j = 0$ threshold. This is enough to clear the $L = 2$ barrier. The magnitude of the partial widths are 2.99 and 276 Gauss for $L = 2$ of the $j = -2, m_j = -2$ and $j = 0, m_j = 0$ thresholds, respectively. The $L = 4$ partial wave of the $j = 0, m_j = 0$ threshold has a partial width of magnitude 3.83 Gauss and contributes significantly to the inelastic cross section. The dominant contribution to the inelastic cross sections is from transitions to the channels of the lowest threshold. Although this channel is also more strongly coupled to the discrete state there is still significant inelastic cross section to the $L = 2$ channel of the $j = 2, m_j = -2$ threshold. The resulting suppression is much less dramatic.

5.6 Conclusion

The objective of our study was to locate and characterize resonances of He-O$_2$ with an aim of increasing our understanding of the potential of Feshbach resonance tuning as a tool for the control of collision outcome in atomic and molecular systems. It is with some satisfaction that we reported [309] dramatic suppressing of the inelastic

cross sections, by magnetic tuning of Feshbach resonances, in collisions of ^{4}He with ^{16}O$_2$. We have also managed to interpret the results in terms of Fano line shapes, helping to establish the conditions necessary for the favorable application of this technique. Suppression of inelastic collisions increases thermalization efficiency and is potentially very useful for important cooling methods such as evaporative and sympathetic cooling. Additionally, loss of atoms and molecules from traps during cooling can be reduced by suppressing transitions to untrappable states. More interesting and complex systems have greater densities of resonances. Thus resonances will continue to be of central importance in future research in the area of ultracold physics. The ability to tune Feshbach resonances can potentially convert what is a challenge to the control and manipulation of molecular systems to an exploitable feature.

Future research to complement our work could look for similar suppression of inelastic cross sections in other systems. This could establish how common the conditions for such suppression are and help consolidate our understanding of the mechanisms involved. It is also possible to study the effects of using electric fields to tune Feshbach resonances. Electric fields do not conserve parity and couple a different set of levels, introducing new and interesting possibilities.

Bibliography

[1] Chu, S.; Hollberg, L.; Bjorkholm, J. E.; Cable, A.; Ashkin, A. *Phys. Rev. Lett.* **1985**, *55*(1), 48.

[2] Anderson, M. H.; Ensher, J. R.; Matthews, M. R.; Wieman, C. E.; Cornell, E. A. *Science* **1995**, *269*(5221), 198.

[3] Davis, K. B.; Mewes, M. O.; Andrews, M. R.; VanDruten, N. J.; Durfee, D. S.; Kurn, D. M.; Ketterle, W. *Phys. Rev. Lett.* **1995**, *75*(22), 3969.

[4] Kagan, Y.; Shlyapnikov, G. V.; Walraven, J. T. M. *Phys. Rev. Lett.* **1996**, *76*(15), 2670.

[5] Bradley, C. C.; Sackett, C. A.; Hulet, R. G. *Phys. Rev. Lett.* **1997**, *78*(6), 985.

[6] Donley, E. A.; Claussen, N. R.; Cornish, S. L.; Roberts, J. L.; Cornell, E. A.; Wieman, C. E. *Nature* **2001**, *412*(6844), 295.

[7] Courteille, P.; Freeland, R. S.; Heinzen, D. J.; van Abeelen, F. A.; Verhaar, B. J. *Phys. Rev. Lett.* **1998**, *81*(1), 69.

[8] Cornish, S. L.; Claussen, N. R.; Roberts, J. L.; Cornell, E. A.; Wieman, C. E. *Phys. Rev. Lett.* **2000**, *85*(9), 1795.

[9] Fedichev, P. O.; Kagan, Y.; Shlyapnikov, G. V.; Walraven, J. T. M. *Phys. Rev. Lett.* **1996**, *77*(14), 2913.

[10] Bohn, J. L.; Julienne, P. S. *Phys. Rev. A* **1996**, *54*(6), R4637.

[11] Bohn, J. L.; Julienne, P. S. *Phys. Rev. A* **1997**, *56*(2), 1486.

[12] Fatemi, F. K.; Jones, K. M.; Lett, P. D. *Phys. Rev. Lett.* **2000**, *85*(21), 4462.

[13] Westbrook, C. I.; Watts, R. N.; Tanner, C. E.; Rolston, S. L.; Phillips, W. D.; Lett, P. D.; Gould, P. L. *Phys. Rev. Lett.* **1990**, *65*(1), 33.

[14] Greiner, M.; Mandel, O.; Esslinger, T.; Hänsch, T. W.; Bloch, I. *Nature* **2002**, *415*(6867), 39.

[15] Greiner, M.; Regal, C. A.; Jin, D. S. Dec **2003**, *426*(6966), 537.

[16] Sortais, Y.; Bize, S.; Abgrall, M.; Zhang, S.; Nicolas, C.; Mandache, C.; P. Lemonde, P. L.; Santarelli, G.; Dimarcq, N.; Petit, P.; Clairon, A.; Mann, A.; Chang, A. L. S.; Salomon, C. *Physica Scripta* **2001**, *2001*(T95), 50.

[17] Hollberg, L.; Oates, C. W.; Wilpers, G.; Hoyt, C. W.; Barber, Z. W.; Diddams, S. A.; Oskay, W. H.; Bergquist, J. C. *J. Phys. B – At. Mol. Opt. Phys.* **2005**, *38*(9), S469.

[18] Bize, S.; Laurent, P.; Abgrall, M.; Marion, H.; Maksimovic, I.; Cacciapuoti, L.; Grnert, J.; Vian, C.; dos Santos, F. P.; Rosenbusch, P.; Lemonde, P.; Santarelli, G.; Wolf, P.; Clairon, A.; Luiten, A.; Tobar, M.; Salomon, C. *J. Phys. B – At. Mol. Opt. Phys.* **2005**, *38*(9), S449.

[19] Khaykovich, L.; Schreck, F.; Ferrari, G.; Bourdel, T.; Cubizolles, J.; Carr, L. D.; Castin, Y.; Salomon, C. *Science* **2002**, *296*(5571), 1290.

[20] Mark, M.; Kraemer, T.; Waldburger, P.; Herbig, J.; Chin, C.; Nägerl, H.-C.; Grimm, R. *Phys. Rev. Lett.* **2007**, *99*(11), 113201.

[21] Hart, R. A.; Xu, X.; Legere, R.; Gibble, K. *Nature* **2007**, *446*(7138), 892.

[22] Bennett, S. C.; Wieman, C. E. *Phys. Rev. Lett.* **1999**, *82*(12), 2484.

[23] Young, R. D.; Carlini, R. D.; Thomas, A. W.; Roche, J. *Phys. Rev. Lett.* **2007**, *99*(12), 122003.

[24] Hudson, J. J.; Sauer, B. E.; Tarbutt, M. R.; Hinds, E. A. *Phys. Rev. Lett.* **2002**, *89*(2), 023003.

[25] Daussy, C.; Marrel, T.; Amy-Klein, A.; Nguyen, C. T.; Borde, C. J.; Chardonnet, C. *Phys. Rev. Lett.* **1999**, *83*(8), 1554.

[26] Bethlem, H. L.; Berden, G.; Meijer, G. *Phys. Rev. Lett.* **1999**, *83*(8), 1558.

[27] Bethlem, H. L.; van Roij, A. J. A.; Jongma, R. T.; Meijer, G. *Phys. Rev. Lett.* **2002**, *88*(13), 133003.

[28] Bethlem, H. L.; Berden, G.; Crompvoets, F. M. H.; Jongma, R. T.; van Roij, A. J. A.; Meijer, G. *Nature* **2000**, *406*(6795), 491.

[29] van Veldhoven, J.; Bethlem, H. L.; Meijer, G. *Phys. Rev. Lett.* **2005**, *94*(8), 083001.

[30] Crompvoets, F. M. H.; Bethlem, H. L.; Jongma, R. T.; Meijer, G. *Nature* **2001**, *411*(6834), 174.

[31] Heiner, C. E.; Carty, D.; Meijer, G.; Bethlem, H. L. *Nature Physics* **2007**, *3*, 115.

[32] Suominen, K. A. *J. Phys. B – At. Mol. Opt. Phys.* **1996**, *29*(24), 5891.

[33] Micheli, A.; Pupillo, G.; Büchler, H. P.; Zoller, P. *Phys. Rev. A.* **2007**, *76*, 043604.

[34] Büchler, H. P.; Demler, E.; Lukin, M.; Micheli, A.; Prokofév, N.; Pupillo, G.; Zoller, P. *Phys. Rev. Lett.* **2007**, *98*(6), 060404.

[35] Fisher, M. P. A.; Weichman, P. B.; Grinstein, G.; Fisher, D. S. *Phys. Rev. B* **1989**, *40*(1), 546.

[36] Góral, K.; Santos, L.; Lewenstein, M. *Phys. Rev. Lett.* **2002**, *88*(17), 170406.

[37] Volz, T.; Syassen, N.; Bauer, D. M.; Hansis, E.; Dürr, S.; Rempe, G. *arXiv* **2006**, pages cond–mat/0605184.

[38] Friedrich, B.; Herschbach, D. *Phys. Chem. Chem. Phys.* **2000**, *2*, 419.

[39] Aldegunde, J.; Alvariño, J. M.; de Miranda, M. P.; Rábanos, V. S.; Aoiz, F. J. *J. Chem. Phys.* **2006**, *125*(13), 133104.

[40] Baranov, M.; Dobrek, Ł.; Góral, K.; Santos, L.; Lewenstein, M. *Phys. Scr.* **2002**, *T102*, 74.

[41] Sadeghpour, H. R.; Bohn, J. L.; Cavagnero, M. J.; Esry, B. D.; Fabrikant, I. I.; Macek, J. H.; Rau, A. R. P. *J. Phys. B – At. Mol. Opt. Phys.* **2000**, *33*(5), R93.

[42] Gorshkov, A. V.; Rabl, P.; Pupillo, G.; Micheli, A.; Zoller, P.; Lukin, M. D.; Büchler, H. P. *Phys. Rev. Lett.* **2008**, *101*(7), 073201.

[43] Santos, L.; Shlyapnikov, G. V.; Soller, P.; Lewenstein, M. *Phys. Rev. Lett.* **2000**, *85*(9), 1791.

[44] Santos, L.; Shlyapnikov, G. V.; Lewenstein, M. *Phys. Rev. Lett.* **2003**, *90*(25), 250403.

[45] Carr, L. D.; DeMille, D.; Krems, R. V.; Ye, J. *New J. Phys.* **2009**, *11*, 055049.

[46] van Veldhoven, J.; Küpper, J.; Bethlem, H. L.; Sartakov, B.; van Roij, A. J. A.; Meijer, G. *Eur. Phys. J. D* **2004**, *31*(2), 337.

[47] Gilijamse, J. J.; Hoekstra, S.; van de Meerakker, S. Y. T.; Groenenboom, G. C.; Meijer, G. *Science* **2006**, *313*, 1617.

[48] Thorsheim, H. R.; Weiner, J.; Julienne, P. S. *Phys. Rev. Lett.* **1987**, *58*(23), 2420.

[49] Fioretti, A.; Comparat, D.; Crubellier, A.; Dulieu, O.; Masnou-Seeuws, F.; Pillet, P. *Phys. Rev. Lett.* **1998**, *80*(20), 4402.

[50] Fioretti, A.; Comparat, D.; Drag, C.; Amiot, C.; Dulieu, O.; Masnou-Seeuws, F.; Pillet, P. *Eur. Phys. J. D* **1999**, *5*(3), 389.

[51] de Araujo, L. E. E.; Weinstein, J. D.; Gensemer, S. D.; Fatemi, F. K.; Jones, K. M.; Lett, P. D.; Tiesinga, E. *J. Chem. Phys.* **2003**, *119*(4), 2062.

[52] Stwalley, W. C.; Wang, H. *J. Mol. Spectrosc.* **1999**, *195*(2), 194.

[53] Jones, K. M.; Tiesinga, E.; Lett, P. D.; Julienne, P. S. *Rev. Mod. Phys.* **2006**, *78*(2), 483.

[54] van de Meerakker, S. Y. T.; Vanhaecke, N.; van der Loo, M. P. J.; Groenenboom, G. C.; Meijer, G. *Phys. Rev. Lett.* **2005**, *95*(1), 013003.

[55] van der Loo, M.; Groenenboom, G. *J. Chem. Phys.* **2007**, *126*(11), 114314.

[56] Heiner, C. E.; Bethlem, H. L.; Meijer, G. *Phys. Chem. Chem. Phys.* **2006**, *8*(23), 2666.

[57] Flambaum, V. V.; Kozlov, M. G. *Phys. Rev. Lett.* **2007**, *99*(15), 150801.

[58] Zelevinsky, T.; Kotochigova, S.; Ye, J. *Phys. Rev. Lett* **2008**, *100*(4), 043201.

[59] DeMille, D.; Sainis, S.; Sage, J.; Bergeman, T.; Kotochigova, S.; Tiesinga, E. *Phys. Rev. Lett.* **2008**, *100*(4), 043202.

[60] Kotochigova, S.; Zelevinsky, T.; Ye, J. *Phys. Rev. A* **2009**, *79*(1), 012504.

[61] Hudson, E. R.; Lewandowski, H. J.; Sawyer, B. C.; Ye, J. *Phys. Rev. Lett.* **2006**, *96*(14), 143004.

[62] Uzan, J. P. *Rev. Mod. Phys.* **2003**, *75*(2), 403.

[63] Wu, C. S.; Ambler, E.; Hayward, R. W.; Hoppes, D. D.; Hudson, R. P. *Phys. Rev.* **1957**, *105*(4), 1413.

[64] Christenson, J. H.; Cronin, J. W.; Fitch, V. L.; Turlay, R. *Phys. Rev. Lett.* **1964**, *13*(4), 138.

[65] Garwin, R. L.; Lederman, L. M.; Weinrich, M. *Phys. Rev.* **1957**, *105*(4), 1415.

[66] Kozlov, M. G.; DeMille, D. *Phys. Rev. Lett.* **2002**, *89*(13), 133001.

[67] Bickman, S.; Hamilton, P.; Jiang, Y.; DeMille, D. *Phys. Rev. A* **2009**, *80*(2), 023418.

[68] Vutha, A. C.; Campbell, W. C.; Gurevich, Y. V.; Hutzler, N. R.; Parsons, M.; Patterson, D.; Petrik, E.; Spaun, B.; Doyle, J. M.; Gabrielse, G.; DeMille, D. *J. Phys. B – At. Mol. Opt. Phys.* **2010**, *43*(7, Sp. Iss. SI).

[69] Crassous, J.; Chardonnet, C.; Saue, T.; Schwerdtfeger, P. *Org. Biomol. Chem.* **2005**, *3*(12), 2218.

[70] Quack, M.; Stohner, J. *Chimia* **2005**, *59*(7-8), 530.

[71] Wigner, E. P. *Phys. Rev.* **1948**, *73*(9), 1002.

[72] Balakrishnan, N.; Dalgarno, A. *Chem. Phys. Lett.* **2001**, *341*(5-6), 652.

[73] Bodo, E.; Gianturco, F. A.; Dalgarno, A. *J. Chem. Phys.* **2002**, *116*(21), 9222.

[74] Bodo, E.; Gianturco, F. A. *Eur. Phys. J. D* **2004**, *31*(2), 423.

[75] Weck, P. F.; Balakrishnan, N. *J. Chem. Phys.* **2005**, *122*(15), 154309.

[76] Balakrishnan, N. *J. Chem. Phys.* **2004**, *121*(12), 5563.

[77] Weck, P. F.; Balakrishnan, N. *Int. Rev. Phys. Chem.* **2006**, *25*(3), 283.

[78] Weck, P. F.; Balakrishnan, N. *J. Chem. Phys.* **2005**, *123*(14), 144308.

[79] Takayanagi, T.; Kurosaki, Y. *J. Chem. Phys.* **1998**, *109*(20).

[80] Skodje, R. T.; Skouteris, D.; Manolopoulos, D. E.; Lee, S. H.; Dong, F.; K.Liu. *Phys. Rev. Lett.* **2000**, *85*(6), 1206.

[81] Cvitaš, M. T.; Soldán, P.; Hutson, J. M.; Honvault, P.; Launay, J. M. *Phys. Rev. Lett.* **2005**, *94*(20), 200402.

[82] Balakrishnan, N.; Dalgarno, A. *J. Phys. Chem. A* **2003**, *107*(37), 7101.

[83] Bodo, E.; Gianturco, F. A.; Dalgarno, A. *J. Phys. B – At. Mol. Opt. Phys.* **2002**, *35*(10), 2391.

[84] Bodo, E.; Gianturco, F. A.; Balakrishnan, N.; Dalgarno, A. *J. Phys. B – At. Mol. Opt. Phys.* **2004**, *37*(18), 3641.

[85] Quéméner, G.; Balakrishnan, N. *J. Chem. Phys.* **2008**, *128*(22), 224304.

[86] Balakrishnan, N. *J. Chem. Phys.* **2004**, *121*(13), 6346.

[87] Weck, P. F.; Balakrishnan, N.; Brandao, J.; Rosa, C.; Wang, W. *J. Chem. Phys.* **2006**, *124*(7), 074308.

[88] Weck, P. F.; Balakrishnan, N. *Eur. Phys. J. D* **2004**, *31*(2), 417.

[89] Hubbard, J. *Proc. Roy. Soc. Lond. Series A-Mathematical and Physical Sciences* **1963**, *276*(1364), 238.

[90] Jaksch, D.; Zoller, P. *Ann. Phys.* **2005**, *52*, 315.

[91] Regal, C. A.; Greiner, M.; Jin, D. S. *Phys. Rev. Lett.* **2004**, *92*(4), 040403.

[92] Bartenstein, M.; Altmeyer, A.; Riedl, S.; Jochim, S.; Chin, C.; Denschlag, J. H.; Grimm, R. *Phys. Rev. Lett.* **2004**, *92*(12), 120401.

[93] Chin, C.; Bartenstein, M.; Altmeyer, A.; Riedl, S.; Jochim, S.; Denschlag, J. H.; Grimm, R. *Science* **2004**, *305*(5687), 1128.

[94] Partridge, G. B.; Strecker, K. E.; Kamar, R. I.; Jack, M. W.; Hulet, R. G. *Phys. Rev. Lett.* **2005**, *95*(2), 020404.

[95] I. B. Spielman, W. D. P.; Porto, J. V. *Phys. Rev. Lett.* **2007**, *98*(8), 080404.

[96] Stöferle, T.; Moritz, H.; Günter, K.; Köhl, M.; Esslinger, T. *Phys. Rev. Lett.* **2006**, *96*(3), 030401.

[97] Baranov, M. A. *Phys. Rep.* **2008**, *464*(3), 71.

[98] Capogrosso-Sansone, B.; Trefzger, C.; Lewenstein, M.; Zoller, P.; Pupillo, G. *Phys. Rev. Lett.* **2010**, *104*(12), 125301.

[99] Damski, B.; Santos, L.; Tiemann, E.; Lewenstein, M.; Kotochigova, S.; Julienne, P.; Zoller, P. *Phys. Rev. Lett.* **2003**, *90*(11), 110401.

[100] Lee, C.; Ostrovskaya, E. A. *Phys. Rev. A* **2005**, *72*(6), 062321.

[101] Menotti, C.; Trefzger, C.; Lewenstein, M. *Phys. Rev. Lett* **2007**, *98*(23), 235301.

[102] DeMille, D. *Phys. Rev. Lett.* **2002**, *88*(6), 067901.

[103] Ryytty, P.; Kaivola, M. *European Physical Journal D* **2000**, *12*(3), 415.

[104] Doyle, J. M.; Friedrich, B.; Kim, J.; Patterson, D. *Phys. Rev. A* **1995**, *52*, 2515.

[105] Ketterle, W.; VanDruten, N. *Adv. Atom. Mol. Opt. Phys.* **1996**, *37*, 181.

[106] Bethlem, H. L.; Meijer, G. *Int. Rev. Phys. Chem.* **2003**, *22*(1), 73.

[107] Friedburg, H.; Paul, W. *Naturwissenschaften* **1950**, *37*(1), 20.

[108] Gordon, J. P.; Zeiger, H. J.; Townes, C. H. *Phys. Rev.* **1954**, *95*(1), 282.

[109] G., B. H.; W., P.; Schlier, C. *Zeitschrift Für physik* **1955**, *141*(1-2), 6.

[110] Bethlem, H. L.; Berden, G.; van Roij, A. J. A.; Crompvoets, F. M. H.; Meijer, G. *Phys. Rev. Lett.* **2000**, *84*(25), 5744.

[111] Gubbels, K.; Meijer, G.; Friedrich, B. *Phys. Rev. A* **2006**, *73*(6), 063406.

[112] Tokunaga, S. K.; Dyne, J. M.; Hinds, E. A.; Tarbutt, M. R. *New J. Phys* **2009**, *11*, 055038.

[113] Gilijamse, J. J.; Hoekstra, S.; Vanhaecke, N.; van de Meerakker, S. Y. T.; Meijer, G. *Eur. J. Phys. D* **2010**, *57*(1), 33.

[114] Bochinski, J. R.; Hudson, E. R.; Lewandowski, H. J.; Meijer, G.; Ye, J. *Phys. Rev. Lett.* **2003**, *91*(24), 243001.

[115] van de Meerakker, S. Y. T.; Labazan, I.; Hoekstra, S.; Kuepper, J.; Meijer, G. *J. Phys. B – At. Mol. Opt. Phys.* **2006**, *39*(19), S1077.

[116] Hudson, E. R.; Ticknor, C.; Sawyer, B. C.; Taatjes, C. A.; Lewandowski, H. J.; Bochinski, J. R.; Bohn, J. L.; Ye, J. *Phys. Rev. A* **2006**, *73*(6), 063404.

[117] Jung, S.; Tiemann, E.; Lisdat, C. *Phys. Rev. A* **2006**, *74*(4), 040701.

[118] Tarbutt, M. R.; Bethlem, H. L.; Hudson, J. J.; Ryabov, V. L.; Ryzhov, V. A.; Sauer, B. E.; Meijer, G.; Hinds, E. A. *Phys. Rev. Lett.* **2004**, *92*(17), 173002.

[119] Bohn, J. L.; Avdeenkov, A. V.; Deskevich, M. P. *Phys. Rev. Lett.* **2002**, *89*(20), 203202.

[120] Bethlem, H. L.; Tarbutt, M. R.; Küpper, J.; Carty, D.; Wohlfart, K.; Hinds, E. A.; Meijer, G. *J. Phys. B – At. Mol. Opt. Phys.* **2006**, *39*(16), R263.

[121] Wohlfart, K.; Filsinger, F.; Graetz, F.; Kueppe, J.; Meijer, G. *Phys. Rev. A* **2008**, *78*(3), 03342.

[122] Wall, T. E.; Armitage, S.; Hudson, J. J.; Sauer, B. E.; Dyne, J. M.; Hinds, E. A.; Tarbutt, M. R. *Phys. Rev. A* **2009**, *80*(4), 043407.

[123] Wohlfart, K.; Graetz, F.; Filsinger, F.; Haak, H.; Meijer, G.; Kuepper, J. *Phys. Rev. A* **2008**, *77*(3), 031404.

[124] Kim, J. H.; Friedrich, B.; Katz, D. P.; Patterson, D.; Weinstein, J. D.; DeCarvalho, R.; Doyle, J. M. *Phys. Rev. Lett.* **1997**, *78*(19), 3665.

[125] Weinstein, J. D.; deCarvalho, R.; Kim, J.; Patterson, D.; Friedrich, B.; Doyle, J. M. *Phys. Rev. A* **1998**, *57*(5), R3173.

[126] Harris, J. G. E.; Michniak, R. A.; Nguyen, S. V.; Brahms, N.; Ketterle, W.; Doyle, J. M. *Europhys. Lett.* **2004**, *67*(2), 198.

[127] Weinstein, J. D.; deCarvalho, R.; Guillet, T.; Friedrich, B.; Doyle, J. M. *Nature* **1998**, *395*(6698), 148.

[128] Egorov, D.; Campbell, W. C.; Friedrich, B.; Maxwell, S. E.; Tsikata, E.; van Buuren, L. D.; Doyle, J. M. *Eur. Phys. J. D* **2004**, *31*(2), 307.

[129] Campbell, W. C.; Tsikata, E.; Lu, H.; van Buuren, L. D.; Doyle, J. M. *Phys. Rev. Lett.* **2007**, *98*(21), 213001.

[130] Doret, S. C.; Connolly, C. B.; Ketterle, W.; Doyle, J. M. *Phys. Rev. Lett.* **2009**, *103*(10), 103005.

[131] Takekoshi, T.; Knize, R. J. *Opt. Lett.* **1996**, *21*(1), 77.

[132] Dong, G. J.; Lu, W. P.; Barker, P. F. *Phys. Rev. A* **2004**, *69*(1), 013409.

[133] Fulton, R.; Bishop, A. I.; Shneider, M. N.; Barker, P. F. *Nature Physics* **2006**, *2*(7), 465.

[134] Modugno, G.; Ferrari, G.; Roati, G.; Brecha, R. J.; Simoni, A.; Inguscio, M. *Science* **2001**, *294*(5545), 1320.

[135] Lara, M.; Bohn, J. L.; Potter, D.; Soldán, P.; Hutson, J. M. *Phys. Rev. Lett.* **2006**, *97*(18), 183201.

[136] Lara, M.; Bohn, J. L.; Potter, D. E.; Soldán, P.; Hutson, J. M. *Phys. Rev. A* **2007**, *75*(1), 012704.

[137] Żuchowski, P. S.; Hutson, J. M. *Phys. Rev. A* **2009**, *79*(6), 062708.

[138] Żuchowski, P. S.; Hutson, J. M. *Phys. Rev. A* **2008**, *78*(2), 022701.

[139] Soldán, P.; Hutson, J. M. *Phys. Rev. Lett.* **2004**, *92*(16), 163202.

[140] Soldán, P.; Żuchowski, P. S.; Hutson, J. M. *Faraday Discuss.* **2009**, *142*, B822769C.

[141] Wallis, A. O. G.; Hutson, J. M. *Phys. Rev. Lett.* **2009**, *103*(18), 183201.

[142] Moerdijk, A. J.; Verhaar, B. J.; Axelsson, A. *Phys. Rev. A* **1995**, *51*(6), 4852.

[143] Timmermans, E.; Tommasini, P.; Hussein, M.; Kerman, A. *Phys. Rep.* **1999**, *315*(1-3), 199.

[144] Ospelkaus, S.; Pe'er, A.; Ni, K.-K.; Zirbel, J. J.; Neyenhuis, B.; Kotochigova, S.; Julienne, P. S.; Ye, J.; Jin, D. S. *Nature Physics* **2008**, *4*, 622.

[145] Nikolov, A. N.; Eyler, E. E.; Wang, X. T.; Li, J.; Wang, H.; Stwalley, W. C.; Gould, P. L. *Phys. Rev. Lett.* **1999**, *82*(4), 703.

[146] Winkler, K.; Thalhammer, G.; Theis, M.; Ritsch, H.; Grimm, R.; Denschlag, J. H. *Phys. Rev. Lett.* **2005**, *95*(6), 063202.

[147] Gaubatz, U.; Rudecki, P.; Schiemann, S.; Bergmann, K. *J. Chem. Phys.* **1990**, *92*(9), 5363.

[148] Luc-Koenig, E.; Vatasescu, M.; Masnou-Seeuws, F. *Eur. Phys. J. D* **2004**, *31*(2), 239.

[149] Luc-Koenig, E.; Kosloff, R.; Masnou-Seeuws, F.; Vatasescu, M. *Phys. Rev. A* **2004**, *70*(3), 033414.

[150] Koch, C. P.; Luc-Koenig, E.; Masnou-Seeuws, F. *Phys. Rev. A* **2006**, *73*(3), 033408.

[151] Samuelis, C.; Tiesinga, E.; Laue, T.; Elbs, M.; Knöckel, H.; Tiemann, E. *Phys. Rev. A* **2000**, *63*(1), 012710.

[152] Nikolov, A. N.; Ensher, J. R.; Eyler, E. E.; Wang, H.; Stwalley, W. C.; Gould, P. L. *Phys. Rev. Lett.* **2000**, *84*(2), 246.

[153] Viteau, M.; Chotia, A.; Allegrini, M.; Bouloufa, N.; Dulieu, O.; Comparat, D.; Pillet, P. *Science* **2008**, *321*, 232–234.

[154] Koch, C. P.; Palao, J. P.; Kosloff, R.; Masnou-Seeuws, F. *Phys. Rev. A* **2004**, *70*(1), 013402.

[155] Wang, H.; Stwalley, W. C. *J. Chem. Phys.* **1998**, *108*(14), 5767.

[156] Stwalley, W. C. *Eur. Phys. J. D* **2004**, *31*(2), 221.

[157] Kotochigova, S.; Tiesinga, E.; Julienne, P. S. *Eur. Phys. J. D* **2004**, *31*(2), 189.

[158] Sage, J. M.; Sainis, S.; Bergeman, T.; DeMille, D. *Phys. Rev. Lett.* **2005**, *94*(20), 203001.

[159] Deiglmayr, J.; Grochola, A.; Repp, M.; Mörtlbauer, K.; Glück, C.; Lange, J.; Dulieu, O.; Wester, R.; Weidemller, M. *Phys. Rev. Lett.* **2008**, *101*(13), 133004.

[160] Tiesinga, E.; Verhaar, B. J.; Stoof, H. T. C. *Phys. Rev. A* **1993**, *47*(5), 4114.

[161] Inouye, S.; Andrews, M. R.; Stenger, J.; Miesner, H. J.; Stamper-Kurn, D. M.; Ketterle, W. *Nature* **1998**, *392*(6672), 151.

[162] Mies, F. H.; Tiesinga, E.; Julienne, P. S. *Phys. Rev. A* **2000**, *61*(2), 022721.

[163] Regal, C. A.; Ticknor, C.; Bohn, J. L.; Jin, D. S. *Nature* **2003**, *424*(6944), 47.

[164] Herbig, J.; Kraemer, T.; Mark, M.; Weber, T.; Chin, C.; Nägerl, H. C.; Grimm, R. *Science* **2003**, *301*(5639), 1510.

[165] Xu, K.; Mukaiyama, T.; Abo-Shaeer, J. R.; Chin, J. K.; Miller, D. E.; Ketterle, W. *Phys. Rev. Lett.* **2003**, *91*(21), 210402.

[166] Dürr, S.; Volz, T.; Marte, A.; Rempe, G. *Phys. Rev. Lett.* **2004**, *92*(2), 020406.

[167] Strecker, K. E.; Partridge, G. B.; Hulet, R. G. *Phys. Rev. Lett.* **2003**, *91*(8), 080406.

[168] Cubizolles, J.; Bourdel, T.; Kokkelmans, S. J. J. M. F.; Shlyapnikov, G. V.; Salomon, C. *Phys. Rev. Lett.* **2003**, *91*(24), 240401.

[169] Jochim, S.; Bartenstein, M.; Altmeyer, A.; Hendl, G.; Chin, C.; Denschlag, J. H.; Grimm, R. *Phys. Rev. Lett.* **2003**, *91*(24), 240402.

[170] Jochim, S.; Bartenstein, M.; Altmeyer, A.; Hendl, G.; Riedl, S.; Chin, C.; Denschlag, J. H.; Grimm, R. *Science* **2003**, *302*(5653), 2101.

[171] Donley, E. A.; Claussen, N. R.; Thompson, S. T.; Wieman, C. E. *Nature* **2002**, *417*(6888), 529.

[172] Claussen, N. R.; Kokkelmans, S. J. J. M. F.; Thompson, S. T.; Donley, E. A.; Hodby, E.; Wieman, C. E. *Phys. Rev. A* **2003**, *67*(6), 060701.

[173] Thompson, S. T.; Hodby, E.; Wieman, C. E. *Phys. Rev. Lett.* **2005**, *95*(19), 190404.

[174] Köhler, T.; Goral, K.; Julienne, P. S. *Rev. Mod. Phys.* **2006**, *78*(4), 1311.

[175] Krems, R. V.; Dalgarno, A.; Balakrishnan, N.; Groenenboom, G. C. *Phys. Rev. A* **2003**, *67*(6), 060703.

[176] Krems, R. V.; Dalgarno, A. *J. Chem. Phys.* **2004**, *120*(5), 2296.

[177] Krems, R. V.; Sadeghpour, H. R.; Dalgarno, A.; Zgid, D.; Kłos, J.; Chałasiński, G. *Phys. Rev. A* **2003**, *68*(5), 051401.

[178] Campbell, W. C.; Tscherbul, T. V.; Lu, H.; Tsikata, E.; Krems, R. V.; Doyle, J. M. *Phys. Rev. Lett.* **2009**, *102*(1), 013003.

[179] Myatt, C. J.; Burt, E. A.; Ghrist, R. W.; Cornell, E. A.; Wieman, C. E. *Phys. Rev. Lett.* **1997**, *78*(4), 586.

[180] Balakrishnan, N.; Kharchenko, V.; Forrey, R. C.; Dalgarno, A. *Chem. Phys. Lett.* **1997**, *280*(1-2), 5.

[181] Balakrishnan, N.; Forrey, R. C.; Dalgarno, A. *Chem. Phys. Lett.* **1997**, *280*(1-2), 1.

[182] Forrey, R. C.; Balakrishnan, N.; Dalgarno, A.; Lepp, S. *Astrophys. J.* **1997**, *489*(2), 1000.

[183] Balakrishnan, N.; Forrey, R. C.; Dalgarno, A. *Phys. Rev. Lett.* **1998**, *80*(15), 3224.

[184] Balakrishnan, N.; Forrey, R. C.; Dalgarno, A. *Astrophys. J.* **1999**, *514*(1), 520.

[185] Forrey, R. C.; Kharchenko, V.; Balakrishnan, N.; Dalgarno, A. *Phys. Rev. A* **1999**, *59*(3), 2146.

[186] Balakrishnan, N.; Dalgarno, A.; Forrey, R. C. *J. Chem. Phys.* **2000**, *113*(2), 621.

[187] Zhu, C.; Balakrishnan, N.; Dalgarno, A. *J. Chem. Phys.* **2001**, *115*(3), 1335.

[188] Krems, R. V. *J. Chem. Phys.* **2002**, *116*(11), 4517.

[189] Krems, R. V. *J. Chem. Phys.* **2002**, *116*(11), 4525.

[190] Cecchi-Pestellini, C.; Bodo, E.; Balakrishnan, N.; Dalgarno, A. *Astrophys. J.* **2002**, *571*(2), 1015.

[191] Bodo, E.; Gianturco, F. A. *J. Phys. Chem. A* **2003**, *107*(37), 7328.

[192] Florian, P. M.; Hoster, M.; Forrey, R. C. *Phys. Rev. A* **2004**, *70*(3), 032709.

[193] Cybulski, H.; Krems, R. V.; Sadeghpour, H. R.; Dalgarno, A.; Kłos, J.; Groenenboom, G. C.; van der Avoird, A.; Zgid, D.; Chałasiński, G. *J. Chem. Phys.* **2005**, *122*(9), 094307.

[194] Stoecklin, T.; Voronin, A.; Rayez, J. C. *Chem. Phys.* **2003**, *294*(2), 117.

[195] M. L. González-Sánchez, E. B.; Gianturco, F. A. *Phys. Rev. A.* **2006**, *73*(2), 022703.

[196] Balakrishnan, N.; Groenenboom, G. C.; Krems, R. V.; Dalgarno, A. *J. Chem. Phys.* **2003**, *118*(16), 7386.

[197] Stoecklin, T.; Voronin, A.; Rayez, J. C. *Phys. Rev. A.* **2003**, *68*(3), 032716.

[198] Balakrishnan, N.; Dalgarno, A. *J. Phys. Chem. A* **2001**, *105*(11), 2348.

[199] Tilford, K.; Hoster, M.; Florian, P. M.; Forrey, R. C. *Phys. Rev. A* **2004**, *69*(5), 052705.

[200] Volpi, A.; Bohn, J. L. *J. Chem. Phys.* **2003**, *119*(2), 866.

[201] Reid, J. P.; Simpson, C. J. S. M.; Quiney, H. M. *J. Chem. Phys.* **1997**, *107*(23), 9929.

[202] Bodo, E.; Gianturco, F. A.; Dalgarno, A. *Chem. Phys. Lett.* **2002**, *353*(1-2), 127.

[203] Stewart, B.; Magill, P. D.; Scott, T. P.; Derouard, J.; Pritchard, D. E. *Phys. Rev. Lett.* **1988**, *60*(4), 282.

[204] Magill, P. D.; Stewart, B.; Smith, N.; Pritchard, D. E. *Phys. Rev. Lett.* **1988**, *60*(19), 1943.

[205] Forrey, R. C.; Balakrishnan, N.; Dalgarno, A.; Haggerty, M. R.; Heller, E. J. *Phys. Rev. Lett* **1999**, *82*(13), 2657.

[206] Forrey, R. C. *Phys. Rev. A* **2002**, *66*(2), 023411.

[207] Baranov, M. A.; Osterloh, K.; Lewenstein, M. *Phys. Rev. Lett.* **2005**, *94*(7), 070404.

[208] Zhang, J.; Zhai, H. *Phys. Rev. Lett.* **2005**, *95*(20), 200403.

[209] Osterloh, K.; Barberán, N.; Lewenstein, M. *Phys. Rev. Lett.* **2007**, *99*(16), 160403.

[210] Quéméner, G.; Launay, J. M.; Honvault, P. *Physical. Rev. A* **2007**, *75*(5), 050701.

[211] Soldán, P.; Cvitaš, M. T.; Hutson, J. M.; Honvault, P.; Launay, J. M. *Phys. Rev. Lett.* **2002**, *89*(15), 153201.

[212] Quéméner, G.; Honvault, P.; Launay, J. M. *Eur. Phys. J. D* **2004**, *30*(2), 201.

[213] Cvitaš, M. T.; Soldán, P.; Hutson, J. M.; Honvault, P.; Launay, J. M. *Phys. Rev. Lett.* **2005**, *94*(3), 033201.

[214] Cvitaš, M. T.; Soldán, P.; Hutson, J. M.; Honvault, P.; Launay, J. M. *J. Chem. Phys.* **2007**, *127*(7), 074302.

[215] Quéméner, G.; Honvault, P.; Launay, J. M.; Soldán, P.; Potter, D. E.; Hutson, J. M. *Phys. Rev. A* **2005**, *71*(3), 032722.

[216] Wynar, R.; Freeland, R. S.; Han, D. J.; Ryu, C.; Heinzen, D. J. *Science* **2000**, *287*(5455), 1016.

[217] Mukaiyama, T.; Abo-Shaeer, J. R.; Xu, K.; Chin, J. K.; Ketterle, W. *Phys. Rev. Lett.* **2004**, *92*(18), 180402.

[218] Syassen, N.; Volz, T.; Teichmann, S.; Dürr, S.; Rempe, G. *Phys. Rev. A* **2006**, *74*(6), 062706.

[219] Zahzam, N.; Vogt, T.; Mudrich, M.; Comparat, D.; Pillet, P. *Phys. Rev. Lett.* **2006**, *96*(2), 023202.

[220] Staanum, P.; Kraft, S. D.; Lange, J.; Wester, R.; Weidemüller, M. *Phys. Rev. Lett.* **2006**, *96*(2), 023201.

[221] Regal, C. A.; Greiner, M.; Jin, D. S. *Phys. Rev. Lett.* **2004**, *92*(8), 083201.

[222] Petrov, D. S.; Salomon, C.; Shlyapnikov, G. V. *Phys. Rev. A* **2005**, *71*(1), 012708.

[223] DeMarco, B.; Papp, S. B.; Jin, D. S. *Phys. Rev. Lett.* **2001**, *86*(24), 5409.

[224] Lee, T. G.; Rochow, C.; Martin, R.; Clark, T. K.; Forrey, R. C.; Balakrishnan, N.; Stancil, P. C.; Schultz, D. R.; Dalgarno, A.; Ferland, G. J. *J. Chem. Phys.* **2005**, *122*(2), 024307.

[225] Soldán, P.; Cvitaš, M. T.; Hutson, J. M. *Phys. Rev. A* **2003**, *67*(5), 054702.

[226] Volpi, A.; Bohn, J. L. *Phys. Rev. A* **2002**, *65*(5), 052712.

[227] Tscherbul, T. V.; Krems, R. V. *Phys. Rev. Lett.* **2006**, *97*(8), 083201.

[228] E., A.; V., T. T.; Krems.; V., R. *J. Chem. Phys* **2007**, *127*(4), 044302.

[229] Tscherbul, T. V. *J. Chem. Phys.* **2008**, *128*(24), 244305.

[230] Pavlovic, Z.; Tscherbul, T. V.; Sadeghpour, H. R.; A., G. C. G.; Dalgarno. *J. Phys. Chem. A* **2009**, *113*(52), 14670.

[231] Tscherbul, T. V.; Groenenboom, G. C.; Krems, R. V.; Dalgarno, A. *Faraday Discussions* **2009**, *142*, 127.

[232] Tscherbul, T. V.; Klos, J.; Rajchel, L.; Krems, R. V. *Phy. Rev. A* **2007**, *75*(3), 033416.

[233] Sawyer, B. C.; Stuhl, B. K.; Wang, D.; Yeo, M.; Ye, J. *Phys. Rev. Lett.* **2008**, *101*(20), 203203.

[234] Alyabyshev, S. V.; Krems, R. V. *Phys. Rev. A* **2009**, *80*(3), 033419.

[235] Ni, K. K.; Ospelkaus, S.; de Miranda, M. H. G.; Pe'er, A.; Neyenhuis, B.; Zirbel, J. J.; Kotochigova, S.; Julienne, P. S.; Jin, D. S.; Ye, J. *Science* **2008**, *322*(5899), 231.

[236] Ni, K. K.; Ospelkaus, S.; Nesbitt, D. J.; Ye, J.; Jin, D. S. *Phys. Chem. Chem. Phy.* **2009**, *11*(42), 9626.

[237] Ni, K. K.; Ospelkaus, S.; Wang, D.; Quemener, G.; Neyenhuis, B.; de Miranda, M. H. G.; Bohn, J. L.; Ye, J.; Jin, D. S. *Nature* **2010**, *464*(7293), 1324.

[238] Ospelkaus, S.; Ni, K. K.; Wang, D.; de Miranda, M. H. G.; Neyenhuis, B.; Quemener, G.; Julienne, P. S.; Bohn, J. L.; Jin, D. S.; Ye, J. *Science* **2010**, *327*(5967), 853.

[239] Avdeenkov, A. V.; Bohn, J. L. *Phys. Rev. A* **2002**, *66*(5), 052718.

[240] Avdeenkov, A. V.; Bohn, J. L. *Phys. Rev. Lett.* **2003**, *90*(4), 043006.

[241] Avdeenkov, A. V.; Bortolotti, D. C. E.; Bohn, J. L. *Phys. Rev. A* **2004**, *69*(1), 012710.

[242] Avdeenkov, A. V.; Bohn, J. L. *Phys. Rev. A* **2005**, *71*(2), 022706.

[243] Ticknor, C.; Bohn, J. L. *Phys. Rev. A* **2005**, *72*(3), 032717.

[244] Avdeenkov, A. V.; Kajita, M.; Bohn, J. L. *Phys. Rev. A* **2006**, *73*(2), 022707.

[245] Alexander, A. V. *New J. Phys.* **2009**, *11*, 055016.

[246] Ticknor, C. *Phys. Rev. Lett.* **2008**, *100*(13), 133202.

[247] Ticknor, C.; Bohn, J. L. *Phys. Rev. A* **2005**, *71*(2), 022709.

[248] Kajita, M. *Phys. Rev. A* **2006**, *74*(3), 032710.

[249] Tscherbul, T. V.; Suleimanov, Y. V.; Aquilanti, V.; Krems, R. V. *New J. Phys.* **2009**, *11*, 055021.

[250] Quemener, G.; Bohn, J. L. *Phys. Rev. A.* **2010**, *81*(2), 022702.

[251] Ospelkaus, S.; Ni, K. K.; Quemener, G.; Neyenhuis, B.; Wang, D.; de Miranda, M. H. G.; Bohn, J. L.; Ye, J.; Jin, D. S. *Phys. Rev. Lett.* **2010**, *104*(3), 030402.

[252] Aldegunde, J.; Ran, H.; Hutson, J. M. *Phys. Rev. A* **2009**, *80*(4), 043410.

[253] Dantus, M.; Lozovoy, V. V. *Chem. Rev.* **2004**, *104*(4), 1813.

[254] Vardi, A.; Abrashkevich, D. G.; Frishman, E.; Shapiro, M. *J. Chem. Phys.* **1997**, *107*(16), 6166.

[255] Salzmann, W.; Poschinger, U.; Wester, R.; Weidemüller, M.; Merli, A.; Weber, S. M.; Sauer, F.; Plewicki, M.; Weise, F.; Esparza, A. M.; Woste, L.; Lindinger, A. *Phys. Rev. A* **2006**, *73*(2), 023414.

[256] Forrey, R. C.; Balakrishnan, N.; Kharchenko, V.; Dalgarno, A. *Phys. Rev. A* **1998**, *58*(4), 2645.

[257] Li, Z.; Krems, R. V. *Phys. Rev. Lett* **2007**, *75*(3), 032709.

[258] Krems, R. V. *Phys. Rev. Lett.* **2006**, *96*(12), 123202.

[259] Ghosal, S. private communication, **2007**.

[260] Johnson, B. R. *J. Chem. Phys.* **1977**, *67*, 4086.

[261] Wicke, B. G.; Harris, D. O. *J. Chem. Phys.* **1976**, *64*, 5236.

[262] Cashion, J. K. *J. Chem. Phys.* **1963**, *39*, 1872.

[263] Cooley, J. W. *Math. Comput.* **1961**, *15*, 363–374.

[264] D. G. Truhlar, D. W. Oslon, A. C. J.; Overend, J. *J. Am. Chem. Soc.* **1976**, *98*, 2373.

[265] Lin, C. S. *J. Chem. Phys.* **1974**, *60*, 1974.

[266] Shore, B. W. *J. Chem. Phys.* **1973**, *59*, 6450.

[267] Numerov, B. *Publs. Observatoire Central Astrophys. Russ* **1933**, *2*, 188.

[268] Press, W. H.; Teukolsky, S. A.; Vetterling, W. T.; Flannery, B. P. *Numerical Recipies in Fortran;* Cambridge University Press: Cambridge, 1992.

[269] Landau, L. D.; Lifshitz, E. M. *Quantum Mechanics (Non-relativistic Theory): third edition;* Butterworth-Heinemann: Oxford, 1981.

[270] Levine, R. D. *J. Chem. Phys.* **1968**, *49*, 51.

[271] Holmgren, S. L.; Waldman, M.; Klemperer, W. *J. Chem. Phys.* **1977**, *67*, 4414.

[272] Hutson, J. M. *Adv. Mol. Vibrat. Coll. Dyn.* **1991**, *1A*, 1.

[273] Tamir, M.; Shapiro, M. *Chem. Phys. Lett.* **1975**, *31*, 166.

[274] Tennyson, J. *Comp. Phys. Reports* **1986**, *4*, 1.

[275] Tennyson, J.; Miller, S.; Henderson, J. R. In *Methods in Computational Chemistry, Vol. 5*; Wilson, S., Ed.; Plenum: New York, 1991.

[276] Bačić, Z.; Light, J. C. *Annu. Rev. Phys. Chem.* **1989**, *40*, 469.

[277] Gordon, R. G. *J. Chem. Phys.* **1969**, *51*, 14.

[278] Johnson, B. R. *J. Chem. Phys.* **1978**, *69*(10), 4678.

[279] Hutson, J. M. *Comput. Phys. Commun.* **1994**, *84*(1-3), 1.

[280] Johnson, B. R. *J. Comput. Phys.* **1973**, *13*(3), 445.

[281] Froese, C. *Proc. Camb. Phil. Soc.* **1957**, *53*, 206.

[282] Froese, C. *Can. J. Phys.* **1963**, *41*, 1895.

[283] Fox, L. *Proc. Camb. Phil. Soc.* **1961**, *57*, 103.

[284] Manolopoulos, D. E. *PhD Thesis, Cambridge University* **1988**.

[285] Calvert, J. M.; Wood, W. D. *J. Phys. A* **1969**, *2*, 278.

[286] Mrugala, F.; Secrest, D. *J. Chem. Phys.* **1983**, *78*, 5954.

[287] Light, J. C.; Walker, R. B. *J. Chem. Phys.* **1976**, *65*, 4272.

[288] Manolopoulos, D. E. *J. Chem. Phys.* **1986**, *85*(11), 6425.

[289] Pethick, C. J.; Smith, H. *Bose-Einstein Condensation in Dilute Gases;* Cambridge University Press, 2002.

[290] Aquilanti, V.; Ascenzi, D.; Vitores, M. D.; Pirani, F.; Cappelletti, D. *J. Chem. Phys.* **1999**.

[291] Aquilanti, V.; Ascenzi, D.; Cappelletti, D.; Pirani, F. *J. Phys. Chem. A.*

[292] Groenenboom, G. C.; Struniewicz, I. M. *J. Chem. Phys.* **2000**, *113*(21), 9562.

[293] Cybulski, S. M.; Burcl, R.; Szczesniak, M. M.; Chalasinski, G. *J. Chem. Phys.* **1996**, *104*(20), 7997.

[294] González-Martínez, M. L.; Hutson, J. M. *Phys. Rev. A* **2007**, *75*, 022702.

[295] Golubiatnikov, G. Y.; Krupnov, A. F. *Journal of Molecular Spectroscopy* **2004**, *225*(2), 222.

[296] Brink, D. M.; Satchler, G. R. *Angular Momentum;* Clarendon Press: Oxford, 3rd ed., 1994.

[297] Boys, S. F.; Bernardi, F. *Mol. Phys.* **1970**, *19*(4), 553.

[298] BOUND computer program, version 5. Hutson, J. M. distributed by Collaborative Computational Project No. 6 of the UK Engineering and Physical Sciences Research Council, **1993**.

[299] BOUND computer code, version 15 (2006). Hutson, J. M.

[300] MOLSCAT computer program, version 14. Hutson, J. M.; Green, S. distributed by Collaborative Computational Project No. 6 of the UK Engineering and Physical Sciences Research Council, **1994**.

[301] Mott, N. F.; Massey, H. S. W. *The Theory of Atomic Collisions;* Clarendon Press: Oxford, 3rd ed., 1965.

[302] Hinckelmann, O.; Spruch, L. *Phys. Rev. A* **1971**, *3*, 642.

[303] Hazi, A. U. *Phys. Rev. A* **1979**, *19*, 920.

[304] Ashton, C. J.; Child, M. S.; Hutson, J. M. *J. Chem. Phys.* **1983**, *78*, 4025.

[305] Hutson, J. M. *New J. Phys.* **2007**, *9*, 152.

[306] Resfit 2007 computer program. Hutson, J. M. **2007**.

[307] Masuhara, N.; Doyle, J. M.; Sandberg, J. C.; Kleppner, D.; Greytak, T. J.; Hess, H. F.; Kochanski, G. P. *Phys. Rev. Lett.* **1988**, *61*(8), 935.

[308] Fano, U. *Phys. Rev.* **1961**, *124*, 1866.

[309] Hutson, J. M.; Beyene, M.; González-Martínez, M. L. *Phys. Rev. Lett.* **2009**, *103*(16), 163201.